ENZYME COFACTOR REGENERATION FOR BIOELECTROCATALYSIS

By

Hanzi Li

A DISSERTATION

Submitted to
Michigan State University
in partial fulfillment of the requirements
for the degree of

Chemical Engineering – Doctor of Philosophy

2014

ABSTRACT

ENZYME COFACTOR REGENERATION FOR BIOELECTROCATALYSIS

By

Hanzi Li

The effective regeneration of nicotinamide adenine dinucleotide, possibly phosphorylated, (NAD(P)H/NAD(P)$^+$) is of great interest, because NAD(P)H/NAD(P)$^+$ acts as an essential cofactor in ubiquitous redox enzymes that are widely applicable in biosensors, bioenergy and bioconversion. However, NAD(P)H oxidation occurs at very high overpotentials, leading to significant energy inefficiencies and increasing the possibility of side reactions. To address these challenges, in this work, we have designed and engineered nanostructured interfaces for high-performance electrochemical cofactor regeneration applicable to bioelectrocatalysis.

A high-rate NADH oxidizing electrode was fabricated by incorporating poly(azine) electrocatalysts into a high surface area layer of carboxylated carbon nanotubes (CNTs). Electrodeposition of poly(methylene green) (PMG) and poly(toluidine blue) (PTBO) on the carboxylated CNT-modified electrodes was achieved by cyclic voltammetry. The PMG-CNT interface demonstrates 5.0 mA cm^{-2} current density for NADH oxidation at 50 mV vs. Ag|AgCl in 20 mM NADH solution.

The bioactivity of cofactor electrogenerated NAD$^+$ was verified spectroscopically. A mathematical model calibrated by measurements of NADH oxidation at PMG-CNT-modified glassy carbon electrodes was applied to predict transient NADH consumption. The model showed good agreement with the experimental data, and 80% conversion of NADH was

observed after 1 hour of electrochemical oxidation. Using a spectroscopic enzyme cycling assay, the yield of enzymatically active NAD^+ was verified at 93% and 87% for applied potentials of 500 mV and 150 mV vs. Ag|AgCl, respectively.

To further facilitate NADH electrocatalysis, electrochemical activation of carbon material was found to increase electrode reactivity by introducing carbon-oxygen functionalities. Electrochemically activated carbon electrodes demonstrate enhanced activity toward NADH oxidation, and more importantly, dramatically improved adsorption of bioelectrochemically active azine dyes. Adsorption of methylene green (MG) on an electroactivated carbon electrode yielded a catalyst layer that is 1.8-fold more active toward NADH oxidation than an electrode prepared using electropolymerized MG.

A quantitative model was developed to explain and predict experimental phenomena and design bioelectronic interfaces. The kinetics of bioelectrocatalysis can be simplified into two steps: the electrocatalytic regeneration of cofactor $NADH/NAD^+$ and the enzymatic reaction of substrate using dehydrogenase. Planar and porous interface structures are modeled to evaluate the kinetics and diffusion for the bioelectronic interface.

This dissertation presents various fabrication, characterization and modeling methods for cofactor regeneration. The findings and designs in this work are highly applicable to dehydrogenase-based economical bioelectrocatalysis.

ACKNOWLEDGEMENTS

I would like to take this opportunity to formally thank my advisor, Professor Scott Calabrese Barton, for his great leadership and guidance. My dream to earn a doctoral degree would not have been realized without his help, support and encouragement. He taught how to do research. He has always helped me to plan and prioritize my work. He is so supportive during the up and downs not only in research but also in life. I enjoyed the time when he invited us to have dinner with his family.

I would like to thank Dr. Robert. M. Worden, Dr. Ilsoon Lee, and Dr. Claire Vieille for serving in my committee and giving me such valuable guidance. Thanks to Dr. Lee for all his advice in nanostructure and modeling work. Thanks to Dr. Worden and Dr. Vieille for attending every bi-weekly project meeting and providing such helpful suggestions.

I am very thankful for our collaborators, Justin Beauchamp in Dr. Vieille's group, Dr. Rui Li and Chloe Liu in Dr. Worden's group. The collaborative projects have helped me gain knowledge in diversified fields of science and engineering, and have also helped me with my "people" skills: communication and teamwork.

I want to thank my wonderful colleagues: Dr. Kothandaraman Ramanujam, Dr. Deboleena Chakraborty and Dr. Vijayadurga Nallathambi, who helped me start electrochemical experiments during the early stages of my Ph.D life; Dr. Hao Wen for discussing research details with me and helping me start my first paper; Dr. Piyush Kar, Harshal Bambhania, Dr. Selvarani Ganesan, Nate Leonard, Yira Feliciano Vega, Duyen Van Thuy Do for being such wonderful co-

workers. Thanks to Duyen for taking over my work after I graduate. I would also like to acknowledge the undergraduates: Kyle Anderson, Kathryn Worley and Raul Dacomba, who worked with me and helped me to speed up research progress.

Very importantly, I would like to acknowledge my family: my mother Wenjuan Lv, my father Bin Li and my boyfriend Guokai Zeng. Thank you so much for being so understanding and supportive. Thank you for your constant and unconditional love. During the ups and downs of my PhD career, I know you have always been there to support me. Thank my parents for teaching me the essence of life. Thank my boyfriend for his encouragement. I could not have done this without you.

TABLE OF CONTENTS

LIST OF TABLES

LIST OF FIGURES

1 Introduction

1.1 Enzyme catalysis

Catalysis is a key field in chemistry and chemical engineering that enables cost-efficient and environmentally friendly processes, and has led to a large variety of chemical products and a strong economic impact.[1] The development of new catalysts and catalyst paradigms carries with the potential for multiple technological breakthroughs.[2]

Biocatalysis concerns the use of enzymes as catalysts. Enzymes possess several advantages over traditional metal-based homogeneous and heterogeneous catalysis.[3-5] Biocatalysts demonstrate remarkable chemical precision in organic synthesis, leading to significant chemical selectivity and direct commercial benefits such as fewer side reactions, easier separation, and reduced pollution.[5,6] Another advantage of biocatalysis is its ability to catalyze reactions under mild conditions. Enzymes typically function at ambient temperature, atmospheric pressure, and near neutral pH.[6,7] A third advantage of biocatalysis is its high catalytic efficiency, as demonstrated by characteristically high turn-over numbers, with acceleration rate constants of more than 10^8 compared to non-biocatalytic reactions.[6,7] This degree of acceleration is impressive, especially under mild reaction conditions.[6]

Biocatalysis may involve the use of whole cells or enzymes.[8] Whole-cell biocatalysis uses intracellular enzymes which operate as part of a living organism,[9] and is often described as

microbial catalysis.[8] In industry, this approach is often applied for synthetic reactions where enzyme cofactors are needed, because it is relatively well-developed and less expensive to recycle cofactors.[5] But compared to enzyme catalysis, whole-cell catalysis generally has disadvantages of low reactor-volume productivity and product separation complexity.

Alternatively, enzyme catalysis uses isolated enzymes from an organism, and eliminates potential diffusion limitations caused by the cell membranes, allowing for a remarkable increase in volumetric activity.[9] Enzyme catalysts tolerate harsher conditions than microbial counterparts and are easier to ship around the world.[3]

Because of these advantages, in the past few decades, enzyme catalysis has emerged as an important tool in the industrial synthesis of bulk chemicals, pharmaceuticals and food ingredients.[3] Table 1.1 shows some examples of recent industrial enzyme biocatalysis.[3,5,10] For example, in the past ten years, ketone reduction-based processes gradually replaced whole-cell biocatalysis and metal-based chemocatalysis,[3] as a result of enzyme catalysis of cofactor regeneration, the details of which will be discussed in Section 1.3.

Table 1.1 Recent established industrial enzyme catalysis systems[3,5,10]

Type of reaction	Product	Enzyme	Scale	Source
Ketone reduction	4(S)-hydroxy-6(S)methyl-thienopyran derivatives	Alcohol dehydrogenase	Several t yr^{-1}	Astra Zeneca[144]
	dihydroxy esters and derivatives	Alcohol dehydrogenase	35 t yr^{-1}	Wacker Chemie[145]
	(R)-methylpentan-2-ol	Lactate dehydrogenase	Several kg scale / 560 g L^{-1} d^{-1}	Pfizer[146]
	(L)-amino acid	Leucine dehydrogenase	Several ton scale / 560 g L^{-1} d^{-1}	Former Degussa AG[5]
Hydrolysis / Esterification	Chiral amines	Lipases	Up to 1000 t yr^{-1}	BASF[10]
	Enantiopure alcohols	Lipases	Several 100 t yr^{-1}	BASF[5]
	(R)-mandelic acid	Nitrilase	Several t yr^{-1}	BASF[1]

One important enzyme group in enzyme catalysis is the oxidoreductases (redox enzymes). By transferring electrons or protons, redox enzymes can catalyze the oxidation or the reduction of a substrate or a group of substrates.[7,11] For some redox enzymes, in order to be activated, enzyme cofactors are required. Enzyme cofactors include nicotinamide adenine dinucleotide (phosphorylated) ($NAD(P)^+$), flavin adenine dinucleotide (FAD), flavin mononucleotide (FMN), and coenzyme A (CoA).[7,12] Because over 60% of redox enzymes use $NAD(P)^+$ or its reduced form NAD(P)H as cofactor, research work on dehydrogenase cofactor regeneration is mainly focused on ($NAD(P)^+$) and NAD(P)H.[7,8,12] The chemical structure of NAD^+ is shown in Figure

1.1.[13] In phosphorylated cofactor $NADP^+$, a $PO(OH)_2$ group replaces the indicated H. For reduced form cofactor NADH, 1,4-NADH is bioactive, whereas 1,6-NADH is non-bioactive.[14]

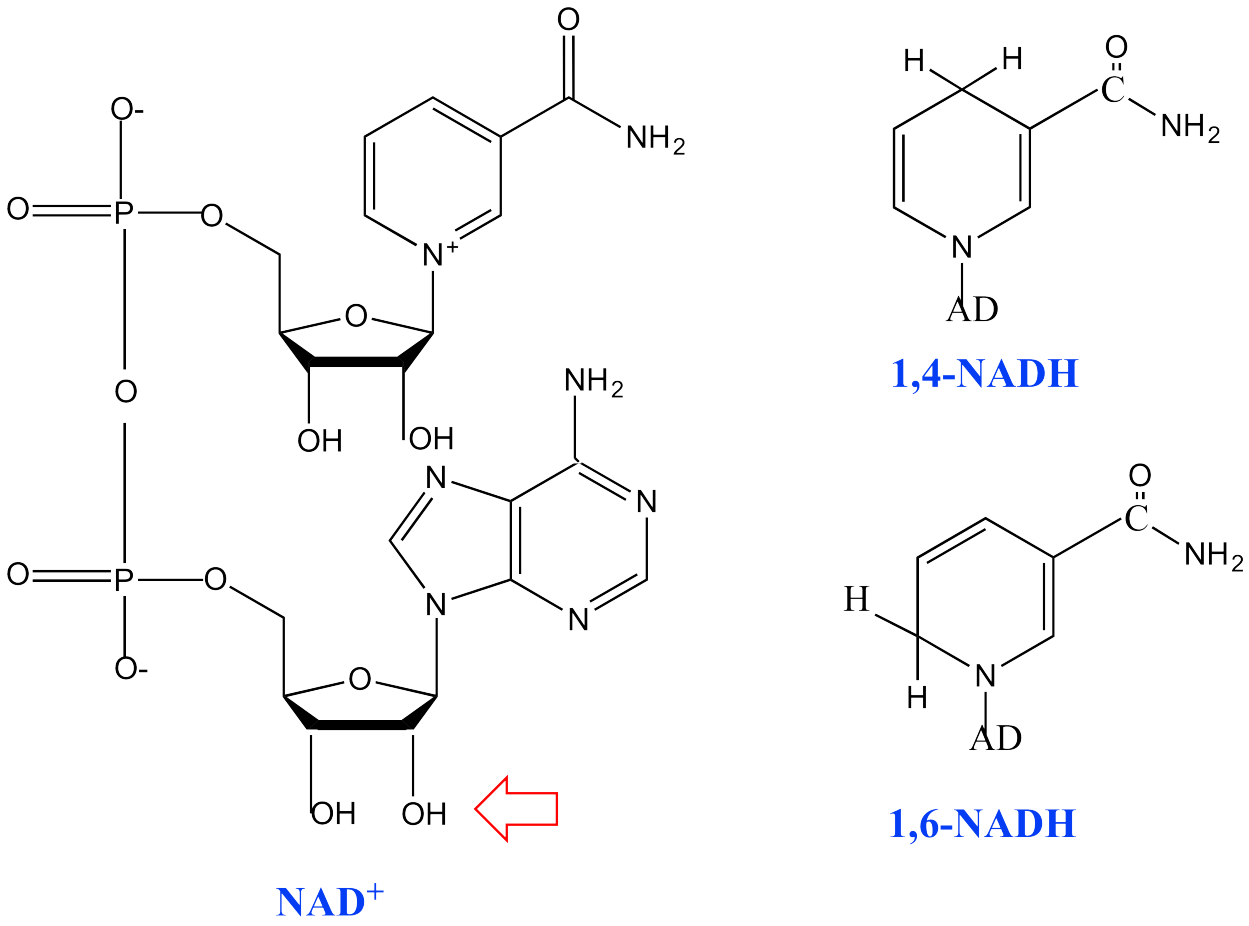

Figure 1.1 Chemical structures of nicotinamide adenine dinucleotide oxidized form (NAD^+), and reduced form 1,4-NADH and 1,6-NADH. In phosphorylated cofactor $NADP^+$, a $PO(OH)_2$ group replaces the arrow indicated OH. (For interpretation of the references to color in this and all other figures, the reader is referred to the electronic version of this dissertation.)

1.2 Cofactor NAD(P)H/NAD(P)$^+$ regeneration

A key problem in use of NAD(P)H-dependent enzymes is the high production cost of the cofactor, NAD(P)$^+$, which is more than ~$ 64 g^{-1} for ≥ 96.5% purity[15] and is even more expensive than the desired products.[12] Accordingly, it is crucial to develop effective approaches to regenerate the cofactors.

In nature, NADH generation by NAD$^+$ reduction is part of beta oxidation, glycolysis, and the citric acid cycle.[7] For example, in citric acid cycle, NADH is generated by malate dehydrogenase, isocitrate dehydrogenase and α-ketoglutarate dehydrogenase, respectively.[7] The generated NADH is fed into the oxidative phosphorylation pathway.[7] With the formation of ATP, NAD$^+$ is regenerated by NADH oxidation.[7]

The state-of-the-art procedures for cofactor regeneration include microbiological, enzymatic, chemical, photochemical, and electrochemical approaches.[16-19] Among these procedures, electrochemical regeneration is the most promising method because of its high selectivity, easy product separation, low cost of electricity and facile monitoring/controlling system.[12,17,18,20-23]

The microbial method has employed common microorganisms including *Escherichia coli* and *Saccharomyces cerevisiae*.[16-18] This method has been used in industrial production of

NADH, because of its high selectivity, relatively easy operation, and inexpensive feed reagents (mainly oxygen and sugar).[16-18] However, the disadvantages, such as low reactor-volume productivity and product separation complexity, seriously hinder its further application.[17]

The enzymatic method mimics microbial reaction pathways but achieves higher rate per reactor volume, at greater expense as a result of the high cost and instability of enzymes. Commonly used enzymes in this regeneration system are alcohol dehydrogenase, glucose dehydrogenase, formate dehydrogenase and amino acid dehydrogenase.

The chemical method generally uses commercially available reagents, such as hydrogen as reducing agent and oxygen as oxidizing agent.[18] Nevertheless, it displays relatively low rates and limited compatibility with biochemical systems, since metal-based catalysis is not as effective or biocompatible as biocatalysis.[24]

The main advantage of photochemical regeneration is the low price of solar energy.[7] This method utilizes so-called photosensitizer, such as methylene blue, porphyrins and ruthenium complexes, to mediate electron transfer from cofactor to the terminal electron acceptor.[19] Semiconductive material such as titanium dioxide has also been reported for cofactor regeneration.[12] The disadvantage of this method is still the low efficiency.[18] Moreover, photo-excitation leads to the formation of reactive free radicals and strong oxidizing agents that react to form unwanted byproducts.[19]

1.3 Bioelectrocatalysis based on cofactor electro-regeneration

The electrochemistry of the NAD^+/NADH redox couple and $NADP^+$/NADPH redox couple are essentially identical.[24] The redox reactions between the oxidized forms and reduced forms involve a two-electron and one proton transfer, as shown below:[24]

$$NAD(P)H \xleftrightarrow{\text{Enzyme}} NAD(P)^+ + H^+ + 2e^- \quad [1.1]$$

The formal oxidation/reduction potential of this reaction is as low as -0.315 V versus standard hydrogen electrode (SHE) (0.1 vs. reversible hydrogen electrode (RHE)),[24,25] which is lower than many substrate/product couples, making the NAD(P)H oxidation reaction thermodynamically favorable.

Dehydrogenase-catalyzed redox reactions may be coupled with electrochemical methods via NAD(P)H-based bioelectrocatalysis. Substrate is converted to product by dehydrogenase according to:[26]

$$A + NAD(P)^+ \xleftrightarrow{\text{Enzyme}} B + NAD(P)H + H^+ \quad [1.2]$$

where A and B are substrate and product respectively. The cofactor NAD(P)H/$NAD(P)^+$ is regenerated electrochemically by Eq 1.1.

Because of the low redox potential of NAD(P)H/NAD(P)$^+$ and the ubiquity of NAD(P)H-dependent dehydrogenases in nature, NAD(P)H-dependent systems are considered widely applicable in biosensor, bioenergy and bioconversion technologies.[21,27-41]

Biosensors based on the NAD(P)H/NAD(P)$^+$ redox reaction detect an analyte by monitoring the rate of NAD(P)H oxidation or NAD(P)$^+$ reduction, and relating these to NAD(P)H concentration or NAD(P)$^+$ concentration via mass action correlations.[42] For example, because NADH/NAD$^+$ participates in naturally occurring enzymatic reactions involved in glycolysis, Kreb's cycle and oxidative phosphorylation,[7] biosensors for glucose,[43,44] glycerol,[37,45] lactate,[46] isocitrate[47] and alcohol[48-53] have been reported. Biofuel cells convert chemical energy to electrical energy via biocatalysis. Combining cofactor NAD$^+$ regeneration with enzyme catalyzed reactions allows one to utilize a great number of inexpensive fuels, *e.g.* methanol[29,54] and ethanol,[36] and develop efficient biofuel cells.[8,55] Similarly, electrochemical bioconversion utilizes electricity to produce chemical products. Applications of NAD(P)H-dependent dehydrogenases to produce value-added chemicals have been studied as well, such as production of mannitol from fructose,[56,57] dihydroxyacetone (DHA) from cheap glycerol[12,58,59] and methanol from CO_2.[60]

A concept of electrobiochemical reactor for producing DHA at anode and mannitol at cathode is depicted in Figure 1.2. Enzymatic DHA production is achieved by glycerol

dehydrogenase catalysis in presence of cofactor NAD^+ that is regenerated by NADH electrochemical oxidation at anode with electrons released to external circuit. The protons formed in the anodic process transport to the cathode through an ionomer membrane. In cathodic process, mannitol production involves the conversion of glucose to fructose by xylose isomerase (XI) and the subsequent production of mannitol from fructose by mannitol dehydrogenase (MtDH) in presence of cofactor NAD(P)H that is regenerated by NAD^+ electrochemical reduction.[56,57] The porous structure of the electrode significantly increases active surface area and improves rate for heterogeneous electrochemical reactions, and thus allows high-performance bioelectrocatalysis.

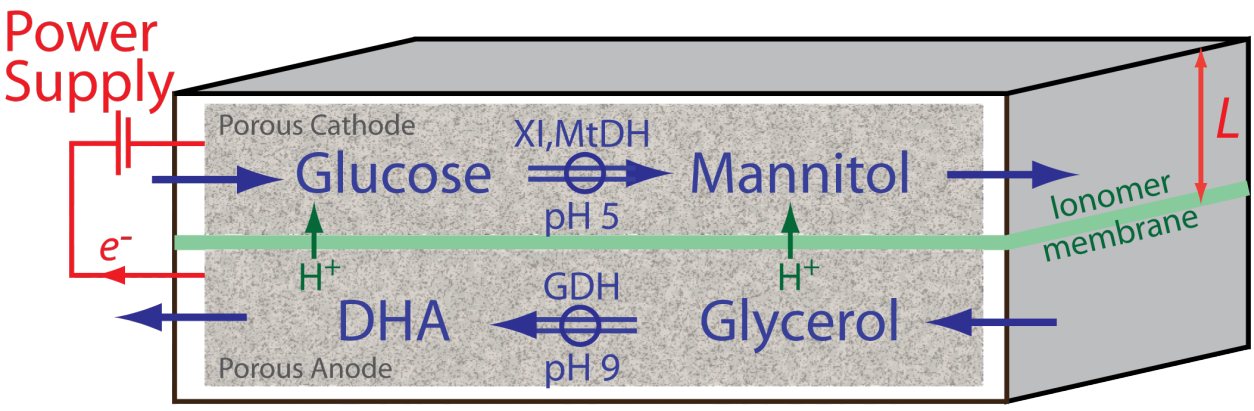

Figure 1.2 Bioreactor coupled with enzyme cofactor electrochemical regeneration, XI: xylose isomers, MtDH: mannitol dehydrogenase, GDH: Glycerol dehydrogenase.

1.4 Enzyme/Cofactor immobilization

Because of high cost, it is undesirable to feed enzymes or cofactors into a conversion process.[54] Instead, it is preferable to immobilize these active species on the electrode surface.[61] To maintain enzyme activity and improve stability, surface immobilization provides a powerful approach.[61] For NADH-dependent dehydrogenases, the cofactor NADH/NAD^+ is also preferred to be immobilized in order to allow easy access to the enzyme and avoid loss due to diffusion.[34]

Typical approaches to molecular immobilization include intermolecular linking by means of bifunctional or multifunctional reagents, and entrapment into a polymer matrix or a semi-permeable membrane.[31,32,54,61,62] The Worden Lab has developed intermolecular linking by means of bifunctional or multifunction reagents. They have reported cysteine as a heterotrifunctional linking molecule that is attached to the electrode by sulfhydryl groups, to the electrode mediator by carboxyl group and to the cofactor by amino group.[32] Additionally, the Vieille Lab suggested that the N^6-aryl amine is a useful binding site for immobilization of NAD^+/NADH (structure of NADH is shown in Figure 1.1). This indicates that, for an MtDH or GlyDH based interface, cofactor immobilization via an N^6-aryl amine is a promising approach. The Vieille lab is synthesizing N^6-carboxymethyl-NAD^+/NADH, the carboxyl group of which can covalently attach to amino group, offering a promising approach for cofactor immobilization. Zhou *et al.* reported a facile approach for cofactor NAD^+ immobilization.[43] They reported that NAD^+ can be non-covalently attached to CNT via the strong π-π stacking interaction between

the adenine subunit in NAD^+ group and CNT.[43] Thus, by simply mixing NAD^+ and CNT in distilled water under stirring condition, a suspension of NAD^+/CNT was obtained.[43] They used X-ray photoelectron spectroscopy to indicate the successful binding of NAD^+ and CNT.[43]

1.5 Electrocatalysis for NADH/NAD^+ redox reaction

Although the redox potential of NADH oxidation is low, on a bare carbon or metallic electrode, the direct electrochemical oxidation of NADH on glassy carbon electrodes becomes kinetically significant only above 1.09 V vs. RHE.[8,63] As shown in Figure 1.3, thermodynamically the oxidation of NADH should occur just above -0.48 V vs. Ag|AgCl. However, on glassy carbon electrode, oxidation current is not observed until the applied potential approaches 0.5 V vs. Ag|AgCl. This potential difference, referred to as overpotential in electrochemistry, is 0.98 V. This approximately one-volt overpotential indicates sluggish kinetics and suggests serious energy inefficiencies.[64] Moreover, side reactions, such as water oxidation, are increasingly likely under this high applied potential, resulting in undesirable byproducts and electrode surface fouling.[8,11,13,14,63,64] Additionally, the current shown in Figure 1.3 is in μA cm^{-2} region, lower than most well-studied electrochemical systems,[64] representing very low reaction rate.

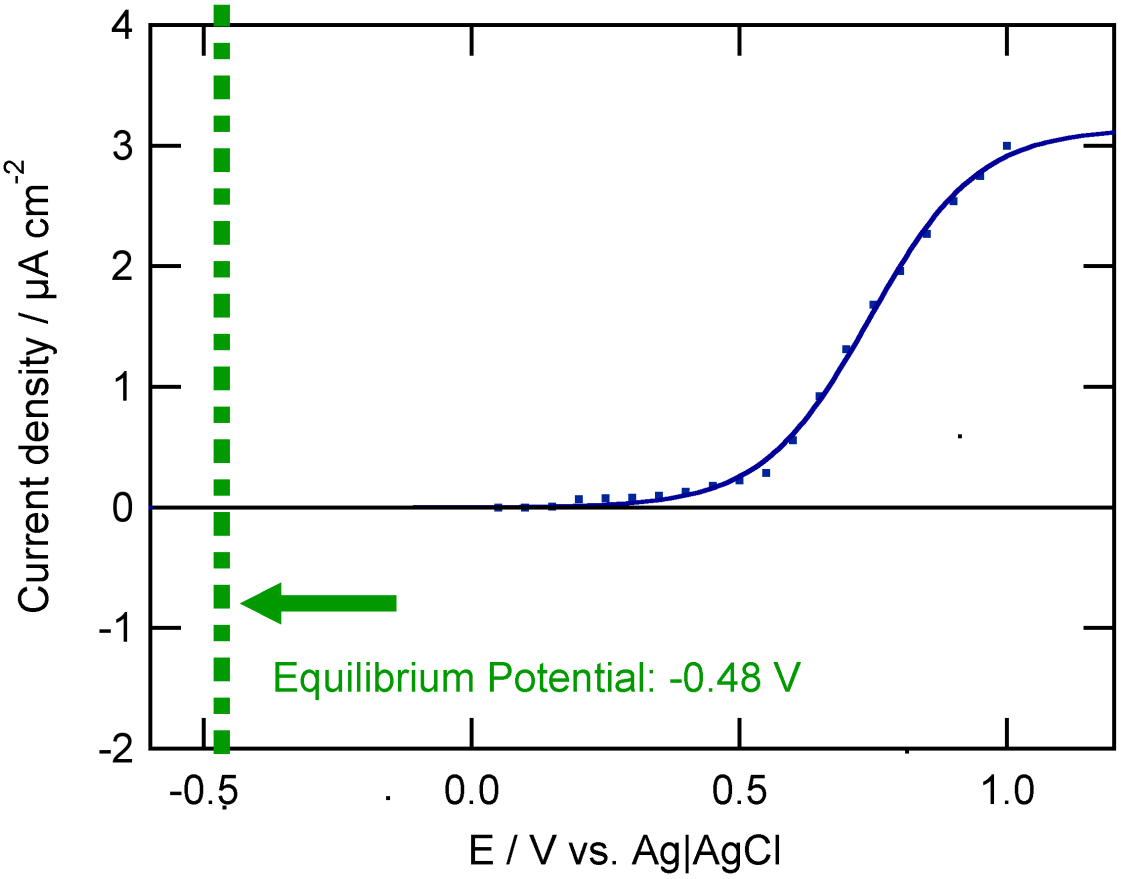

Figure 1.3 NADH electro-oxidation at conventional electrode

To reduce the oxidation overpotential, one approach is to employ an electrocatalyst (Figure 1.4), including electroactive polymers such as poly(azines),[14,65-68] conducting polymers such as poly(aniline),[27] metal oxides,[20,69] and NADH-oxidizing enzymes such as diaphorase.[29] Karyakin used the electropolymerization method to deposit azines on glassy carbon electrodes and observed improved activity towards NADH oxidation.[14] This electrode modification approach in many cases possesses high loading of electrocatalyst, high reaction rate and good stability of the modified layer.[63,70,71] Bartlett *et al.* electrodeposited poly(aniline) on

microelectrodes and observed electrocatalytic activity at 0.6 V vs. RHE.[27] This method demonstrates fast charge transport and can be used in micro-electrochemical transistors. Kim *et al.* employed tin oxide[20] and iron oxide[69] as electrocatalysts for NADH oxidation, where no mediator or chemical treatment is needed. To obtain high power density, Palmore *et al.* utilized diaphorase and benzyl viologen in their biofuel cell system incorporating NADH-dependent enzymes.[8,29] Diaphorase, as NADH oxidizing enzyme, has high selectivity and good activity. Nevertheless, the introduction of the secondary catalysis: benzyl viologen, increases the complexity of electrocatalysis.

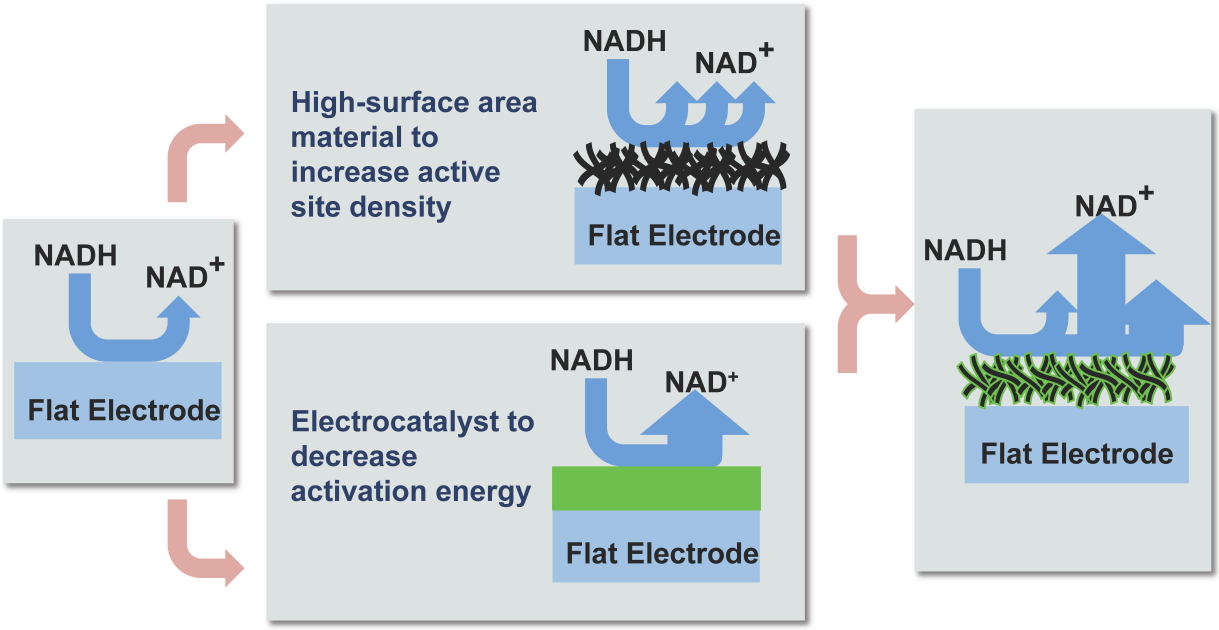

Figure 1.4 NADH electrocatalysis systems

Another effective approach to lower the overpotential is to increase the electrocatalytic active site density via high-surface area materials such as carbon nanotubes (CNT)[37,43,50,72-75]

and graphene.[30] Zhao *et al.* employed chemical vapor deposition to coat CNT on carbon supports.[37] The resulting CNT-modified fiber shows 200 mV decrease of overpotential for NADH oxidation.[37] Kumar *et al.* modified graphite electrode with functionalized graphene and observed sensitive amperometric response to NADH.[30]

Recently, to achieve high-rate NADH electrocatalysis, a combination of electrocatalysis and high surface area has attracted attention. For example, Villarrubia *et al* have achieved electropolymerization of methylene green (a commercially available dye) on CNT based "Bucky Papers" and observed electrochemical activity towards NADH oxidation and L-malate oxidation.[76] Table 1.2 displays some works regarding NADH electrocatalysis. To the best of our knowledge, the reported steady-state current densities for NADH oxidation were still far less than 1 mA cm^{-2} under low overpotential (such as 0.6 V/RHE).[8,11,13,14,24,27-30,37,63,65-69,77-89] Thus, exploring effective electrode fabrication approaches to improve the electrocatalysis of NADH oxidation is still a challenge.

Table 1.2 Some of recent reported NADH electrocatalysis systems

Approach		Applied potential vs. RHE (mV)	i_{max} ($\mu A/cm^2$)	i_{max} (μA)	Data source
NADH-oxidizing enzyme	Diaphorase (DI)-Os complex-SWCNT-Graphite	703	47	3.3	147
	E. coli flavohemoglobin (HMP)-Os complex-Graphite	913	-----	150	148
High surface-area material	Graphene-GC	1100	240	17	48
	Graphene Oxide-Screen printed carbon (SPCE)	1000	47	1.4	149
	MWCNT/polymer binder-GC	650	198	14	74
Electrocatalyst	Ru-complex-GC	670	~120	~8	150
	Quercetin-Pencil graphite	877	50	3.5	151
Incorporation of high surface-area material and Electrocatalyst	MWCNT-PMG/Os Complex	930	240	17	72
	Poly(phenosafranin)- basal plane pyrolytic graphite/GC	910	~160	~40	152
	PMB/MWCNT/SPCE	813	25	-----	73
	Poly(phenosafranin)-SWCNT	613	99	7	153
	PMG -"Bucky paper"	913	-----	600	76
	PBCB-SWCNT-GC	685	-----	1.2	53
	DAB-MB-SWCNT-GC	663	8.49	0.6	77
	Meldola blue-CNT-GC	505	1.6	0.4	154
	Thionine-CNT-Nafion/GC	537	28.3	2	155
	TBO-MWNT-GC	655	-----	45	156

Development of effective NAD^+ reduction electrocatalysts is still ongoing. These electrocatalysts can be classified into four groups: diaphorase (DI, one NAD^+ reducing enzyme),[90-95] Ru complexes,[96-98] dye-modified-electrodes,[61,99-101] and other approaches such as tin oxide[20] and direct reduction using Au and Cu.[102] Some good catalysts for NADH oxidation, such as poly(azine) and CNT, were found to show high overpotential and large background currents towards NAD^+ reduction electrocatalysis.[103] Nevertheless, these results may be improved upon by modified experimental conditions, such as the introduction of Zn^{2+}, as reported by Arechederra *et al* for poly(neutral red) modified electrodes.[68]

1.6 Bioactivity of electro-generated NAD^+

Although many materials have been demonstrated to possess activity for NADH electrocatalysis, there are few reports verifying the bioactivity of electrogenerated NAD^+ by NADH oxidation, especially for high-rate electrodes.[48,51,54,76,104-111] As suggested by Elving *et al*,[112,113] Chi *et al*[71] and Gorton *et al*,[104,114] the mechanism for NADH electrochemical oxidation follows an electrochemical-chemical-electrochemical (ECE) pathway:

$$\mathrm{NADH} \xrightarrow{-e^-} \mathrm{NADH}^{\bullet +} \xleftarrow{-H^+} \mathrm{NAD}^{\bullet} \xrightarrow{-e^-} \mathrm{NAD}^+ \qquad [1.3]$$

The first step of NADH electrocatalysis is deprotonation to $NADH^{\bullet+}$, which leads to the conversion of NADH to $NAD^{\bullet}$ radicals after releasing one proton. The $NAD^{\bullet}$ radicals may subsequently dimerize to NAD_2 or react with the solvent medium, resulting in non-bioactive products.[112] Similarly, Karyakin *et al* have reported that non-bioactive 1,6-NADH (shown in Figure 1.1) is generated as a byproduct in NAD^+ electroreduction.[61] Thus, it is crucial to verify enzymatic activity of the products of NADH electrooxidation.

In the late 70s, Kelly *et al* demonstrated enzymatically active NAD^+ that was generated on a carbon electrode using alcohol dehydrogenase.[111] Their optimal applied potential was as high as 1.2 V vs. RHE and at least 6 hours were required to achieve more than 80% NADH conversion.[111] Laval *et al*,[106,107] Bonnefoy *et al*,[108] and Fassouana *et al*,[109] used RVC electrodes and reported turnover numbers above 3000 s^{-1}. Nevertheless, a similarly high applied potential was needed.[106-109] To reduce this overpotential, Tse *et al*, for the first time, utilized chemically modified electrodes (CME) for NADH electrocatalysis and confirmed that the product was enzymatically active NAD^+.[105] The current was observed only in μA range, indicating a low kinetic rate.[105]

Recently, researchers have explored and characterized advanced materials for NADH electrocatalysis. Zhang *et al* fabricated graphene oxide and reduced graphene oxide modified

screen-printed electrodes to oxidize NADH,[48] and observed NADH oxidation by monitoring the absorbance at 260 nm and 340 nm in spectroscopy.[48] But they did not verify the enzymatic activity of the electro-generated NAD^+.[48]

NAD^+ was generally introduced as a reactant when characterizing such electrodes, preventing observation of bioactivity in purely electroregenerated NAD^+.[54,76,110] Alpat *et al* developed an alcohol dehydrogenase biosensor based on NADH electrocatalysis by toluidine blue O,[51] and their report indirectly confirmed that the generated NAD^+ was enzymatically active, since their system did not contain NAD^+ in the initial operation conditions.[51] However, the quantitative efficiency of NADH electrocatalysis, which we define as the percentage yield of enzymatically active NAD^+ produced by electro-oxidation of NADH, has remained unclear.[51]

1.7 Further facilitation of NADH electrocatalysis

After developing an effective electrocatalysis system for NADH oxidation and verifying the bioactivity of product NAD^+, we would like to explore whether it is possible to further facilitate NADH electrocatalysis in order to accelerate the development of bioelectrocatalysis where NADH-dependent dehydrogenases are involved.

Carbon surface reactivity may be increased by activation. The key principle of carbon material activation is to modify its surface chemistry by increasing surface roughness and introducing carbon-oxygen functionalities.[115-127] Typical activation approaches include laser

irradiation,[125,128] high-intensity ultra-sonication,[124] and heat treatment.[122] Electrochemical pretreatment has attracted extensive interest because of its effectiveness in mild operation conditions.[115-121,123,126]

In this dissertation, three types of carbon materials have been considered regarding electrochemical activation in order to increase reactivity: glassy carbon, carbon paper, and carbon nanotubes. Glassy carbon (GC) is a widely used conventional electrode material in electrochemical systems due to its high conductivity, hardness and inertness.[129] Recent reports regarding glassy carbon activation involve cyclic voltammetry[120] and constant potential[121] approaches.

Carbon papers consisting of carbon fibers has been studied due to their high porosity and low cost.[130] The treatment of CNT is also important towards its electrochemistry activity, especially the introduction of hydrophilicity.[75,131-133] Oxidative treatment of CNT is a key method for increasing their hydrophilicity.[75,131-133]

1.8 Kinetics and transport in bioelectrocatalysis

1.8.1 Rotating disk electrode (RDE)

The rotating disk electrode (RDE) is a technique to study electrode kinetics and has been applied to many electrochemical systems.[24] As shown in Figure 1.5, in RDE, an circular electrode with known surface area rotates during experiments, inducing a flux of electrolyte to

the electrode.[134] The main advantage of the RDE technique is the ability to precisely control mass transport to the electrode by manipulation of disk rotating speed and to be solved analytically.[24] The corresponding current of RDE can be expressed by the Koutecký-Levich equation:[24,135]

$$\frac{1}{i} = \frac{1}{nFAk\Gamma C} + \frac{1}{0.62nFAD^{2/3}v^{-1/6}C\,\omega^{1/2}} \qquad [1.4]$$

where i is current, C is reactant concentration, n is the number of electrons transferred, F is the Faraday constant, k is one-step reaction rate, D is the diffusion coefficient, Γ is the surface coverage of the electrocatalyst, A is the electrode surface area, v is the kinematic viscosity, ω is the angular velocity of the rotating disk electrode. The flux towards the electrode can be precisely controlled by adjusting ω.

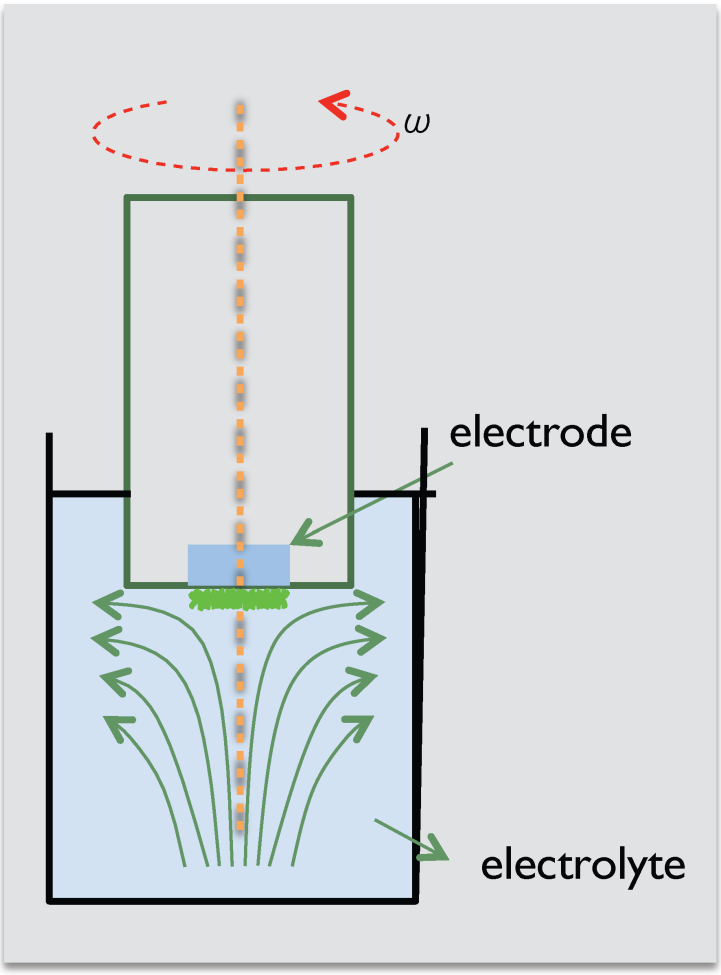

Figure 1.5 Rotating disk electrode (RDE) scheme

Treimer *et al* extended the application of RDE to other charge-transfer mechanisms.[136] Karyakin *et al* [82] and Gorton *et al*[63] applied this equation to NADH electrochemical oxidation, based on which Kar *et al*[137] proposed that NADH electrocatalysis can be related to applied potential and NADH concentration at the electrode surface via the following relation:

$$i = i_{\max}\left(\frac{C_S}{K_S + C_S}\right)\left\{\frac{\exp[(V-U)/b]}{1+\exp[(V-U)/b]}\right\} \quad [1.5]$$

This model of current density, i, for NADH electrocatalysis involves two-independent variables (C_S and V) and four parameters (i_{max}, K_S, U and b). C_S is the surface concentration of NADH; V is the applied electrode potential. The NADH concentration dependency reflects Langmuir heterogeneous adsorption of NADH at electrode surface, with an adsorption coefficient K_S. The exponential term represents Nernstian potential dependence with U as the half-wave potential and b as the exponential coefficient. i_{max} is an adsorption-controlled plateau current density at high surface concentration ($C_S \gg K_S$) and high applied potential (V - U $\gg b$).

1.8.2 Kinetics and mass transport model

Due to the complexity of bioelectrocatalysis, quantitative modeling is vitally important to explain and predict experimental phenomena and design bioelectronic interfaces. The kinetics of the system can be simplified into two steps: the electrocatalytic regeneration of cofactor NADH/NAD^+ and the enzymatic reaction of substrate using dehydrogenase, as shown in Eq 1.1 and Eq 1.2.

To optimize the performance of the interface, it is necessary to explore the mechanism of substrate/product transport, electron transport, and enzyme kinetics. The reaction-diffusion model of the interface results in highly non-linear differential equations, which can be solved by numerical or analytical approaches under specific conditions. Analytical solutions are generally

based on the determination of suitable limiting cases where the diffusion and kinetics can be linearized and solved.[138,139] For example, the paper by Bartlett and Pratt develops approximate analytical analysis and related numerical solutions. They also provide concentration profiles in various limiting cases.[140] Based on Bartlett *et al*'s model, Manimozhi *et al* reported the analytical solutions for non-Michaelis-Menten kinetics of the enzymatic reaction.[141] Meena *et al* studied the non-linear reaction diffusion equations for direct reaction of substrate at microdisc electrode surface.[142] Barton developed a model of a porous carbon electrode based on redox hydrogels, where the morphological properties of the carbon support such as porosity, fiber diameter, and surface area were studied.[143] Kar *et al* described a modeling study of bioanode in methanol/air fuel cell where enzymes and electrocatalyst are entrapped in a porous film whereas cofactor NAD^+ is present in the bulk solution.[137] Nevertheless, there is still no quantitative model involving reversible enzyme kinetics and cofactor immobilization.

1.9 Overview of dissertation

This dissertation concerns the design and engineering of high-performance cofactor regeneration at nanostructured interface, enabling its application in bioconversion, biosensor and bioenergy processes.

Chapter 2 describes fabrication of modified electrodes for high-rate cofactor regeneration. Nanostructured interfaces were obtained by electropolymerizing azines on a carboxylated CNT modified electrode with high-surface area, uniform, controllable properties, and excellent

electrocatalytic activity towards NADH oxidation. Steady-state reaction rate was characterized by a quantitative model incorporating concentration and potential dependence.

Chapter 3 extends the incorporation of poly(azine) and CNT to carbon paper support and verified the bioactivity of NAD^+ electrogenerated spectroscopically. A mathematical model calibrated by measurements of NADH oxidation at PMG-CNT-modified glassy carbon electrodes was applied to predict transient NADH consumption.

Chapter 4 describes a novel approach to further facilitate NADH electrocatalysis. Electrochemical activation of carbon material yields carbon-oxygen functional groups. The resulting electrode demonstrates catalytic activity towards NADH oxidation. Methylene green deposition on activated carbon electrode is achieved by direct adsorption, which turns out to be better NADH oxidizing interface than electropolymerized PMG.

Chapter 5 demonstrates quantitative models for dihydroxyacetone production coupled with cofactor electrochemical regeneration. A two-step kinetics model was developed to describe the reactions in bioelectrocatalysis involving NADH electrochemical regeneration. Planar and porous interface structures are modeled to simulate, predict and evaluate the kinetics and diffusion for the bioelectronic interface. Key parameters involve diffusivity of cofactor/substrate, electrocatalytic activity and enzyme kinetics.

Chapter 6 summarizes this work and describes future advancements and recommendations for future research.

2 NADH Oxidation Catalyzed by Electropolymerized Azines on Carbon Nanotube Modified Electrodes

2.1 Abstract

Electropolymerizing azines on a carbon nanotube (CNT) modified electrode, yields a high-surface area interface with excellent electrocatalytic activity towards NADH oxidation. Electrodeposition of poly(methylene green) (PMG) and poly(toluidine blue) (PTBO) on the carboxylated CNT-modified electrodes was achieved by cyclic voltammetry. The PMG-CNT interface demonstrates 5.0 mA cm^{-2} current density for NADH oxidation at 50 mV vs. Ag|AgCl in 20 mM NADH solution. The kinetics of NADH electrocatalysis were analyzed using a quantitative mass-transport-corrected model with NADH bulk concentration and applied potential as independent variables. This high-rate poly(azine)-CNT interface is potentially applicable to high-performance bioconversion, bioenergy and biosensors involving NADH-dependent dehydrogenases.

2.2 Introduction

As described in Chapter 1, to the best of our knowledge, the reported steady-state current densities for NADH oxidation were still far less than 1 mA cm^{-2} under low overpotential (such as 0.6 V vs. RHE).[8,11,13,14,24,27-30,37,63,65-69,77-89] Moreover, there is lack of quantitative kinetic analysis in the literature especially for high-surface area electrode.

In this study, we report poly(azines) deposited on carboxylated-CNT coated electrodes. The CNT layers demonstrate good nanoscale homogeneity via scanning electron microscopy (SEM) and have surface area that is proportional to CNT loading, as demonstrated by electrochemical capacitance measurements. This CNT-coated electrode possesses excellent electrochemical properties such as controllable high active surface area and good reproducibility. The poly(azines)-CNT electrodes oxidize NADH at high current density and low overpotential. Steady-state oxidation was characterized by a simple model incorporating concentration and potential dependence. The experimental findings combined with quantitative analysis indicate that the poly(azines)-CNT based nanostructured interfaces are a promising electrode to high-rate bioconversion, bioenergy and biosensors.

2.3 Experiments and analysis

2.3.1 Chemicals and materials

Carboxylated multiwall carbon nanotubes (CNT) were purchased from Nanocyl (Sambreville, Belgium, catalog number: NC3101). The manufacturer-reported average properties are 9.5 nm diameter, 1.5 μm length, and >95% purity. Carbon paper was purchased from

Electroche, Inc, (Woburn, Massachusetts, catalog number: EC TP1 030). N,N-dimethylformamide (DMF) was purchased from Fisher BioReagents (Hampton, NH). Toluidine blue O (TBO), methylene green (MG), NADH, sodium tetraborate and sodium nitrate were obtained from Sigma-Aldrich (St. Louis, MO). Argon gas was purchased from Airgas (Lansing MI). Sodium phosphate monobasic and sodium phosphate diabasic were obtained from J.T. Baker (Phillipsburg, NJ). All materials were used as received.

2.3.2 CNT coating on carbon support

As reported by Wen *et al,*[157] CNT were dispersed in DMF to create CNT ink with the aid of ultra-sonication. CNT-coated glassy carbon rotating dish electrodes (GC, RDE, 3 mm diameter) were prepared by drop-casting 5 µl 1 mg mL^{-1} CNT ink and dried in vacuum. CNT-coated carbon paper was prepared by air-brushing and dried in vacuum. Such CNT-coated carbon paper was only used for morphology study in this work.

2.3.3 Electropolymerization of azines

TBO and MG monomer solutions were prepared by dissolving 0.4 mM TBO or MG in 0.01 M borate buffer pH 9.1, 0.1 M $NaNO_3$.[14] Before electropolymerization, the CNT-modified electrode was pre-treated by cyclic voltammetry (CV) between -0.6 and 0.1 V vs. Ag|AgCl (4 M KCl) in TBO or MG monomer solution for 10 min to ensure the TBO or MG adsorption. During electropolymerization, CV was performed in TBO or MG monomer solution between -0.5 and 1.5 V vs. Ag|AgCl for 20 cycles.

2.3.4 Morphology characterization

Scanning electron microscopy (SEM, JEOL JSM-7500F, 5.0 kV, 4.5 mm) was used to characterize the morphology of CNT and PMG-CNT on the carbon support. Because the CNT-carbon paper demonstrates the same capacitive surface area per CNT loading as CNT-GC (Data not show), and PMG-CNT-carbon paper also shows similar activity towards NADH oxidation as PMG-CNT-GC (Data not shown), the CNT and PMT-CNT may possess the same properties on GC and on carbon paper. In this work, we use PMG-CNT-carbon paper for morphology characterization. Os coating was used in order to get clear SEM images (Neo Osmium coater, Meiwafosis Co., LTD., Tokyo, Japan).[158] For 5 s deposition time, the thickness of Os is 2.5 nm, as reported by the manufacturer. Energy-dispersive X-ray spectroscopy (EDS) was applied for elemental quantification, using non-Os coated samples.

2.3.5 Electrochemical characterization

All electrochemical characterizations were measured using a potentiostat (Bio-Logic VSP, Knoxville, TN) and rotating disk electrode system (RDE, see section 1.8.1 for details). An Ag|AgCl (4 M KCl) reference electrode was employed with a platinum wire as counter electrode. The electrolyte was purged with argon to exclude oxygen.

To obtain capacitance data, CV was performed in 1 M sulfuric acid 30℃ in the range of 0.78 to 0.88 V vs. Ag|AgCl with scan rates of 50 to 100 mV s^{-1}. Plotting the non-faradaic current as a function of scanning rate, the slope was the capacitance. Assuming a conversion factor of 25 μF cm^{-2} of carbon material,[159] capacitive surface area was obtained.

Characterization of polymer redox peaks was performed by CV with scan rate 50 mV/s in 100 mM phosphate buffer pH 6 and 30℃. NADH oxidation and NAD^+ reduction characterization was performed by chronoamperometry in 100 mM phosphate buffer pH 6 and 30℃.

To obtain polarization curves, working electrode potential was stepped at 0.05 V intervals in the range of -0.2 to 0.4 V in 0.5 mM NADH solution for NADH oxidation and -0.2 to -1.3 V vs. Ag|AgCl in 0.5 mM NAD^+ solution for NAD^+ reduction. Steady-state current density at each potential was recorded after 2 minutes. To obtain NADH concentration profiles, working electrode potential was fixed at 0.05 V vs. Ag|AgCl, and steady-state current density at each NADH concentration was recorded. All steady-state experiments were recorded three times and the averages and standard deviations were reported. All current densities are relative to the geometric surface area of the RDE (0.071 cm^2).

2.4 Analysis of NADH electrocatalysis

As described by Kar *et al.*,[137] current density due to NADH electrooxidation can be related to applied potential and NADH concentration at the electrode surface via the following relation:

$$i = i_{\max}\left(\frac{C_S}{K_S + C_S}\right)\left\{\frac{\exp[(V-U)/b]}{1+\exp[(V-U)/b]}\right\} \qquad [2.1]$$

This model of current density, i, for NADH electrocatalysis involves two-independent variables (C_S and V) and four parameters (i_{max}, K_S, U and b). C_S is the surface concentration of NADH; V is the applied electrode potential. The NADH concentration dependency reflects Langmuir heterogeneous adsorption of NADH on the poly(azine) surface, with an adsorption coefficient K_S. The exponential term represents Nernstian potential dependence with U as the half-wave potential and b as the exponential coefficient. i_{max} is an adsorption-controlled plateau current density at high surface concentration ($C_S >> K_S$) and high applied potential (V - U >> b).[137]

A quantitative mass-transport correction was developed based on the model shown in Eq 2.1. Equating flux to the electrode surface with the surface reaction rate, we have

$$i = nFk_d(C_B - C_S) = i_{max}\left(\frac{C_S}{K_S + C_S}\right)\left\{\frac{\exp[(V-U)/b]}{1+\exp[(V-U)/b]}\right\} \qquad [2.2]$$

where n is the number of electrons transferred in NADH oxidation, n = 2 eq mol^{-1};[14,63] F is Faraday's constant (96485 C eq^{-1}); C_B and C_S are the concentrations of NADH in the bulk and at the electrode surface, respectively; and k_d is a mass transfer coefficient defined by the Levich equation:[64]

$$k_d = 0.62nFAD^{2/3}v^{-1/6}\omega^{1/2} \qquad [2.3]$$

where D is the diffusivity of NADH, v is kinematic viscosity of the electrolyte, and ω is the angular rotation rate of the electrode. The value of D was found to be 1.0×10^{-5} cm^2 s^{-1} by Levich analysis (data not shown), which is comparable to literature values;[136,160,161] The viscosity value, $v = 1.0 \times 10^{-2}$ cm^2 s^{-1}, was obtained from literature.[136] For a rotation speed ω = 900 rpm, Eq 2.3 yields $k_d = 6.0 \times 10^{-3}$ cm s^{-1}.

Eq 2.2 can be rearranged as a quadratic function of C_S, with the solution

$$C_S = \frac{-Y + \sqrt{Y^2 + 4Z}}{2} \qquad [2.4]$$

where:

$$Y = \frac{i_{max}(\exp[(V-U)/b])}{nFk_d(1+\exp[(V-U)/b])} + K_S - C_B \qquad Z = K_S C_B \qquad [2.5]$$

Using Eq 2.1 and 2.4, one can estimate C_S and the current density, i, given values of all other parameters. The estimated current density may be fit to experimental concentration studies, $i(C_B)$ and polarization curves $i(V)$ to obtain estimates of i_{max}, K_S, U and b, as shown in Table 2.2. This fitting was accomplished using the analytical software Igor Pro (Wavemetrics, Inc.).

2.5 Results and discussion

CNT-modified glassy carbon RDEs were prepared at various CNT loadings, and characterized by SEM to assess morphology and by CV to assess capacitance and surface area. Either PTBO or PMG was then electrodeposited on CNT-modified electrodes at two different loadings of CNTs, and these electrodes were further characterized for activity toward NADH oxidation and reduction.

2.5.1 CNT coated carbon support

The typical morphology of the CNT layer on carbon support characterized by SEM was displayed in Figure 2.1a. The CNTs are distributed homogeneously on the carbon support, forming a porous structure with 50 to 200 nm pores. EDS spectra (Figure 2.1c) indicate that only carbon and oxygen exist on the CNT layer. It is likely that oxygen appears as part of carboxyl groups on the CNT surface.

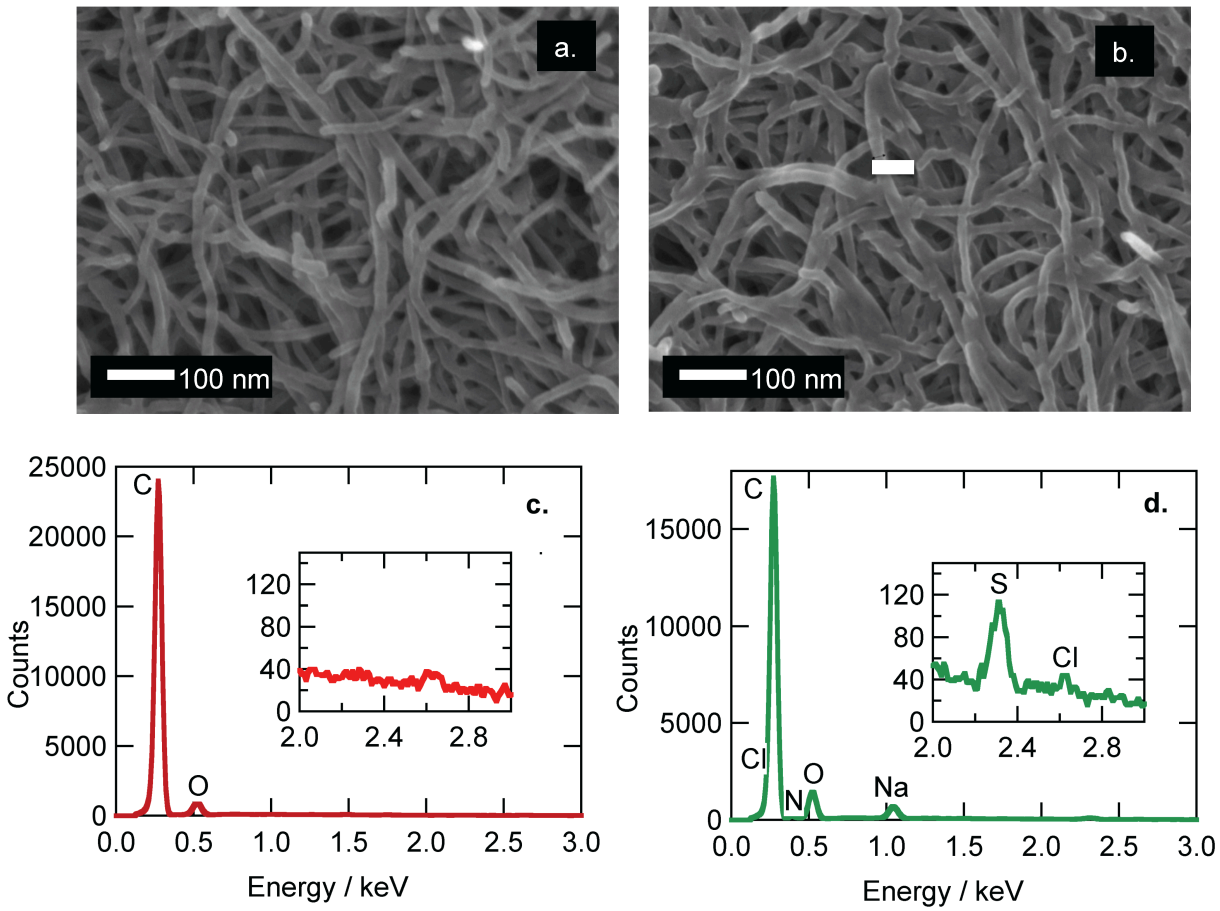

Figure 2.1 Surface characterization of CNT and PMG-CNT. a. SEM image of CNT; b. SEM image of PMG-CNT; c. EDS spectrum of CNT; d. EDS spectrum of PMG-CNT

The capacitive surface area of the CNT-modified electrode varies linearly with CNT loading as shown in Figure 2.2. The observed surface area at 0.85 mg cm^{-2} CNT loading corresponds to a mass-specific surface area of 175 ± 3 cm^2 g^{-1}. This value is at the high end of BET (Brunauer-Emmett-Teller) surface area of multi-walled CNT,[130] indicating that the approach we use here is able to fully utilize the high-surface area property of CNT. Because of this clear linear relationship, it is feasible to control the active surface area by adjusting the CNT loading.

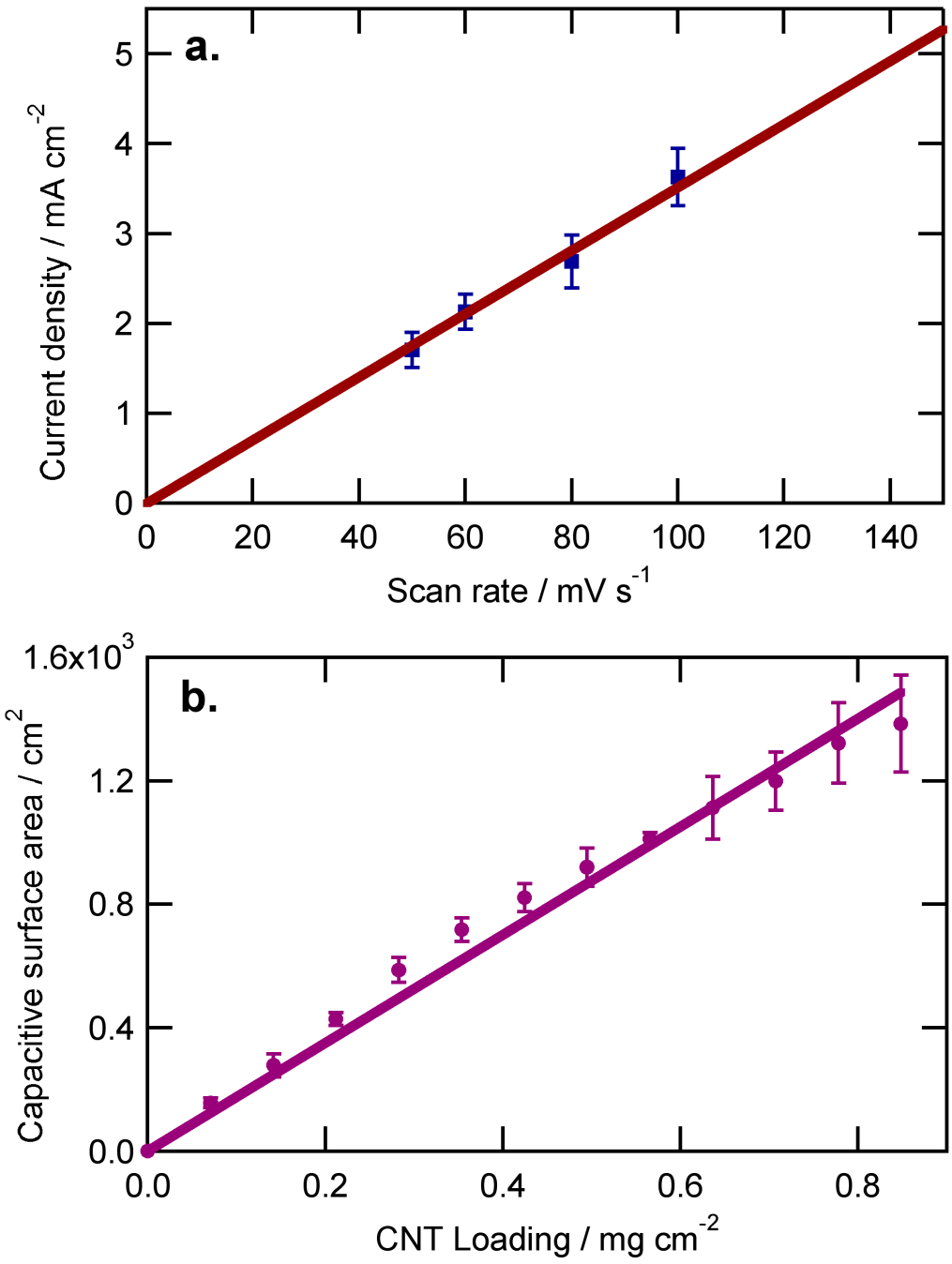

Figure 2.2 a. Capacitive current density varying with scanning rate for 0.85 mg/cm^2 CNT-GC in 1 M sulfuric acid, 30℃. The slope is capacitance. Insert: Examples of cyclic voltammograms at 50 mV/s for three CNT loadings (0.21, 0.50 and 0.85 mg/cm^2). b. Capacitive surface area of CNT-coated glassy carbon electrode, the conversion factor 25 μF cm^{-2} of carbon material was assumed.[159]

2.5.2 Poly(azines) deposited on CNT-modified carbon support

Electrodeposition of poly(TBO) and poly(MG) was achieved by CV. Figure 2.3 shows the chemical structures of TBO and MG.

a. Toluidine Blue O (TBO)

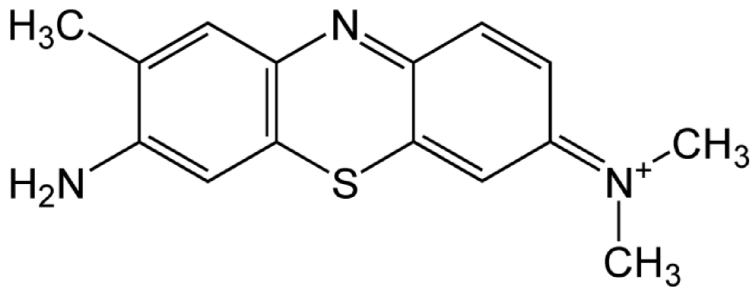

b. Methylene Green (MG)

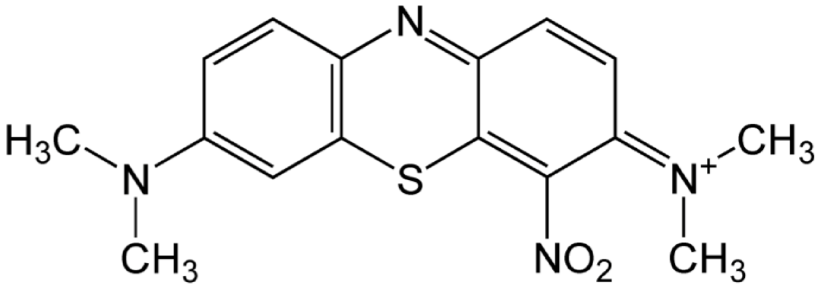

Figure 2.3 Chemical structures of a. Toluidine blue O (TBO) and b. Methylene green (MG).[82]

Typical cyclic voltammograms for electropolymerization of poly(TBO) and poly(MG) are shown in Figure 2.4, in which one can observe three characteristic peaks similar to the PTBO/PMG electropolymerization on bare GC:[67,162,163] The low potential (-0.5 V to 0 V) reduction of oxidized azine according to a one-proton, two-electron reaction;[67,162,163] the

oxidation and desorption of reduced azine in the -0.5 V to 0.5 V range,[67] and the high potential (> 1 V) polymerization shoulder, representing the formation of polymer on the electrode surface by irreversible oxidation of azine.[67] Compared to electropolymerization of PTBO/PMG on a bare GC electrode, the CV in electropolymerization of PTBO/PMG on CNT-modified GC electrode shows 60-fold higher current response. This phenomenon may be due to the large surface area of CNT-modified electrode which leads to a larger amount of electrodeposited PTBO/PMG.[156]

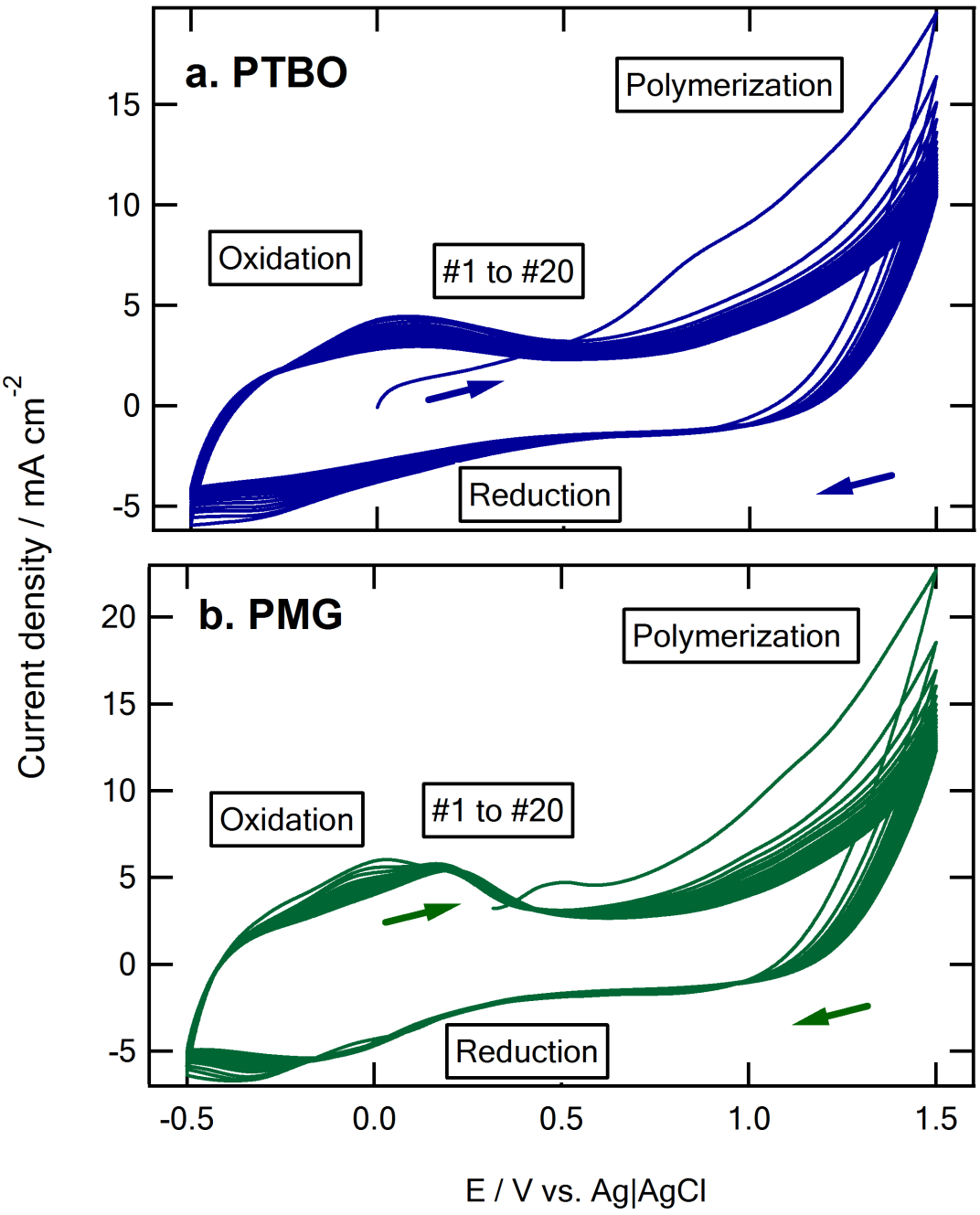

Figure 2.4 Cyclic voltammograms of a. PTBO and b. PMG electropolymerization on 0.85 mg cm^{-2} CNT-coated GC, 20 cycles, 50 mV/s, 0.4 mM TBO, 0.01M borate buffer pH 9.1, 0.1 M $NaNO_3$, 30℃.

The morphology and EDS analysis of the PMG-CNT electrode is shown in Figure 2.1b, 2.1d and Table 2.1. From SEM images, no distinct polymer clusters can be observed, and a slight increase of nanotube diameter can be seen as compared to pure CNT (Figure 2.1a), suggesting that the polymer deposits conformally. EDS analysis indicates a small sulfur peak at 2.3 keV, corresponding to a 560 nmol cm^{-2} sulfur loading after electropolymerization, which suggests a PMG loading of 560 nmol cm^{-2}.

Table 2.1 Elemental quantification on CNT-carbon and PMG-CNT-carbon

Samples	C / %	N / %	O / %	Na / %	S / %	Cl / %
CNT	94.0 ± 0.2	--	5.2 ± 0.2	--	--	--
PMG-CNT	80.8 ± 0.5	1.9 ± 0.4	10.9 ± 0.2	3.6 ± 0.1	2.1 ± 0.2	0.7 ± 0.2

Electrochemical characterization of resulting electropolymerized PTBO/PMG films in phosphate buffer is shown in Figure 2.5. Consistent with electropolymerization voltammetry, the poly(azine)/CNT/GC electrodes show increased current response compared with poly-azines deposited on bare GC, suggesting an increased PTBO/PMG loading. Integration of cyclic voltammetric peaks for PMG deposited on 0.85 mg cm^{-2} CNT-GC (b-3 in Figure 2.5b) yields an active PMG loading of 110 nmol cm^{-2}. This result indicates that ~20 % of the total PMG loading, obtained by EDS, is electrochemically active.

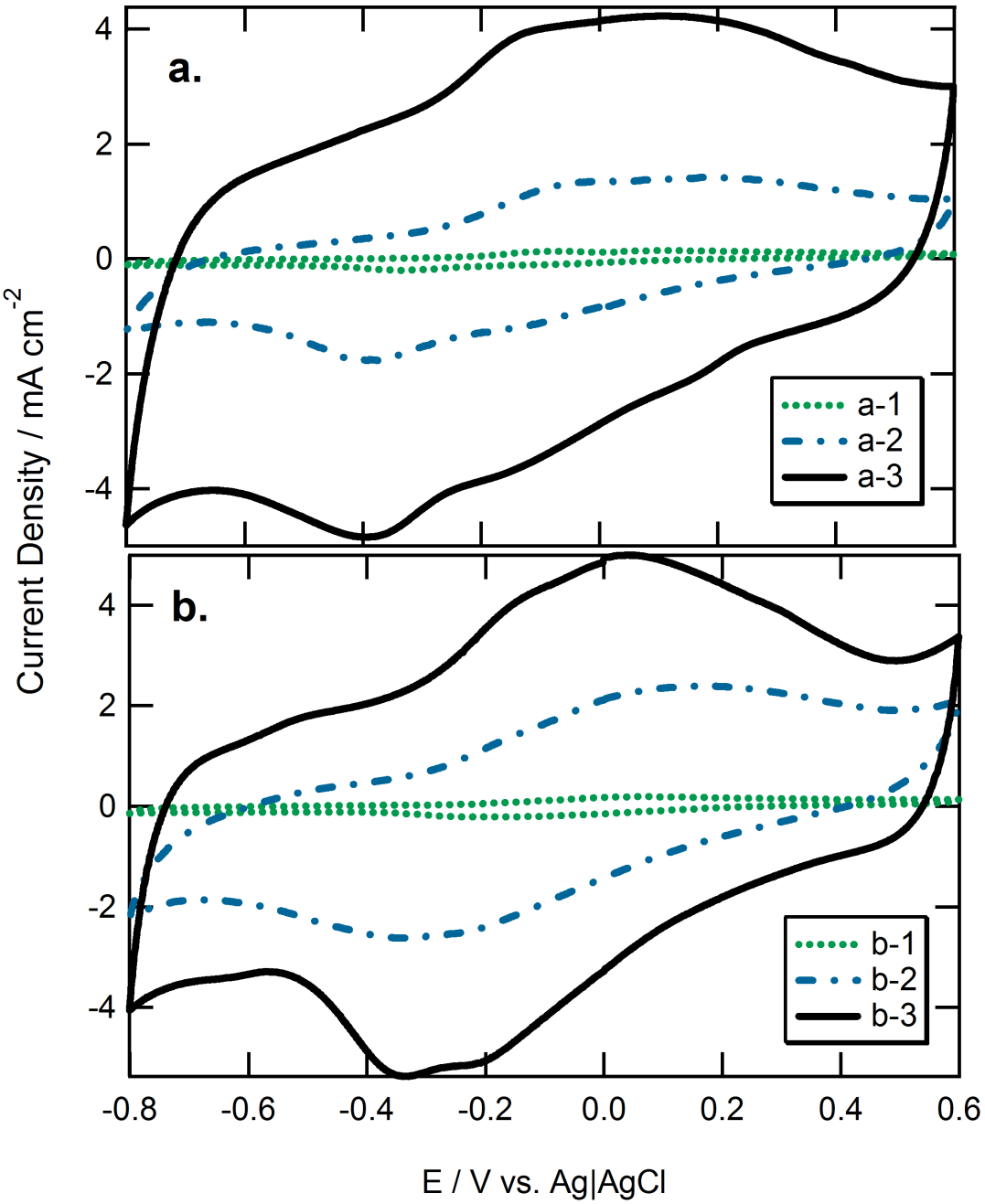

Figure 2.5 Cyclic voltammograms of a. PTBO and b. PMG deposited carbon electrodes (1: Bare GC; 2: 0.21 mg cm^{-2} CNT-GC; 3: 0.85 mg cm^{-2} CNT-GC) in 0.1 M phosphate buffer pH 6, scan rate: 50 mV/s, 30℃.

2.5.3 NADH oxidation on Poly(azine)/CNT electrode

Polarization and concentration studies were performed on modified electrodes at various CNT loadings. Figure 2.6 shows the NADH concentration profiles under fixed applied potential (50 mV vs. Ag|AgCl) on different electrode systems, whereas Figure 2.7 shows polarization curves in fixed NADH concentration (0.5 mM). The mass-transport corrected model was used to fit both concentration and polarization studies simultaneously for each electrode system. Values of parameters i_{max}, K_S, U and b thus obtained are shown in Table 2.2.

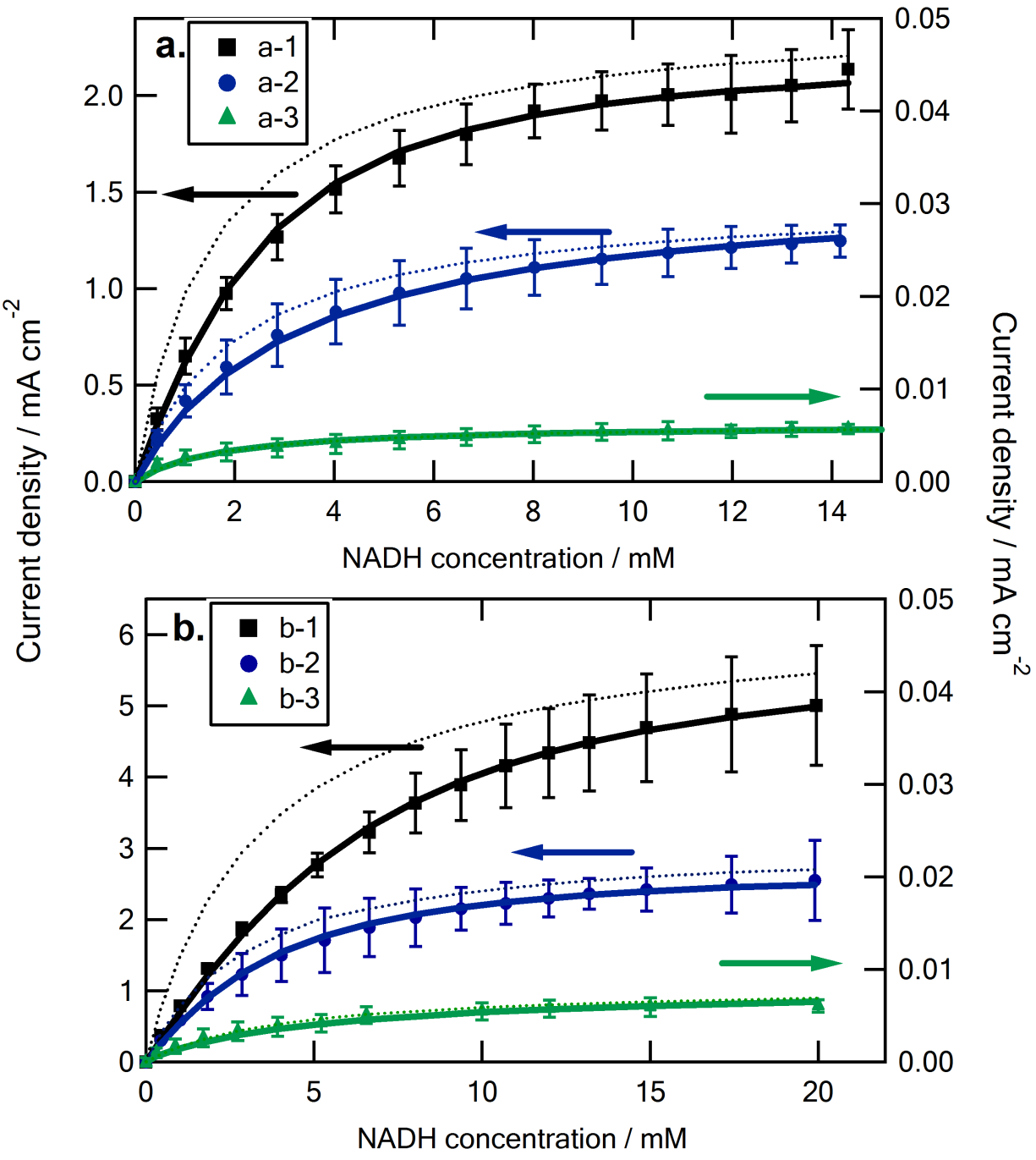

Figure 2.6 NADH concentration study at 50 mV vs. Ag|AgCl in 0.1 M phosphate buffer pH 6.0, 900 rpm, 30℃. a. PTBO, b. PMG. 1: 0.85 mg cm^{-2} CNT-GC; 2: 0.21 mg cm^{-2} CNT-GC; 3: Bare GC. Markers: Experimental data; Solid line: Fitting using mass-transport corrected model; Dashline: Simulation for mass-transport corrected curves

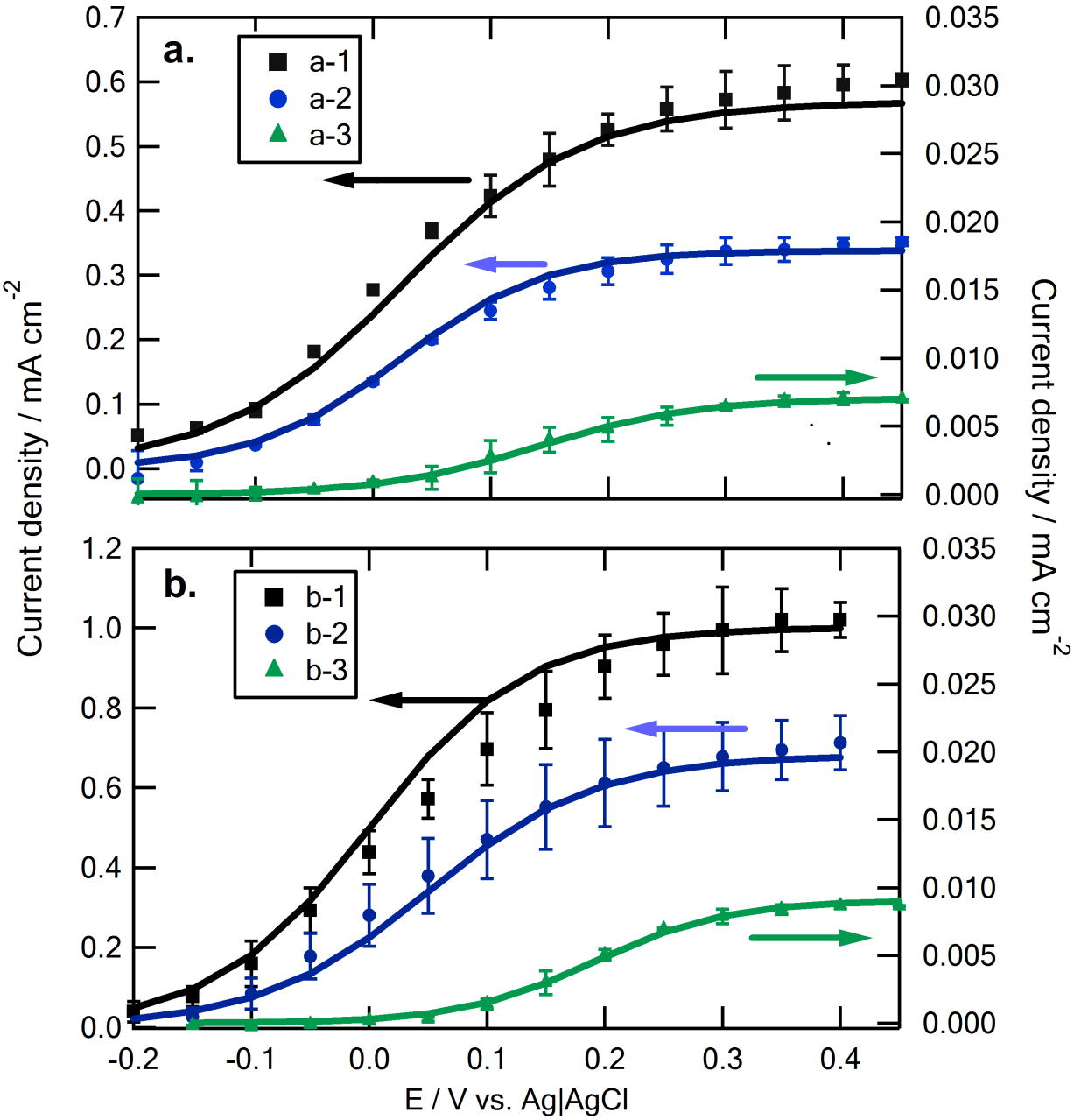

Figure 2.7 Polarization curves for NADH oxidation in 0.5 mM NADH, 0.1 M phosphate buffer pH 6.0, 900 rpm, 30℃. a. PTBO, b. PMG. 1: 0.85 mg cm^{-2} CNT-GC; 2: 0.21 mg cm^{-2} CNT-GC; 3: Bare GC. Markers: Experimental data; Solid line: Fitting using mass-transport corrected model

Table 2.2 Parameter values

Electrodes	i_{max} (mA/cm^2)	K_S (mM)	U (mV)	b (mV)
PTBO-GC	0.029 ± 0.006	1. 7 ± 0.2	141 ± 6	66 ± 4
PTBO-0.21 mg/cm^2 CNT-GC	4.2 ± 0.8	2.0 ± 0.2	100 ± 29	78 ± 19
PTBO-0.85 mg/cm^2 CNT-GC	8.4 ± 1.9	1.5 ± 0.1	110 ± 27	67 ± 11
PMG-GC	0.090 ± 0.0020	4.0 ± 0.6	183 ± 5	58 ± 3
PMG-0.21 mg/cm^2 CNT-GC	15 ± 3	3.0 ± 0.3	125 ± 24	56 ± 10
PMG-0.85 mg/cm^2 CNT-GC	26 ± 4	3.3 ± 0.1	129 ± 15	70 ± 8
0.21 mg/cm^2 CNT-GC	3.6 ± 0.4	2.6 ± 0.1	191 ± 26	101 ± 10

The activities of NADH electrocatalytic oxidation were significantly enhanced by increasing surface area via carboxylated-CNT modification. Maximum steady-state current density i_{max} increased more than 100-fold to 8.4 mA cm^{-2} and 26 mA cm^{-2}, for PTBO and PMG respectively, at 0.85 mg cm^{-2} CNT loading (Table 2.2). Because NADH concentration studies were conducted at low applied potential and polarization curves were conducted at low NADH concentration, far below K_S values, these maximum steady-state current density values were not observed from the experimental data (Figure 2.6-7). However, at NADH concentration C_B = 20 mM, electrode potential V = 0.5 V vs. Ag|AgCl, and rotating speed w = 3000 rpm, a steady-state current density of 20 mA cm^{-2} was obtained, somewhat below the predicted i_{max} (data not shown). However, these conditions are not considered to be of technological interest.

After mass transport correction, the estimated adsorption coefficient, K_S, remains approximately constant with increasing CNT loading (Table 2.2), demonstrating that NADH

adsorption at the polymer surface is not strongly affected by the introduction of nanotubes. Simulated mass-transport corrected curves using these K_S values are shown in Figure 2.6. The shift between simulated curves and experimental data is due to mass transport. Similarly, the mass-transport corrected half-wave potential, *U*, stay approximately constant for CNT-modified electrodes and non-CNT-modified electrodes (Table 2.2).

Figures 2.6-7 and Table 2.2 also demonstrate that electrocatalytic activity differs for PTBO and PMG, consistent with the findings on low-surface area electrodes.[70,82] PTBO-modified electrodes show lower half-wave potential, *U*, than PMG-modified electrodes, but also lower activity, characterized by i_{max}. Additionally, PTBO shows lower K_S values than PMG. Thus, one can observe higher current for PMG-modified electrodes especially at high positive potential region and high NADH concentration. This result may be due to the differences of azine chemical structures, such as additional electron acceptor groups (*e.g.* $–NO_2$) in the aromatic ring, which attributed to higher electrocatalytic activity, while additional proton acceptor groups (*e.g.* $–CH_3$) attributed to lower activity.[70,82]

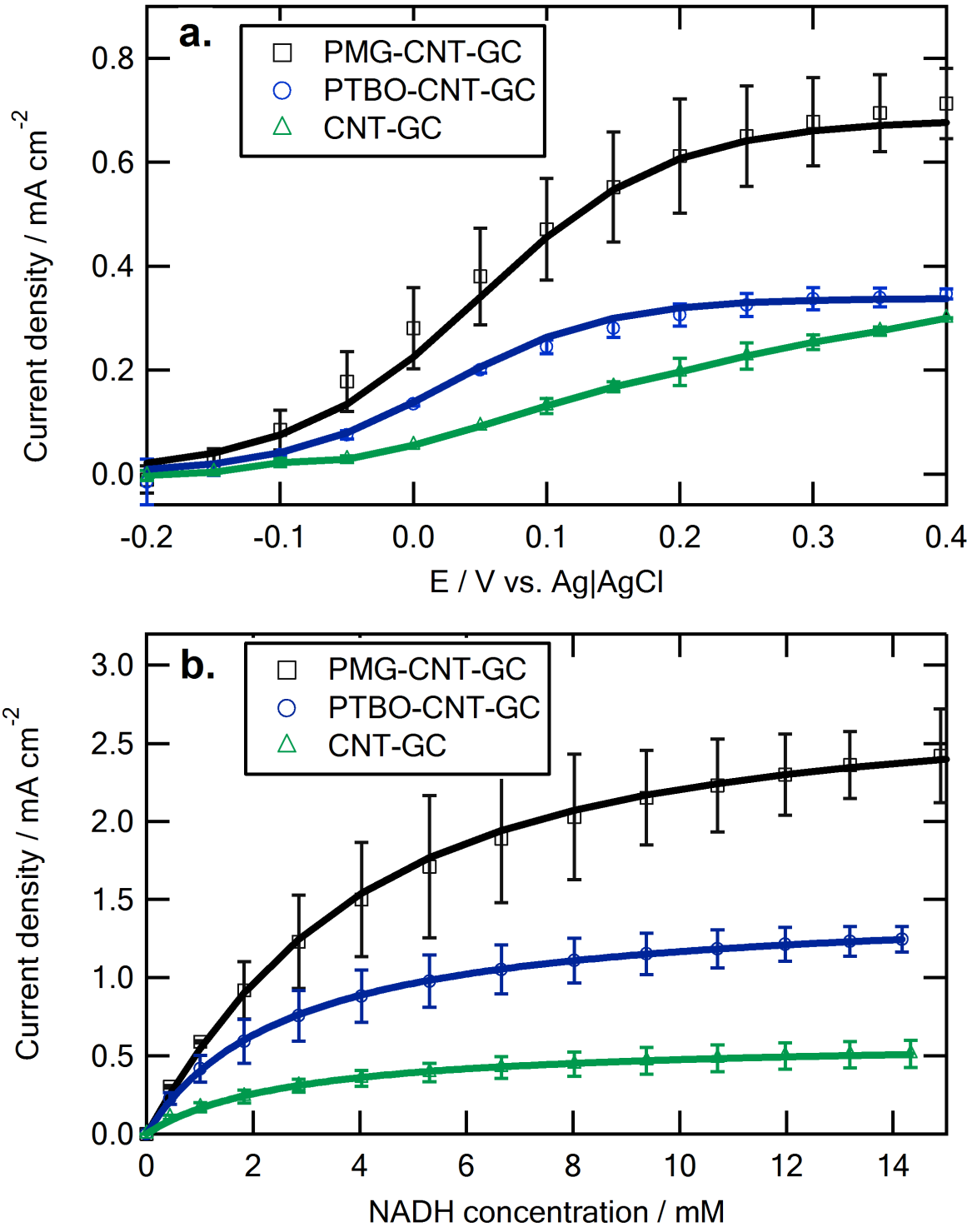

Figure 2.8 Comparison of activities of CNT-GC, PTBO-CNT-GC and PMG-CNT-GC towards NADH oxidation in 0.1 M phosphate buffer pH 6.0, 900 rpm 30℃. a: Polarization curves in 0.5 mM NADH; b: NADH concentration study at 50 mV vs. Ag|AgCl.

As a control, NADH oxidation in the absence of electropolymerized azines was characterized. Figure 2.8 compares polarization curves and NADH concentration profiles for bare and polymer-coated CNT electrodes. From this figure, one can observe that CNT-GC does display activity towards NADH oxidation.[37,43,86,164] However, the observed, activity, i_{max}, is lower and the half-wave potential, *U*, is higher than those of the poly(azines)-CNT-GC (Figure 2.8 and Table 2.2). The observed potential dependence for the bare CNT electrode does not display a plateau, suggesting that the reaction is activation controlled within the applied potential region and is irreversible. These results clearly show the impact of the electropolymerized electrocatalyst on NADH oxidation performance.

2.5.4 NAD^+ reduction on Poly(azine)/CNT electrode

Cathodic polarization studies were performed in oxygen-free electrolyte containing 0.5 mM NAD^+ to assess the activity of modified electrodes towards NAD^+ reduction, as shown in Figure 2.9. Unlike NADH oxidation, side reactions greatly contribute to the observed reduction current. Polarization of the CNT-GC electrode in the presence and absence of NAD^+ are almost comparable, with the background current in NAD^+-free solution attributable to water reduction at such low potential. The PTBO-CNT-GC electrode shows lower background current but the response in NAD^+ is also lower. The PMG-CNT-GC electrode displays a larger background current than in NAD^+ solution, indicating deactivation by adsorbed NAD^+. These findings suggest that, under the experimental conditions used here, PMG-CNT-GC is not active for

NAD^+ reduction, whereas CNT-GC and PTBO-CNT-GC are poor NAD^+ reduction electrocatalysts as a result of their high overpotential and large background currents. These results may be improved upon by modified experimental conditions, such as the introduction of Zn^{2+}, as reported by Arechederra *et al.* for poly(neutral red) modified electrodes.[68]

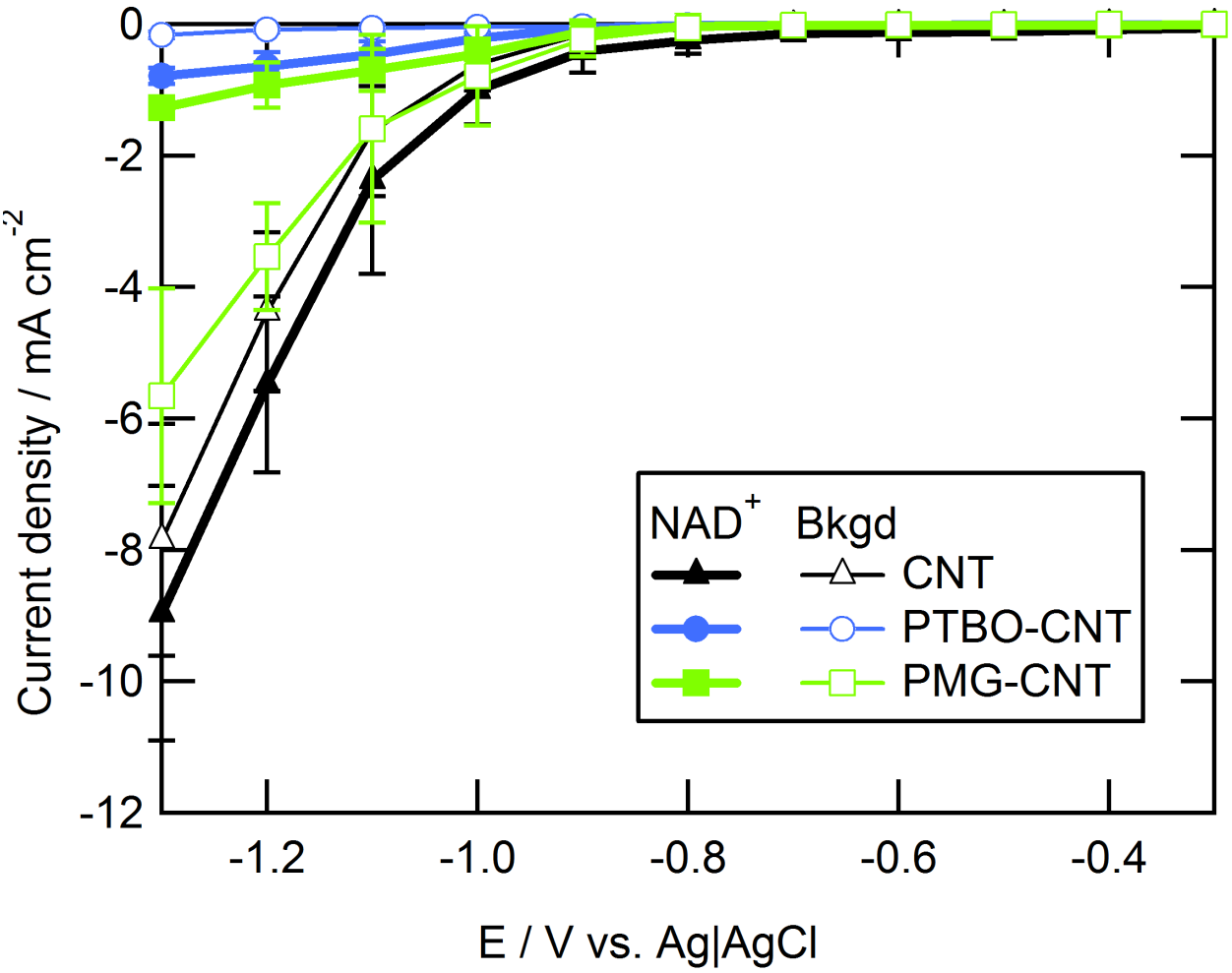

Figure 2.9 Polarization curves of CNT-GC, PTBO-CNT-GC and PMG-CNT-GC towards NAD^+ reduction. 0.1 M phosphate buffer pH 6.0, 900 rpm 30℃ in 0.5 mM NAD^+ and 0 NAD^+ (background) respectively. CNT loading is 0.21 mg cm^{-2} in the three electrode systems.

2.6 Conclusion

Electrodes modified by carboxylated-CNTs demonstrate high capacitive surface area, and allow for modification by electropolymerized azines to yield electrodes with high catalytic activity toward NADH oxidation. Poly(MG) modified electrodes display higher activity than those modified by poly(TBO), especially at high NADH concentration and high overpotential. A mass-transport-corrected mathematical model enabled quantitative characterization of NADH electrocatalysis at steady-state. These poly(azine)/CNT interfaces are applicable for high-performance bioconversion, bioenergy and biosensor processes where NADH-dependent dehydrogenases are involved.

3 Quantitative analysis of bioactive NAD^+ regenerated by NADH electro-oxidation

3.1 Abstract

The bioactivity of NAD^+ electrogenerated at a high-surface area composite anode was verified spectroscopically. The anode was composed of poly(methylene green) electropolymerized on carbon nanotubes (PMG-CNT) which was in turn immobilized on carbon paper. A mathematical model calibrated by measurements of NADH oxidation at PMG-CNT-modified glassy carbon electrodes was applied to predict transient NADH consumption. The model showed good agreement with the experimental data, and 80% conversion of NADH was observed after 1 hour of electrochemical oxidation. Using a spectroscopic enzyme cycling assay, the yield of enzymatically active NAD^+ was verified at 93% and 87% for applied potentials of 500 mV and 150 mV vs. Ag|AgCl, respectively. This suggests that roughly 10% of oxidized NADH may be lost due to dimerization or some other side reaction, after accounting for self decay. These results prove that bioactive NAD^+ can be efficiently produced using electrochemical techniques, enabling application in bioconversion, biosensor and bioenergy processes.

3.2 Introduction

In Chapter 2, we described the fabrication of high-rate NADH oxidizing electrodes which was obtained by electropolymerizing azines on carbon nanotube-modified glassy carbon electrodes, and a mathematical model was developed for quantitative analysis. We tested several electrocatalysts including carbon nanotubes (CNT-GC), poly(toluidine blue O) (PTBO-GC), and poly(methylene green) (PMG-GC) for activity toward NADH electrooxidation, and found that the incorporation of PMG and CNT (PMT-CNT-GC) lead to the highest NADH oxidation rate.[103] In this Chapter, we immobilize PMG-CNT on a carbon paper support in order to construct a high surface area electrode for bulk conversion of NADH to NAD^+. Capacitance measurements on CNT-carbon paper indicate electrochemical properties similar to CNT-GC, including controllable high surface area and good reproducibility. Bulk NADH oxidation was performed on PMG-CNT-carbon paper, with conversion monitored using spectroscopic absorbance at 340 nm. The process was simulated using a kinetic model calibrated with data from rotating disk electrode experiments. Using this enzyme cycling assay, we quantitatively verified the yield of enzymatically active NAD^+ on PMG modified high-surface area electrodes.

3.3 Experimental

3.3.1 Chemicals and materials

NADH, methylene green (MG), sodium tetraborate and sodium nitrate were purchased from Sigma-Aldrich (St. Louis, MO). Sodium phosphate monobasic and sodium phosphate diabasic were obtained from J.T. Baker (Phillipsburg, NJ). N, N-dimethylformamide (DMF) was

obtained from Fisher BioReagents (Hampton, NH). All materials were used as received without further purification. Buffer solutions were prepared with deionized water. Ultrapure argon gas was purchased from Airgas (Lansing, MI). Carboxylated multiwalled CNT (9.5 nm diameter, 1.5 μm length, > 95% purity), were obtained from Nanocyl (NC3101, Sambreville, Belgium). Carbon paper was obtained from ElectroChem (EC TP1 030, Woburn, Massachusetts).

3.3.2 CNT deposition on carbon electrode

CNT modification of carbon electrodes was reported previously.[103,157] Essentially, 2 mg mL^{-1} CNT ink was dispersed ultrasonically in DMF solvent. The CNT-modified carbon electrode (CNT-CP) was fabricated by air-brushing CNT ink on carbon paper (CP) and vacuum drying.

3.3.3 Electropolymerization of methylene green

As previously reported,[14,103] deposition of poly-methylene green (PMG) on CNT-CP was achieved via electropolymerization using cyclic voltammetry (CV) with scan rate of 50 mV s^{-1} between -0.5 to 1.5 V vs. Ag|AgCl (4 M KCl) for 20 cycles in fresh MG solution. MG solution was prepared by dissolving 0.4 mM MG in 0.01M borate buffer, pH 9.1, with 0.1M $NaNO_3$. The resulting MG solution was purged with argon for 20 min to eliminate oxygen. During electropolymerization, argon was continuously bubbled to maintain an oxygen-free solution.

3.3.4 Capacitance characterization

Capacitive surface area was estimated using CV in the narrow potential range from 0.3 to 0.4 V vs. Ag|AgCl (4 M KCl) with varying scan rates from 50 to 100 mV s^{-1} in supporting electrolyte (0.01 M borate buffer pH 9.1, 0.1 M $NaNO_3$, 30°C). This electrolyte was chosen because it serves as buffer solution for electropolymerization. Plotting the current in the non-faradic potential region against scan rate, the slope was recorded as capacitance. Assuming a specific capacitance of 25 μF cm^{-2} for carbon material,[159] electrode surface area was thus evaluated. Prior to electropolymerization of PMG on CNT-CP, capacitance was measured to ensure consistent values for all CNT-CP electrodes.

3.3.5 NADH decay

NADH bulk solution in phosphate buffer pH 6 was magnetically stirred at 1,200 rpm, 30 ºC. For varied initial NADH concentrations, the decay of NADH was monitored using spectroscopic absorbance at 340 nm.

3.3.6 NADH bulk oxidation

NADH oxidation was performed using PMG-CNT-CP as the working electrode, with initial NADH concentration of 0.94 mM in 20 mL pH 6 phosphate buffer at 30°C, constant applied potential of 0.15 V or 0.5 V vs. Ag|AgCl (4 M KCl), and magnetically stirred with a 10 mm × 3 mm stirring bar at 1,200 rpm. The exposed electrode surface area was 0.8 cm^2. The electrolyte was purged with argon to exclude oxygen.

During reaction, the NADH concentration was monitored at 10 min intervals by analyzing 160 μL samples of the reactor solution at 5-fold dilution by absorbance spectroscopy at 340 nm with extinction coefficient $\varepsilon = 6{,}220\ M^{-1}\ cm^{-1}$. To quantify the enzymatic activity of electrogenerated NAD^+, a commercially available enzyme cycling assay (EnzyChrom™ *NAD^+/NADH Assay Kit*, ECND-100) was employed to analyze bulk solution during and after electrocatalysis. The scheme for the cycling assay is shown in Figure 3.1**.** The working reagents of the assay include lactate, lactate dehydrogenase (LDH), diaphorase and formazan (MTT_{ox}), which are underlined in Figure 3.2. The assay kit relies on excess activity of LDH to fully reduce all NAD^+ present to NADH, which in turn reduces the MTT_{ox} reagent via the NADH-oxidizing enzyme diaphorase. After a 15-min reaction time, the absorbance of reduced MTT_{red} measured at 565 nm is proportional to the combined concentration of NAD^+ and NADH, C_{NADtot}.[165-167] The concentration of NADH, C_{NADH}, was obtained by absorbance in the absence of the kit. The concentration of enzyme-active NAD^+ could then be calculated by subtraction: $C_{NAD+,\,active}(t) = C_{NADtot}(t) - C_{NADH}(t)$.

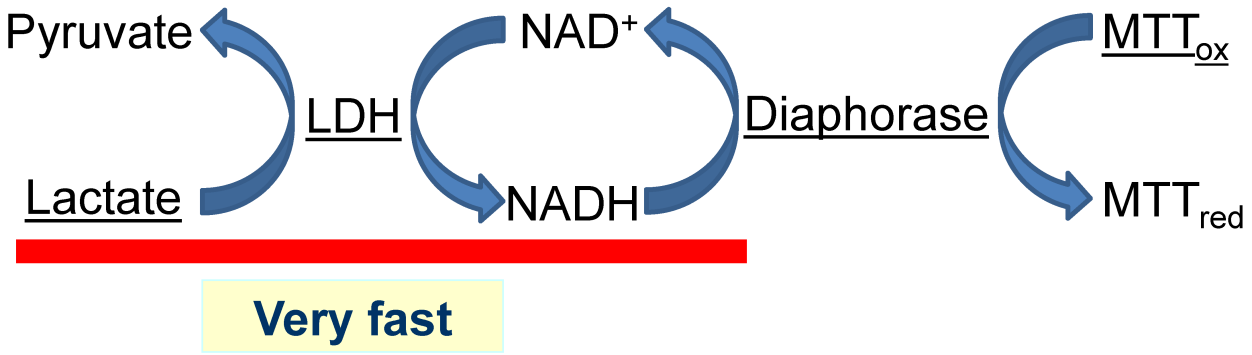

Figure 3.1 Scheme of EnzyChrom™ enzyme cycling assay

3.4 Analysis

NADH electro-oxidation occurs according to the reaction

$$NADH \longrightarrow NAD^{+} + H^{+} + 2e^{-} \qquad [3.1]$$

NADH is consumed in a bulk electrolysis reactor due to the above reaction as well as bulk decay.[168-172] The consumption rate of NADH, R_{NADH} (mM min^{-1}), can therefore be expressed as:

$$\frac{dC_{\mathrm{NADH}}}{dt} = -R_{\mathrm{NAD+}} - R_{\mathrm{decay}} \qquad [3.2]$$

where $R_{\mathrm{NAD+}}$ is the rate of NAD^{+} generation according to Eq 3.1, and is related to electrode current density, j, by:

$$R_{\mathrm{NAD+}} = \frac{j(t)A}{nFV} \qquad [3.3]$$

where A is the geometric surface area of the electrode (0.8 cm^{-2}), V is the reactor volume (initially 20 mL, varying with time as 160 µL samples are withdrawn), n is electron stoichiometric coefficient (2 eq mol^{-1}), and F is Faraday's constant (96,485 C eq^{-1}).

Based on previous work, current density j can be written as:[103,137]

$$j(t) = j_{\max}\left(\frac{C_{\mathrm{NADH}}(t)}{K_{\mathrm{S}} + C_{\mathrm{NADH}}(t)}\right)\left\{\frac{\exp[(E-U)/b]}{1+\exp[(E-U)/b]}\right\} \qquad [3.4]$$

where $j_{\max}$ is the adsorption-controlled plateau current density, K_{S} is the Langmuir-adsorption coefficient, U is the half-wave potential, b is the exponential coefficient, E is the applied potential; and C_{NADH} is the bulk concentration of NADH.

Ambient self-decay of NADH, R_{decay}, can be expressed as a first-order reaction:

$$\frac{dC_{\mathrm{decay}}}{dt} = k_{\mathrm{decay}} \times C_{\mathrm{NADH}}(t) \qquad [3.5]$$

Under the conditions considered in this work, the decay constant k_{decay} was found experimentally (Figure 3.2) to be 0.06 ± 0.01 hr^{-1}, which is within literature values.[171,173] Other

parameters are listed in supporting information. Using an initial NADH concentration of 0.94 mM with no NAD^+ initially present, the conversion of NADH to NAD^+ was simulated using the above equations in MATLAB.

Experimentally, the NADH concentration was measured using spectroscopic absorbance at 340 nm. The expected NAD^+ concentration, $C_{NAD+}(t)$, was calculated using

$$C_{NAD+}(t) = C^0_{NADH} - C_{NADH}(t) - C_{decay}(t) \quad [3.6]$$

where C^0_{NADH} is the initial NADH concentration, $C_{NADH}(t)$ is the measured NADH concentration obtained by spectroscopic absorbance, and $C_{decay}(t)$ is the decayed NADH obtained by integration of Eq 3.5.

The yield of enzymatically active NAD^+ is calculated by:

$$\text{Yield} = \frac{C_{NAD+,active}(t)}{C_{NAD+}(t)} \quad [3.7]$$

where $C_{NAD+,\ active}$ (t) is measured by the EnzyChrom™ assay and C_{NAD+} (t) is obtained from Eq 3.6.

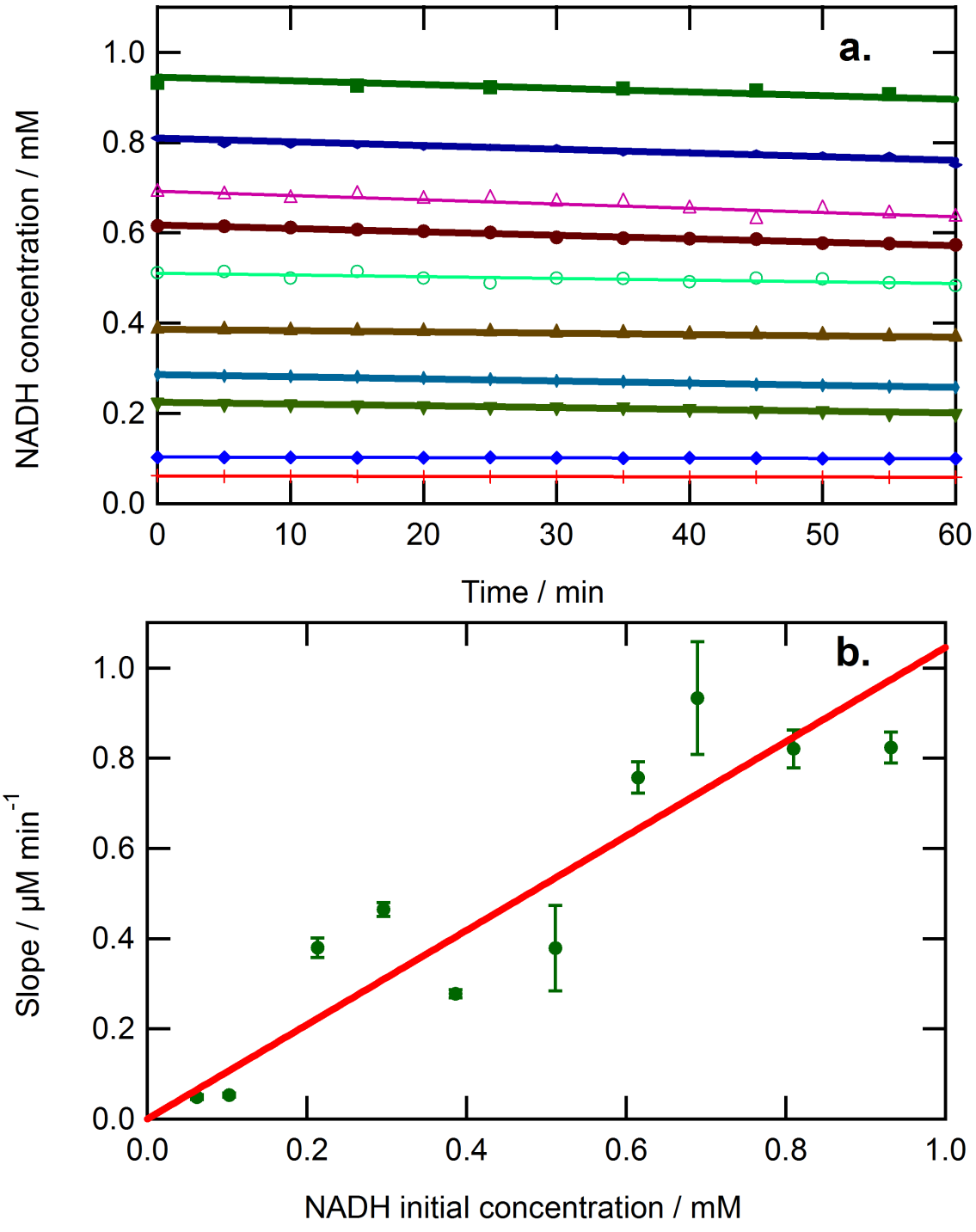

Figure 3.2 The decay of NADH in 0.1 M phosphate buffer pH 6.0, magnetic stirred speed 1200 rpm, 30 °C. a. At varied NADH initial concentrations, NADH decay was monitored using UV-Vis spectra at 340 nm; b. The slopes in a. varying with NADH initial concentration.

3.5 Results and discussion

3.5.1 CNT coated carbon support

Figure 3.3 shows the capacitive surface area of CNT-coated carbon paper compared with CNT-coated glassy carbon (GC) as it varies with CNT loading. The two curves appear to be linear within experimental error, with similar slopes (890 ± 18 and 860 ± 11 cm^2 mg^{-1}, for CNT-GC and CNT-CP-GC, respectively). Therefore, immobilization of carbon paper does not impact the active surface area of the CNT layer, suggesting that the deposited CNT possesses the same properties when supported on carbon paper support as on a GC electrode. The larger experimental error on CNT-CP-GC compared to CNT-GC is likely a result of the increased complexity of assembling the electrode with the additional CP layer.

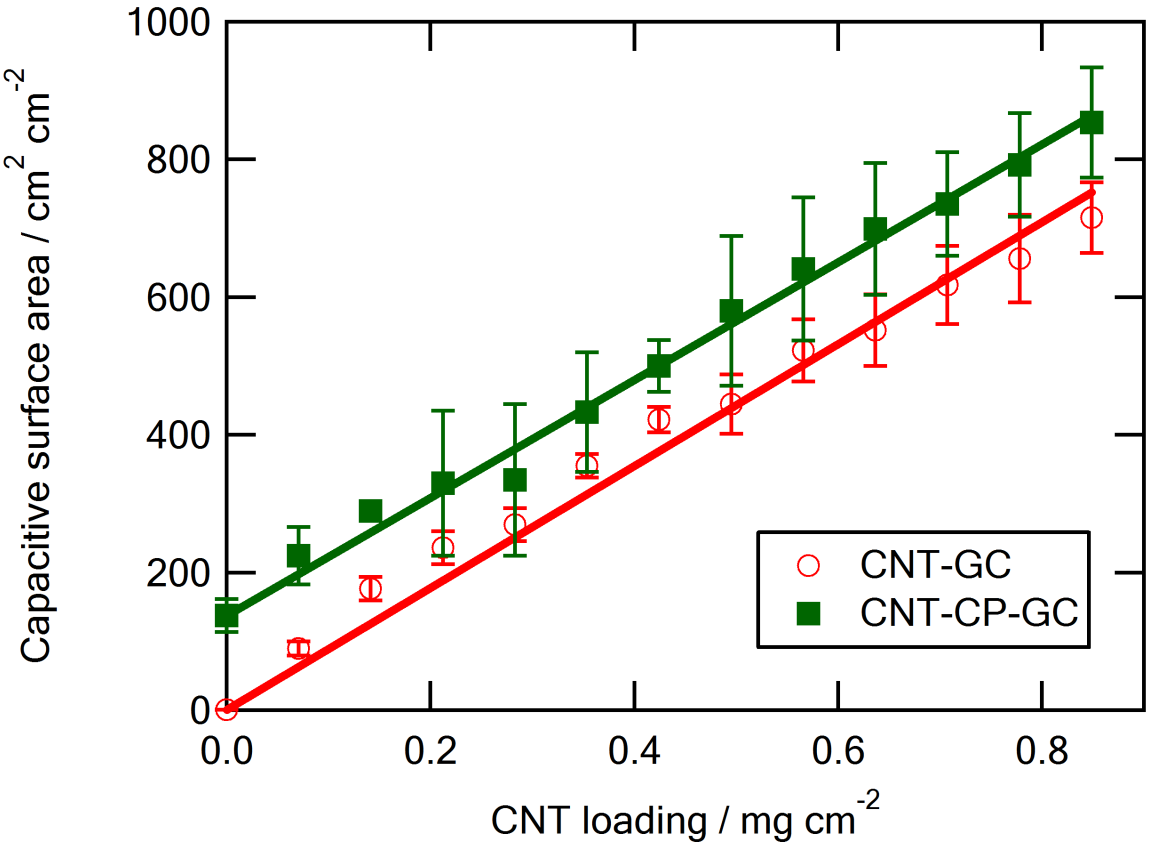

Figure 3.3 Capacitance of CNT-coated carbon paper (CNT-CP-GC) and CNT-coated glassy carbon (CNT-GC) for varying CNT loading, obtained by cyclic voltammetry at varying scan rates in 0.01 M borate buffer pH 9.1, 0.1 M $NaNO_3$, 30 °C, potential range 0.3-0.4 V vs Ag|AgCl.

3.5.2 Conversions in NADH bulk oxidation on PMG-CNT-carbon paper

Poly-methylene green (PMG) was deposited on CNT-CP via electropolymerization in borate buffer. For the current deposition conditions, the loading of PMG was previously found to be 560 nmol cm^{-2} using energy-dispersive X-ray spectroscopy (EDS).[103]

PMG-CNT-CP electrodes were employed in a 20 mL NADH oxidation reactor initially containing 0.94 mM NADH. Figure 3.4 indicates the decrease of NADH concentration with time

(blue squares), showing good agreement with simulation results (dashed lines). In this batch reactor experiment, NADH is consumed by electrochemical reaction and self-decay. Since the NADH concentration (initially ~ 1 mM) is lower than K_S value (3.0 ± 0.7 mM),[103] the electrochemical rate is proportional to its concentration during the bulk oxidation. Because the NADH decay rate is small, NADH consumption is dominated by conversion to NAD^+, and an exponential decrease in concentration is observed in Figure 3.4. The rate of NADH consumption appears to depend linearly on NADH concentration for the entire reaction, and the reaction solution remained homogeneous. From these observations we may conclude that the products of NADH oxidation do not deactivate the electrode, and may be mostly soluble.

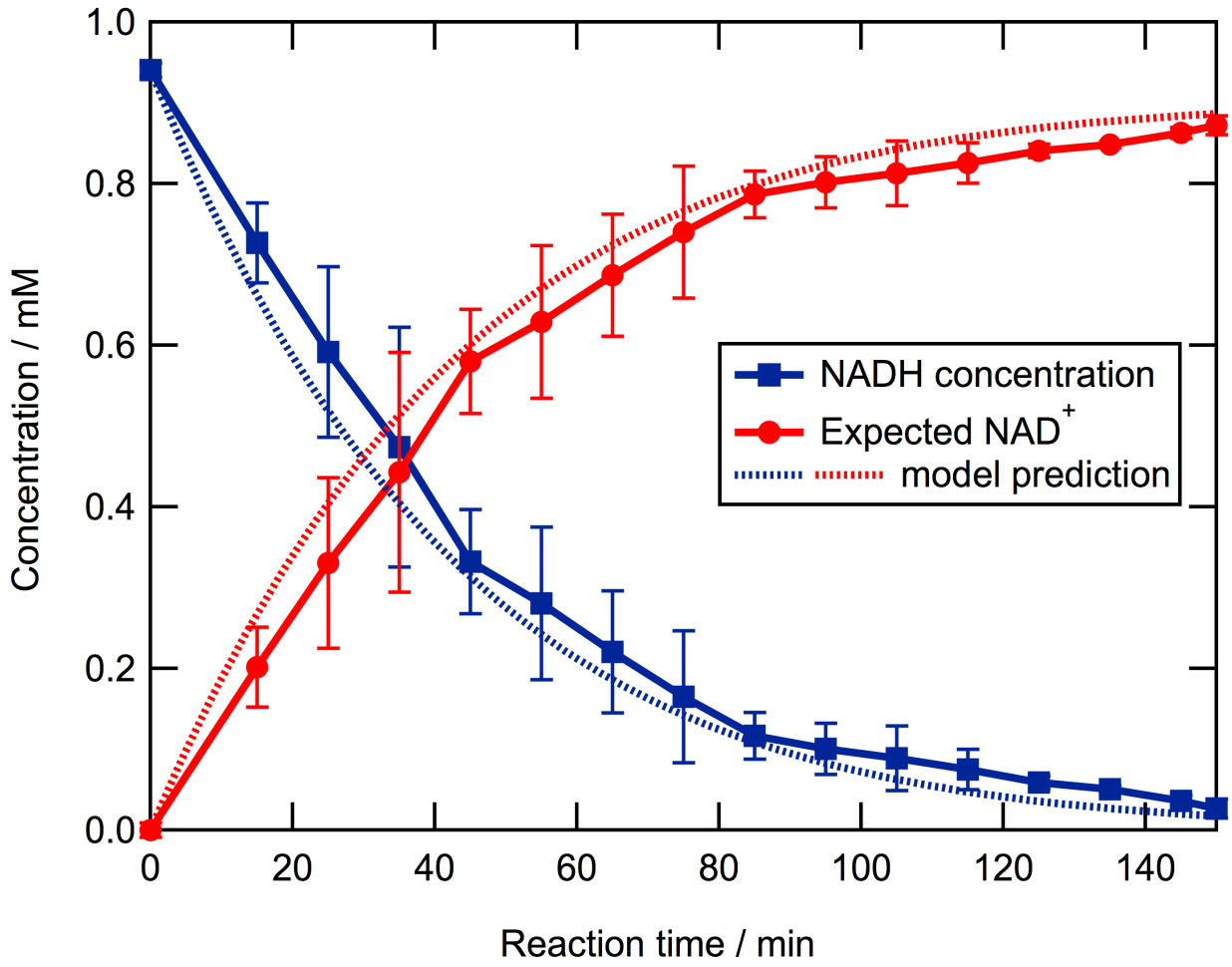

Figure 3.4 Electrochemical oxidation NADH to NAD^+ in a batch reactor using a 0.8 cm^2 PMG-CNT-CP electrode. Markers and solid lines: Experimental data. Dashed lines: Simulation Results; NADH oxidation was performed with NADH concentration initially at 0.94 mM in 20 mL pH 6, 30 °C phosphate buffer, applied potential of 0.5 V vs. Ag|AgCl , with 1,200 rpm magnetic stirring. NADH concentration was measured by spectroscopic absorbance at 340 nm. Expected NAD^+ concentration was obtained by Eq 3.6.

About 80% conversion of NADH was observed after 1 hour, suggesting a high conversion rate. As described by Eq 3.2, NADH may be consumed by either electrooxidation or by self decay. After 150 min of reaction, according to Eq 3.6, 0.87 mM NAD^+ was expected to be generated, accounting for 93% of the initial NADH concentration. Over the same period, 5%

of the initial NADH was predicted to be lost to self-decay, according to Eq 3.5. This indicated that the electrochemical conversion rate was at least 13-fold higher than the decay rate.

3.5.3 Bioactivity of electrogenerated NAD^+

Using the commercially available enzyme cycling assay, the yield of enzymatically active NAD^+ electrogenerated by NADH oxidation was obtained during and after electrocatalysis. The dashed line in Figure 3.5 represents 100% yield of active NAD^+. During NADH electrocatalysis on the PMG-CNT modified electrode, the yield of active NAD^+ stays at a high level. At the end of reaction, 93 ± 6 % and 87 ± 8 % yields were obtained for applied potential at 500 mV and 150 mV vs. Ag|AgCl respectively. This suggests that roughly 10% of oxidized NADH may be inactive due to dimerization or some other side byproduct, after accounting for self decay using Eq 3.5.

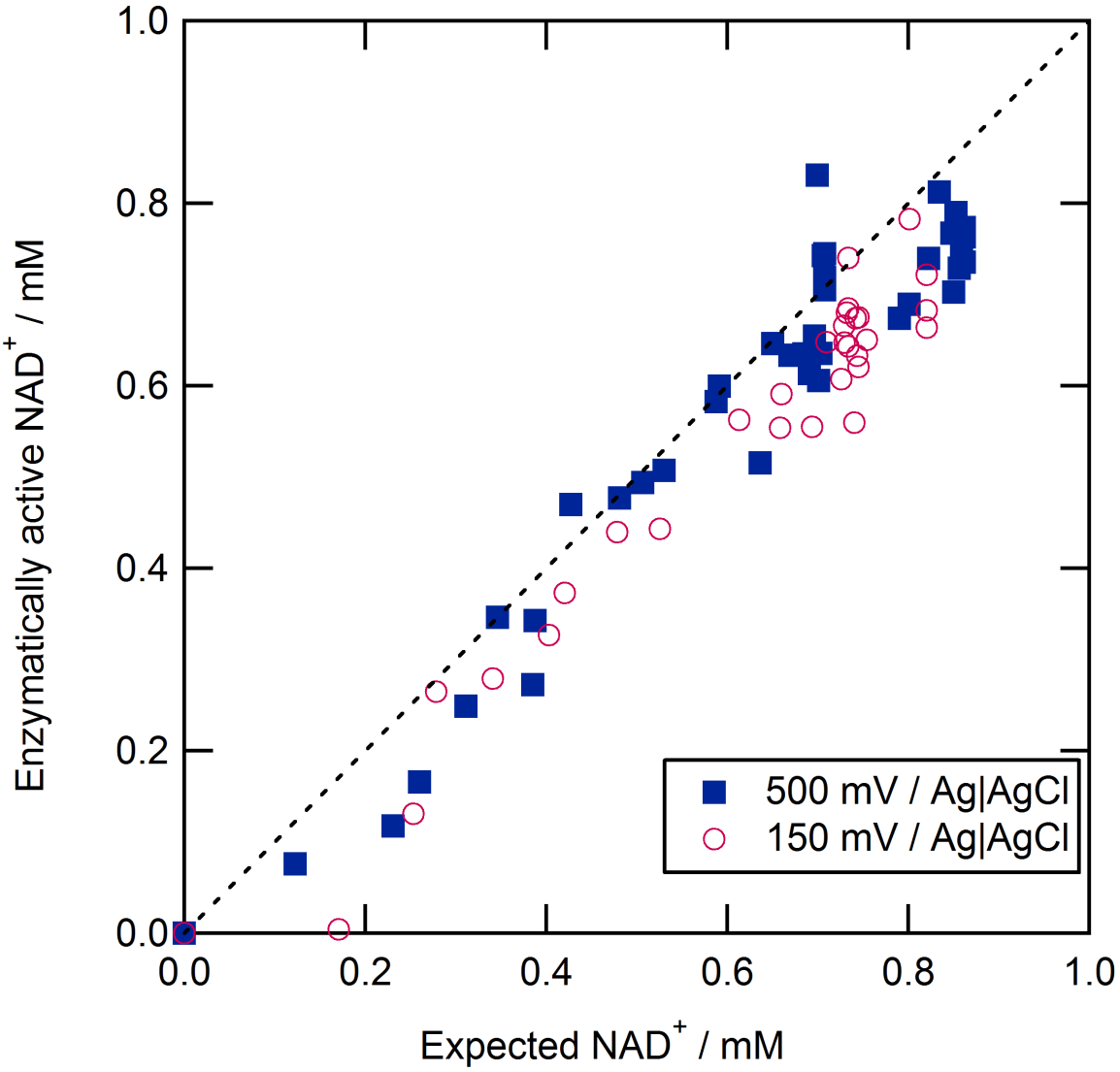

Figure 3.5 The yield of enzymatically active NAD^+ generated by NADH electrochemical oxidation. The concentration of active NAD^+ was measured using enzyme cycling assay kit. Expected NAD^+ concentration was obtained by subtracting measured NADH and decayed NADH from initial concentration.

3.6 Conclusion

Electropolymerizing MG on a carboxylated-CNT modified carbon paper yields a high-surface-area electrode with high oxidative conversion of NADH to bioactive NAD^+. Experimental data in an NADH electro-oxidizing batch reactor shows good agreement with a quantitative mathematical model. These findings demonstrate that a high-surface area poly(azine)-CNT electrode presents a promising approach to regenerating NAD^+ for bioconversion, bioenergy and biosensors.

4 Facilitation of High-Rate NADH Electrocatalysis Using Electrochemically Activated Carbon Materials[1]

4.1 Abstract

Electrochemical activation of glassy carbon, carbon paper and functionalized carbon nanotubes via high-applied-potential cyclic voltammetry leads to the formation of adsorbed, redox active functional groups and increased active surface area. Electrochemically activated carbon electrodes demonstrate enhanced activity toward NADH oxidation, and more importantly, dramatically improved adsorption of bioelectrochemically active azine dyes. Adsorption of methylene green on an electroactivated carbon electrode yields a catalyst layer that is 1.8-fold more active toward NADH oxidation than an electrode prepared using electropolymerized methylene green. Stabilities studies using cyclic voltammetry indicate 70% activity retention after 4000 cycles. This work further facilitates the electrocatalysis of NADH oxidation for bioconversion, biosensor and bioenergy processes.

[1] Collaboration with Rui Li and Robert M. Worden in Chemical Engineering and Materials Science at Michigan State University.

4.2 Introduction

In Chapter 2 and 3, we describe NADH oxidizing electrodes which were fabricated by electropolymerizing azines on functionalized carbon nanotube (*f*CNT)-modified electrodes.[103] In this chapter, we explore novel methods to further facilitate NADH electrocatalysis in order to accelerate the development of bioelectrocatalysis where NADH-dependent dehydrogenases are involved.

Activation is a well-known approach to increase carbon electrode reactivity.[127] The key principle of carbon material activation is to modify its surface chemistry by increasing surface roughness and introducing carbon-oxygen functionalities.[115-127] For example, as early as 1971, Epstein *et al* studied isotropic pyrolytic graphite activated by cyclic voltammetry (CV) and suggested the formation of quinine-hydroquinone groups.[174] Mostly reported carbon activation procedures include laser irradiation,[125,128] high-intensity ultra-sonication,[124] heating[122] and UV-ozone treatment.[133] Electrochemical pretreatment has attracted extensive interest because of its effectiveness in mild operation conditions.[115-121,123,126]

Glassy carbon (GC) is a widely used conventional electrode material due to its high conductivity, hardness and inertness.[129] Laser *et al* proposed the mechanism of carbon-oxygen group formation on GC electrode surface: the chemical adsorption of oxygen under anodic polarization, the oxidation and reduction of existing surface groups and the evolution of oxygen from water.[175] Čėnas *et al* reported quinoidal structure of pretreated GC and demonstrated its

increased catalytic activity for NADH oxidation.[126] Recent reports regarding electrochemical activation of GC involve CV-activated GC for chloranil adsorption,[120] constant potential treated GC for hydroquinone and catechol sensor.[121]

Porous materials such as carbon paper,[130] carbon foam,[159] and carbon nanotubes[75,131-133] introduce intrinsically high surface areas and may also be electrochemically activated.[127,159] Oxidative treatment of carbon nanotubes (CNTs) is a key method for increasing their hydrophilicity.[75,131-133] However, the literature shows inconsistency regarding the effect of electrochemical pretreatment on CNTs.[176,177] For example, Gong *et al* reported electrochemical activation of vertically aligned CNTs at 1.8 V for 3 min in pH 6.5 phosphate buffer electrolyte yields to a reduction of NADH oxidation overpotential by 450 mV.[176] Yet a different study by Musameh *et al* shows no change of NADH electrocatalysis after electrochemically oxidizing CNTs at 1.75 V for 3 min in pH 7,4 phosphate buffer.[177]

This work utilized high-applied-potential cyclic voltammetry to activate GC, carbon paper (CP) and carbon nanotubes (*f*CNT). Electrochemical activation leads to the formation of redox active groups on the electrode surface and increased active surface area. These activated carbon materials allow subsequent adsorption of the electrocatalyst methylene green (MG), forming a novel NADH-oxidizing interface. The activity of MG-*f*CNT toward NADH oxidation

is higher than our previously reported poly(azine)-*f*CNT electrodes,[103] demonstrating an improved facilitation of NADH electrocatalysis.

4.3 Experimental and Analysis

4.3.1 Materials

GC rotating disk electrodes, diameter 3 mm, were made from type 2 GC rods (Alfa Aesar, Ward Hill, MA). Before use, they were sanded with 400, 800, 2,400 and 4,000 grit ultrafine sandpapers (Buehler, IL), polished to a mirror finish with 0.05 μm alumina slurry, and rinsed with distilled water in an ultrasonic bath for 10 minutes to remove any residual alumina. Multiwall CNT, functionalized by carboxylation (*f*CNT, 9.5 nm diameter, 1.5 μm length, and >95% purity) were purchased from Nanocyl (Sambreville, Belgium, catalog number: NC3101). Carbon paper was purchased from Electrochem, Inc, (Woburn, Massachusetts, catalog number: EC TP1 030). NADH, MG, sodium tetraborate and sodium nitrate were obtained from Sigma-Aldrich (St. Louis, MO). N,N-dimethylformamide (DMF) was purchased from Fisher BioReagents (Hampton, NH). Sodium phosphate monobasic and sodium phosphate diabasic were purchased from J.T. Baker (Phillipsburg, NJ). Argon gas was purchased from Airgas (Lansing MI). Unless otherwise stated, all materials were used as received.

4.3.2 CNT coating on GC and CP

As previously reported,[103,178] CNT were dispersed in DMF solvent to create 1 mg mL^{-1} ink under ultrasonication. CNT-coated GC electrodes (CNT-GC) were fabricated by drop-casting

5 µl of CNT ink on the GC surface and vacuum drying. For the purposes of elemental analysis, CNT-coated CP was prepared by air-brushing and dried in vacuum.

4.3.3 Electrochemical activation of carbon electrode

GC and CP were activated by cyclic voltammetry (CV) with scan rate of 100 mV s^{-1} between -1.5 V to 2.5 V vs. Ag|AgCl (4 M KCl) in 100 mM, pH 7.45 phosphate buffer. Twenty cycles were conducted at 30℃. *f*CNT were further activated electrochemically using CV for two cycles, because further cycles would lead *f*CNT to fall off from carbon substrate.

4.3.4 Deposition of azines

Two approaches were used for azine deposition: adsorption and electropolymerization. For adsorption, the activated electrodes were soaked in 1 mM MG solution (100 mM pH 7.45 phosphate buffer, 30℃) for 1 hour. For electropolymerization, CV was performed in MG monomer solution at 50 mV s^{-1} between -0.5 to 1.5 V vs. Ag|AgCl for 20 cycles in 10 mM, pH 9.1 borate buffer with 100 mM $NaNO_3$.[82]

4.3.5 Electrochemical characterization

All electrochemical characterizations were obtained using a VSP potentiostat (Bio-Logic VSP, Knoxville, TN). An Ag|AgCl (4 M KCl) reference electrode was employed with a platinum wire as counter electrode. The supporting electrolyte used was 100 mM phosphate buffer, pH 7.45, 30℃, with argon purged to exclude oxygen.

Capacitance was measured by CV in the range of 0.3 to 0.4 V vs. Ag|AgCl with scan rates varying from 30 to 150 mV s^{-1}. Plotting the current against scan rate, the slope was recorded as the capacitance. Characterization of redox peaks was performed via CV with scan rate 50 mV/s. NADH oxidation activities were characterized by chronoamperometry for polarization curves and NADH concentration studies. In polarization curves, NADH concentration was fixed at 1 mM, and steady-state current density at each working potential was recorded. In NADH concentration studies, working electrode potential was fixed at 50 mV vs. Ag|AgCl, and steady-state current density at each NADH concentration was recorded.

4.3.6 Elemental analysis

Scanning electron microscopy (SEM, JEOL JSM-7500F, 5.0 kV, 4.5 mm) and Energy-dispersive X-ray spectroscopy (EDS) were used for elemental quantification. The details of these techniques have been described in Chapter 2.

4.4 Results and discussion

Glassy carbon RDEs, CP and *f*CNT were electrochemically activated by CV. MG was then deposited on pretreated carbon electrodes, and these electrodes were further characterized for activity towards NADH oxidation.

4.4.1 Electrochemical Activation

Activation of the GC electrode was achieved by CV over -1.5 to 2.5 V in phosphate buffer, the voltammograms of which are shown in Figure 4.1. In the 1.5 to 2.5 V range, the evolution of oxygen from water contributes to a large observed oxidation current. Under such

anodic polarization, oxygen chemisorbs on the GC surface, presumably at defects in the basal plane sites.[175,179,180]

$$C + H_2O \rightarrow C(O) + 2H^+ + 2e^- \quad [4.1]$$

where C(O) represents the possible carbon-oxygen functionalities on electrode surface, such as phenol, carbonyl and quinone.[181]

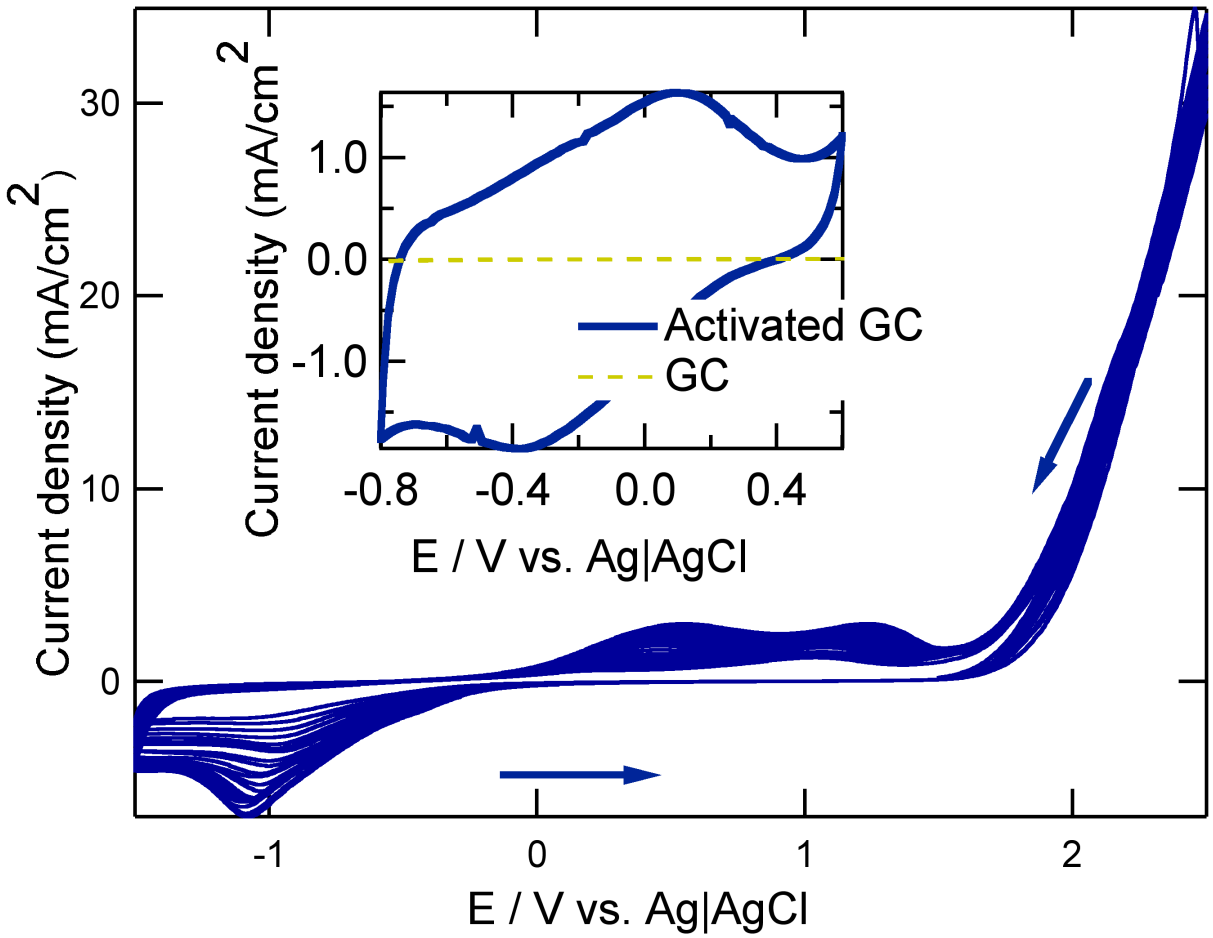

Figure 4.1 Electrochemical activation of glassy carbon electrode. Cyclic voltammetry was performed on glassy carbon electrode, 20 cycles, 100 mV/s, 0.1 M phosphate buffer, pH 7.45, 30 ºC. Insert: Cyclic voltammograms of glassy carbon electrode before and after activation in 0.1 M phosphate buffer pH 7.45, 30 ºC.

After surface carbon is oxidized, electrolyte may penetrate into interlayer spaces, form graphite-oxide layers, thereby increasing the distance between layers, and further provoke the increase of active surface area.[180,182] Moreover, at such high polarization potential, aromatic rings can be oxidatively broken and oxidized to CO or CO_2. This process can facilitate the electrochemical activation and porous structure formation in GC.[180]

At low potential (< 0 V, especially around -1 V), the cathodic current in Figure 4.1 is attributable to water reduction. This region is not necessary for electrochemical activation, and it is possible to bypass this cathodic polarization region altogether. Further analysis of the impact of activation conditions is ongoing.

4.4.2 Electrochemically activated carbon electrodes

CV characterization of the electrochemically activated GC electrode (Act-GC) is displayed in the insert of Figure 4.1. One can observe a significant increase of capacitive current as well as an obvious redox peak with mid-potential around -0.15 V vs. Ag|AgCl. This mid-potential is comparable to the reported redox potentials of quinones,[183] indicating the existence of quinine/hydroquinone couple according to:

$$Q + 2H^+ + 2e^- \rightleftharpoons QH_2 \qquad [4.2]$$

The existence of redox active quinine/hydroquinone couples has been suggested by Epstein *et al*[174] and Čėnas *et al*[126] to account for the observed redox response. Other functional groups, such as phenol and carbonyl, have a higher capacitance than bare GC and can lead to an increase in observed double-layer capacitance.[180,181]

For the purposes of discussion, we refer here to all redox active groups produced by activation as "quinones". Assuming a two-electron redox reaction, quinone loading was determined coulometrically to be 29 nmol cm^{-2} for electroactivated GC. A broad redox peak was

also observed for electroactivated CP, pre-functionalized CNT (*f*CNT) and further electrochemically activated *f*CNT (Act-*f*CNT, CVs not shown). Quinone loadings for all of these materials were calculated from CV.

The morphology of Act-*f*CNT characterized by SEM is displayed in Figure 4.2a. A homogeneous porous structure with 50 to 200 nm pores was found, which is very similar to *f*CNT, indicating that electrochemically activation does not change the porous structure of *f*CNT. For all CP samples, with and without *f*CNT, oxygen content was obtained by EDS, shown in Figure 4.2b. The results were correlated with coulometric quinone loading in Figure 4.2c, where a linear correlation was found. The slope of the line represents the percent of quinone in oxygen functionalities.

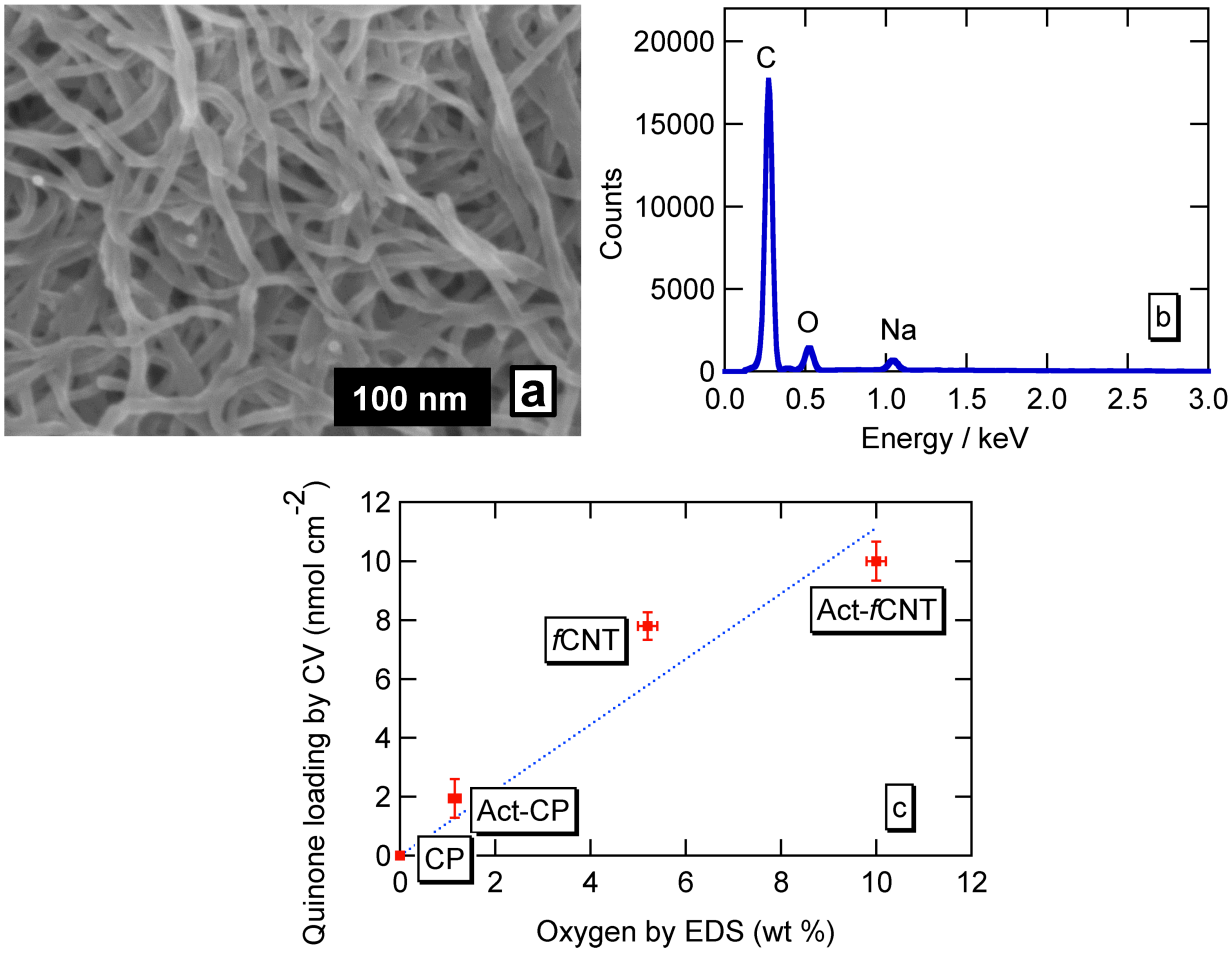

Figure 4.2 a) SEM image of Act-*f*CNT; b) Example of EDS spectra: on Act-*f*CNT; c) Quantitative properties of electrochemically activated carbon material. Quinone loading was calculated by integration of redox peaks in CV in 0.1 M phosphate buffer pH 7.45, 30 ºC, assuming a two-electron redox reaction; Oxygen mass content was obtained from EDS.

Capacitance data are displayed in Figure 4.3 for a range of materials. Act-GC possesses capacitance as high as 2.4×10^{3} µF cm^{-2}, 200-fold above untreated GC and in the same magnitude as *f*CNT, suggesting a significant increase in surface area and/or capacitive species. Electrochemical activation of CP increases its capacitance to 1.4×10^{3} µF cm^{-2} and quinone loading to 1.9 nmol cm^{-2}. Both values are smaller than Act-GC, indicating that the electrochemical activation procedure works better for GC than CP. Electroactivation of *f*CNT

increases capacitance by 7% and quinone loading by 28%. This small increase is likely due to extensive surface oxidation during functionalization, such that there is little potential for further increase. Further optimization of *f*CNT electrochemical activation is under study, but so far, Act-*f*CNT is still the most active carbon material in most respects.

The catalytic activity of the electroactivated electrodes toward NADH oxidation was studied via polarization and concentration studies. Figure 4.4 shows the polarization curves in fixed NADH concentration (1 mM) and the NADH concentration profiles under fixed applied potential (50 mV vs. Ag|AgCl). Activity toward NADH electrocatalytic oxidation was consistently enhanced by electrochemical activation. This finding is also consistent with literature reported by Čėnas *et al*[126] and Prasad *et al*[184]. But their current is in μA region and the percentage of increase is far lower than this study.[126,184] In the work, current density of 0.35 mA cm^{-2} was observed for Act-GC towards NADH oxidation at 50 mV vs. Ag|AgCl in 20 mM NADH solution (pH 7.45), which is in the same magnitude of 0.21 mg cm^{-2} *f*CNT electrode and at least 200-fold increase compared to untreated GC (Data of bare-GC not shown). Electrochemically activated *f*CNT shows 10% increase in NADH electrocatalysis activity (Data of *f*CNT not shown), consistent with the low increase of capacitance and quinone loading.

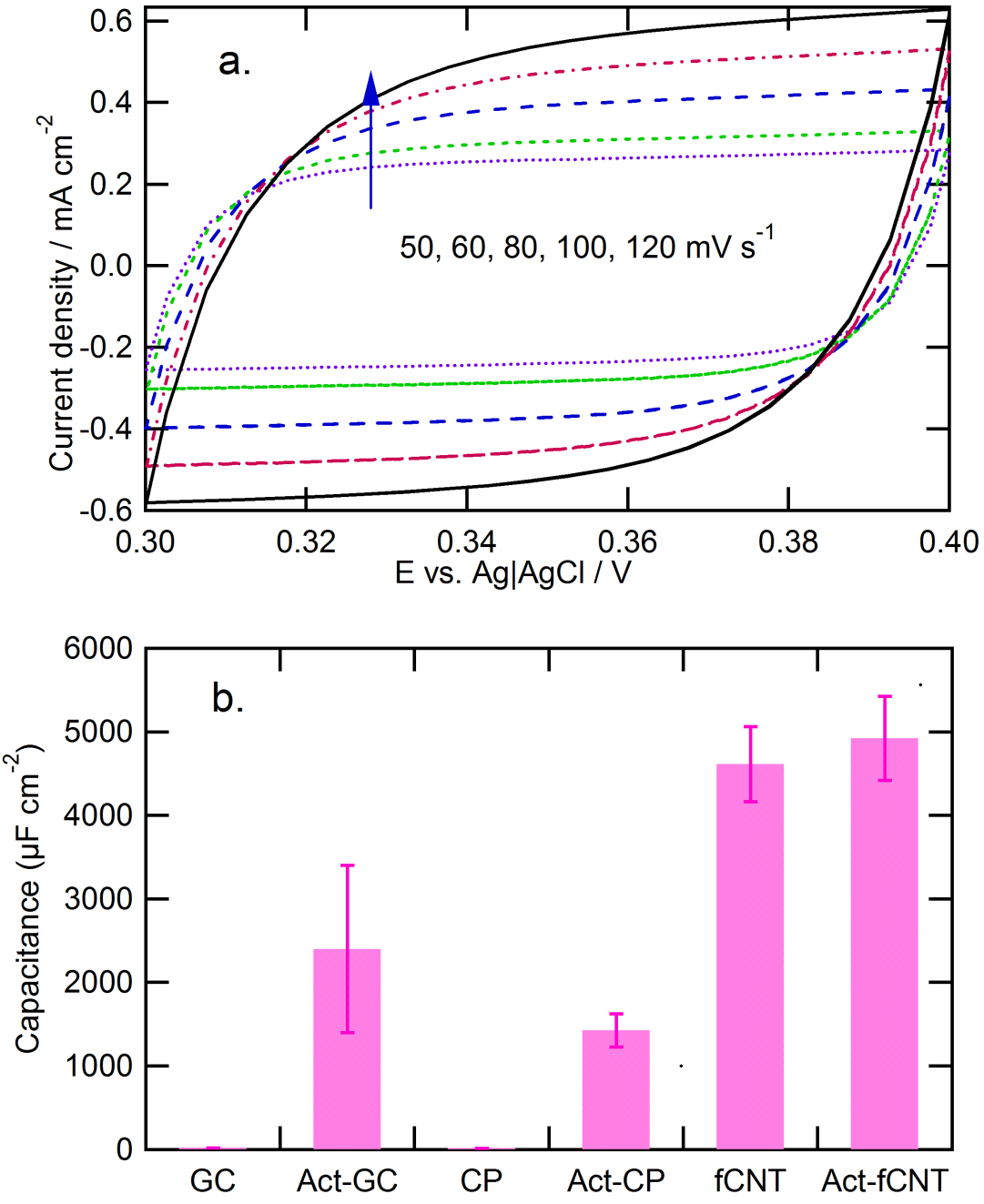

Figure 4.3 a) Capacitance measurement of *f*CNT. Capacitance was estimated using CV in the narrow potential range from 0.3 to 0.4 V vs. Ag|AgCl (4 M KCl) with varying scan rates from 50 to 120 mV s^{-1} in 0.1 M phosphate pH 7.4, 30℃; b) Capacitance of different carbon materials. Plotting the current in the non-faradic potential region against scan rate, the slope was recorded as capacitance.

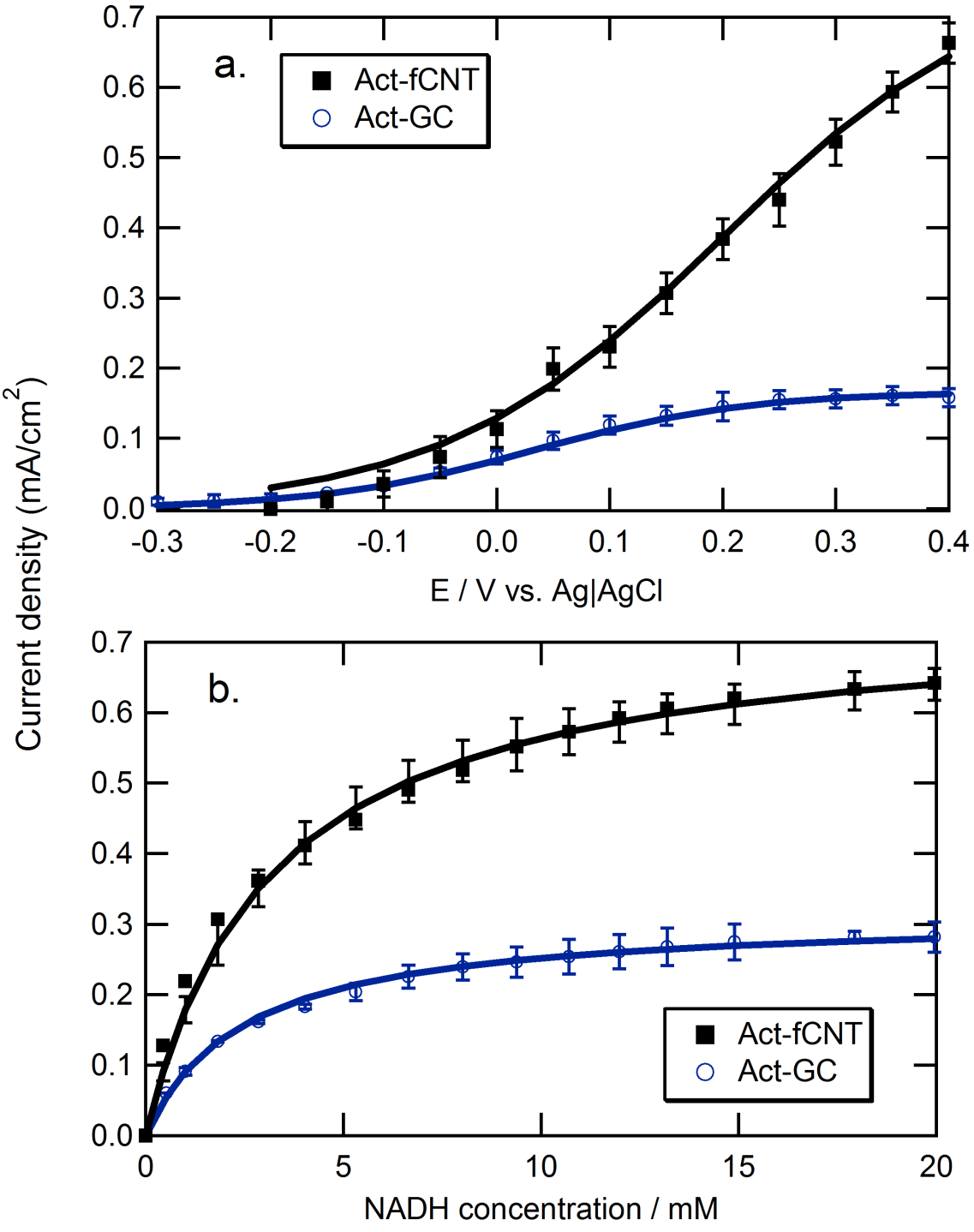

Figure 4.4 Activity of electrochemically activated GC and *f*CNT for NADH electrocatalysis in 0.1 M phosphate buffer pH 7.45, 30 ºC. a) Polarization curve in 1 mM NADH; b) NADH concentration study at 50 mV vs. Ag|AgCl

The enhanced activity toward NADH oxidation may be attributed to increased active surface area, the evidence of which is shown in the increase of capacitance, or to NADH electrocatalysis by surface quinone groups (Q):[185,186]

$$Q + H^+ + NADH \rightleftharpoons QH_2 + NAD^+ \quad [4.3]$$

Followed by the recycling of quinone groups on the carbon electrode surface:

$$QH_2 \rightleftharpoons Q + 2H^+ + 2e^- \quad [4.4]$$

Whereas increased surface area would increase NADH direct oxidation rate, it would not be expected to reduce oxidation overpotential, as quantified by the half-wave potential. However, the introduction of new surface species, such as quinones, can reduce the activation energy, resulting in a reduction in overpotential for NADH oxidation, as shown in comparison of Table 4.1 with Figure 1.3. The half-wave potentials shown in Table 4.1 have taken into account mass transport correction (see section 2.1 for details of mass-transport correction analysis). Considering the half-wave potentials in NADH polarization curve (Table 4.1 and Figure 4.4a) as well as the proportion of redox active group and capacitance of these carbon electrodes, we think that the key reason for the activity of Act-GC is the quinone group, while either *f*CNT or Act-*f*CNT serves more as the high surface area material.

Table 4.1 Half-wave potential in NADH polarization curves

Electrodes	Half-wave Potential (U, mV vs. RHE)
Act-GC	684 ± 8
*f*CNT	827 ± 27
Act-*f*CNT	824 ± 25
PMG-*f*CNT	747 ± 23
MG-*f*CNT	681 ± 41

4.4.3 Azine deposited on activated carbon electrodes

Deposition of MG on activated GC electrode (Act-GC), CP (Act-CP) and *f*CNT (Act-*f*CNT) were achieved by direct adsorption and the performance of these electrodes was compared to performance of electrodes prepared by the electropolymerization method.

Cyclic voltammograms of the resulting MG-Act-GC electrodes are shown in Figure 4.5a, in which two sets of redox peaks can be observed: the two-step, two-electron redox reaction of MG (at potential -0.5 / -0.2 V, -0.25 / 0 V) and the redox behavior of quinone group (at potential -0.3 / 0.1 V). The MG redox peak response for MG-Act-GC is 140-fold higher than MG-GC, indicating a much stronger adsorption on Act-GC. This could be attributable to the stronger electrostatic force between MG and Act-GC, because the oxygen-functionalities on Act-GC make the electrode surface negatively charged, while MG as a basic dye (pK_a =9.9) is positively charged in pH 7.4 solution.[187] Other azine dyes were immobilized on Act-GC, including methylene blue (MB) and toluidine blue O (TBO) and found that the most basic dye MG shows

the strongest adsorption, as shown in Table 4.2, further indicating that electrostatic forces lead to immobilization of azine dyes on Act-GC. Moreover, since TBO is a neutral dye and can also be adsorbed on Act-GC, we believe there also exists other force. Considering that the chemical bonding of GC is composed mainly of sp^2 bonds,[188] as well as the chemical structure of these dyes,[82] this adsorption force is probably π-π stacking.[189,190]

Table 4.2 Azine adsorption on Act-GC

Dye	pK_a[187]	Electroactive loading (nmol/cm^2)
Methylene Green	9.9	40
Methylene Blue	9.3	29
Toluidine Blue O	6.1	34

In our previous work, we fabricated high-rate nanostructured NADH oxidizing electrodes by electropolymerizing MG on functionalized *f*CNT (PMG-*f*CNT).[103] In this study, we found that the MG immobilization on *f*CNT can be achieved by facile adsorption. The resulting electrodes demonstrate improved electro-activity compared to PMG-*f*CNT. The redox behavior of the obtained MG-*f*CNT was characterized via CV, and was compared to that of PMG-*f*CNT, as shown in Figure 4.5b. The peaks in -0.5 to 0.2 V vs. Ag|AgCl represent the two-step redox reactions of electro-active MG and PMG. PMG redox peaks shift to a slightly positive region, consistent with findings on low-surface area electrodes.[82] Integration of the peaks yields electroactive loading of 63 nmol cm^{-2} for MG-*f*CNT and 38 nmol cm^{-2} for PMG-*f*CNT. This

result indicates that MG-*f*CNT possesses more active loading than the previous reported PMG-*f*CNT.

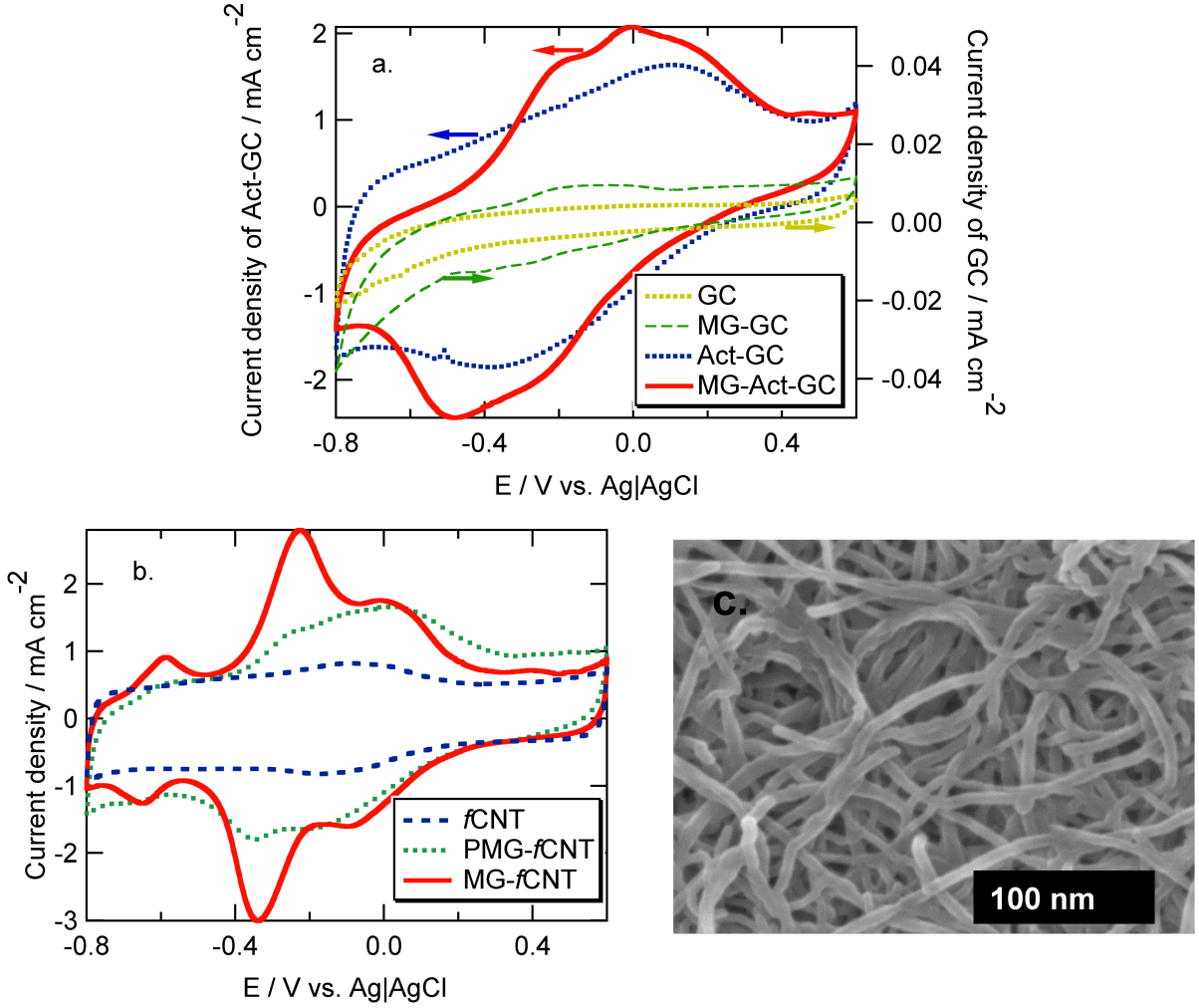

Figure 4.5 Cyclic voltammograms in 0.1 M phosphate buffer pH 7.45, 30 ºC. a) Adsorbed MG on electrochemically activated GC electrode, compared with activated GC and untreated GC; b) Adsorbed MG on pre-functionalized CNT, compared with electropolymerization on *f*CNT; c) SEM image of MG-*f*CNT

In Figure 4.5b, it is difficult to discern the broad quinine/hydroquinone peaks on MG-*f*CNT, since they overlap with MG peaks. The redox peak observed with midpoint potential -0.6 V vs. Ag|AgCl may be due to the impurity in MG, such as methylene blue (MB).[82] MB has very

similar chemical structure to MG and also possesses catalytic activity towards NADH oxidation. But its activity is generally lower than MG, as reported by previous researchers.[14,78,191] Thus we do not believe the presence of MB explains electrode activity.

The morphology and EDS analysis of the MG-*f*CNT electrode is shown in Figure 4.5c. From SEM images, no distinct clusters can be observed, suggesting a conformal deposition, which allows good interaction between MG and *f*CNT.

The activity of MG-*f*CNT towards NADH electrocatalysis was characterized and shown in Figure 4.6 and Table 4.1, compared to previously reported PMG-*f*CNT-GC. The MG-*f*CNT-GC electrode demonstrates lower half-wave potential and higher current density for NADH electrocatalysis, which is corresponding to their CV comparison, indicating that MG-*f*CNT is a better-activity NADH oxidizing interface.

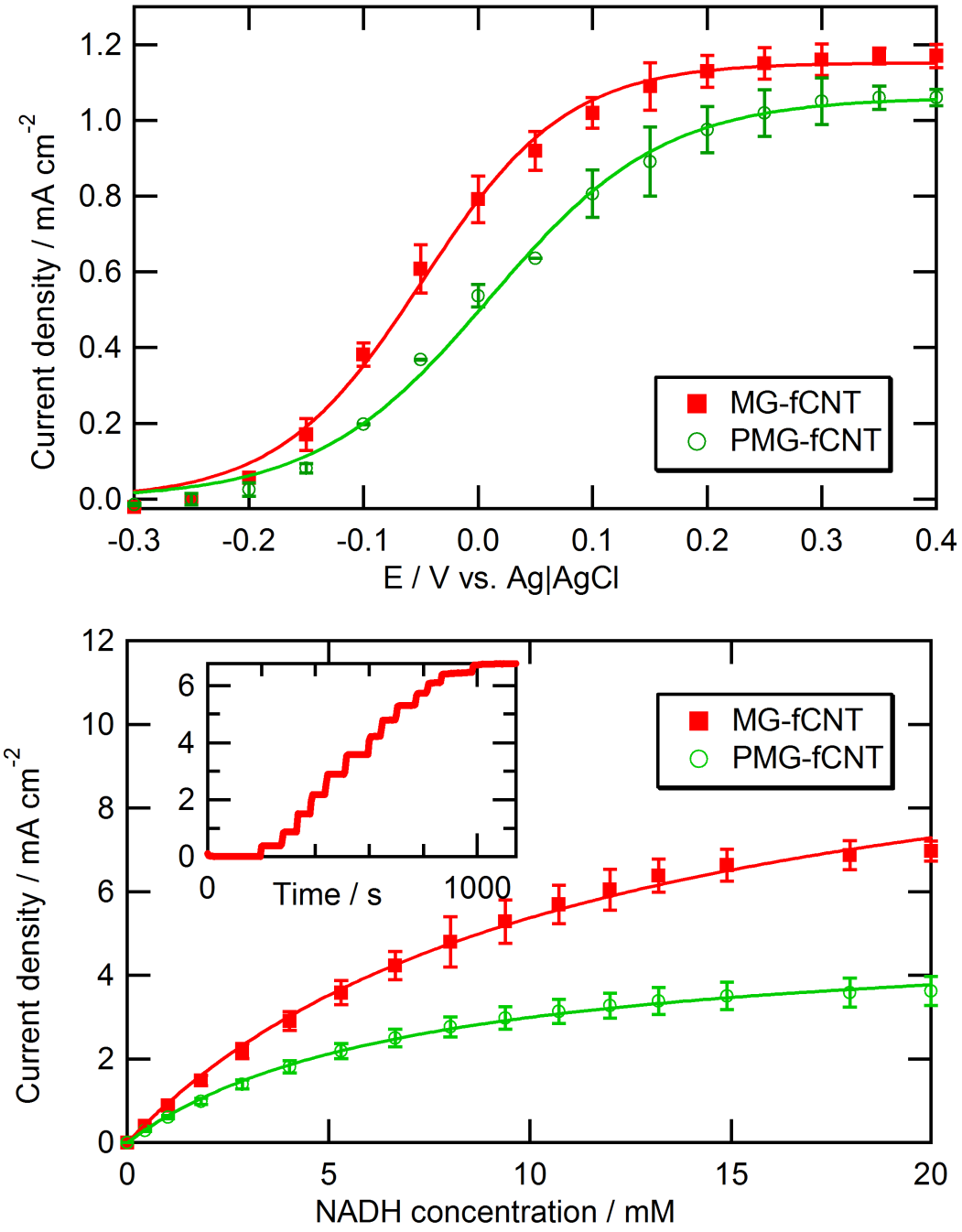

Figure 4.6 NADH electrocatalysis activity of MG-*f*CNT and PMG-*f*CNT in 0.1 M phosphate buffer pH 7.45, 30 ºC. a) Polarization curve in 1 mM NADH; b) NADH concentration study at 50 mV vs. Ag|AgCl, Insert: Time-dependent curve on MG-*f*CNT

4.4.4 Absorption vs. Electropolymerization

As discussed above, the mechanism of adsorption involves electrostatic force, Van Der Waals force and π-π stacking. The processes of electropolymerization include adsorption of MG, oxidation and reduction of MG, and irreversible oxidation of MG to PMG that involves the formation of cation-radical.[82,103,192] The chemical structure and mechanism of formation of PMG is still under study. It is believed that PMG has the same redox center as MG (as shown in Figure 4.7a).[66,82] Hypotheses on PMG formation include "ring-to-ring" coupling which is analogous to the formation of N,N,N,N-tetramethylbenzidine by oxidation of N,N-dimethylaniline,[82] and "nitrogen-to-ring" coupling, arising from the observation that destruction of methylene green monomer leads to the demethylation of amino group.[84] Both "ring-to-ring" and "nitrogen-to-ring" types were confirmed via electrospray mass spectrometry as reported by Vilmos *et al*.[84] The "nitrogen-to-ring" coupling was further confirmed from XPS characterization as reported by Rincon *et al*.[66] Based on these observations, the general proposed chemical structure of PMG is purposed in Figure 4.7b.[66,84,110] Because the coupling sites are far away from the active center of methylene green, the polymerization process is not expected to consume or eliminate redox active sites.

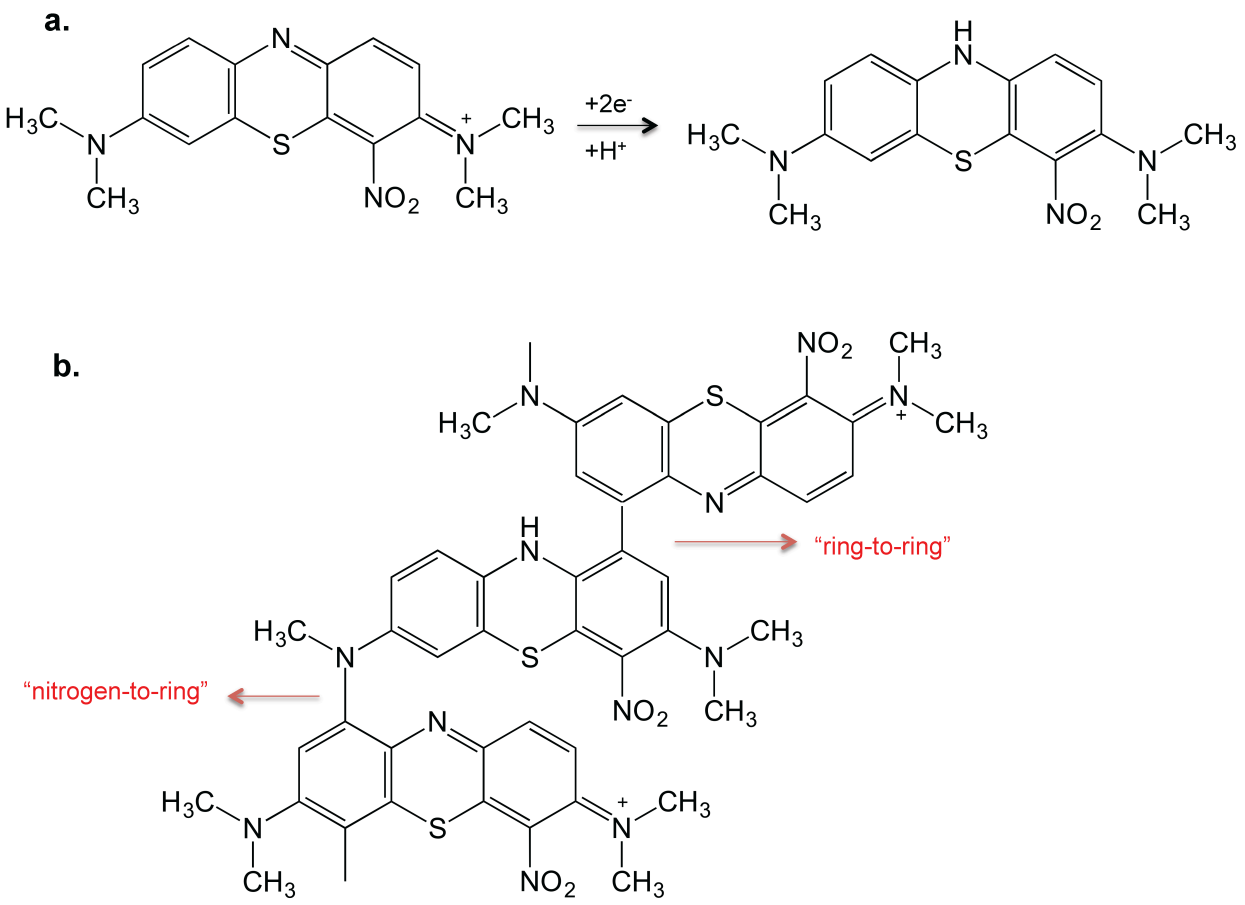

Figure 4.7 a) Redox reaction of methylene green; b) Possible structure of poly(methylene green)

For untreated GC, without the introduction of carbon-oxygen functional groups, the adsorption of MG on GC is relatively weak, and electropolymerization yields a higher electrocatalyst loading and better NADH oxidation activity than MG (as shown in Figure 4.8). Electropolymerization was also used to immobilize PMG on Act-GC. The electropolymerized electrode showed lower electro-active species loading than Act-GC and MG-Act-GC, as shown in Figure 4.7. Only PMG peaks were found and quinone peaks were not observed. PMG-Act-GC also possessed poorer activity towards NADH electrocatalysis than Act-GC and MG-Act-GC, consistent with their relative redox active group loading. It is possible that the irreversible oxidation of MG to PMG during polymerization deactivated some carbon-oxygen functional

groups, including quinones, that were introduced in electrochemical activation. This leads to lower electroactive loading on PMG-Act-GC thus lower activity for NADH oxidation.

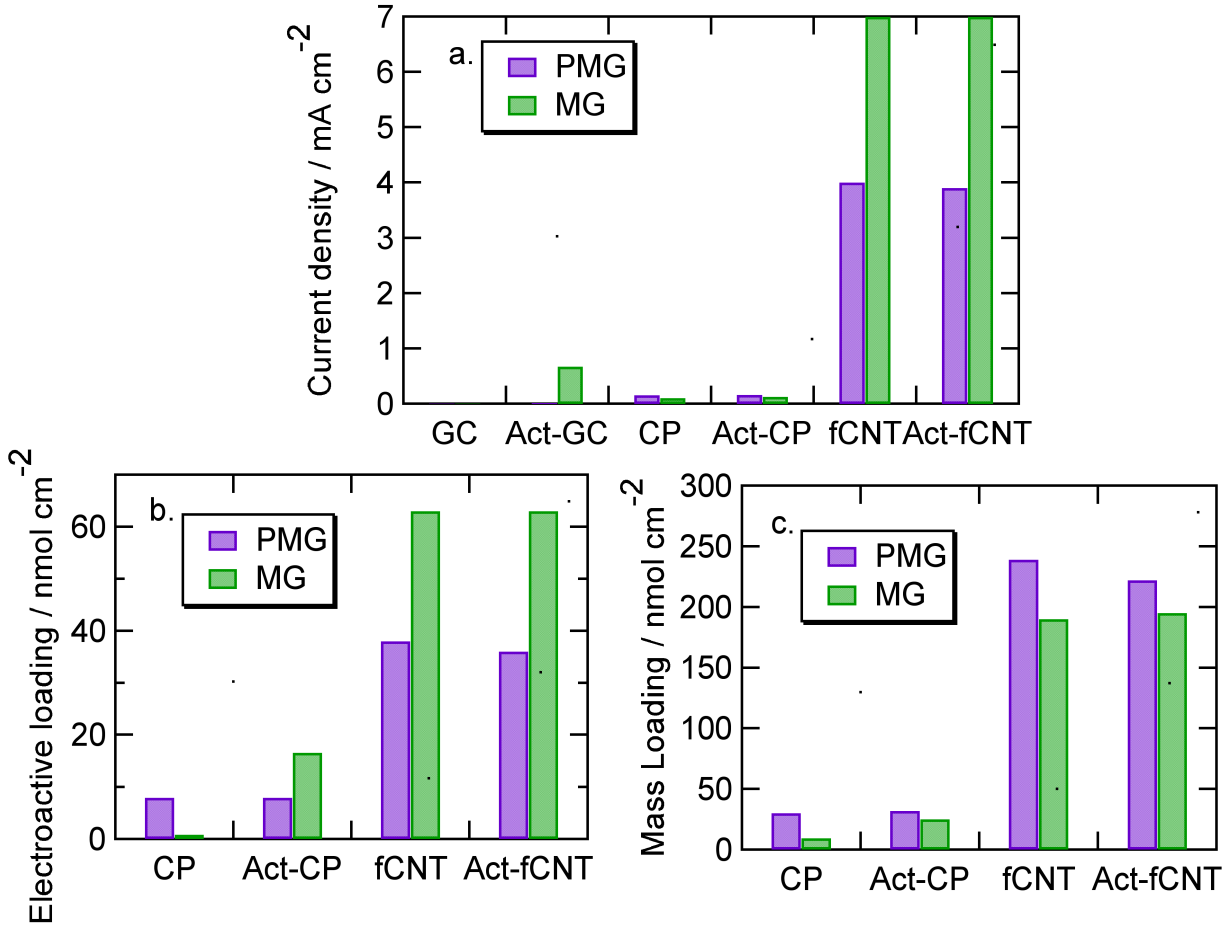

Figure 4.8 a) NADH electrocatalysis current was recorded at 50 mV vs. Ag|AgCl in 20 mM NADH solution, 0.1 M phosphate buffer pH 7.45, 30 ºC; b) Electroactive loading was calculated by integration of redox peaks in CV in 0.1 M phosphate buffer pH 7.45, 30 ºC, assuming a two-electron redox reaction; c) Mass loading was obtained by EDS based on sulfur content.

The quantitative comparison of MG and PMG in terms of NADH oxidation activity and electrocatalyst loading is displayed in Figure 4.8. MG-Act-GC electrode demonstrates 0.7 mA cm^{-2} current density for NADH electrooxidation at 50 mV vs. Ag|AgCl in 20 mM NADH solution (Figure 4.8a), a two-fold increase compared to Act-GC. Considering the two sets of

redox peaks observed in cyclic voltammograms (Figure 4.5a), electrooxidation of NADH on MG-Act-GC is likely to be catalyzed by both the quinone group and MG. After electrochemical activation of *f*CNT, immobilization of MG, either by adsorption (MG) or polymerization (PMG), as well as the resulting catalytic activity remains approximately constant. This could be attributable to a small increase of quinone loading and/or surface area due to *f*CNT electrochemical activation. These results may be improved upon by optimization of *f*CNT electrochemical activation conditions.

Electroactive and mass loading of electrocatalyst are compared for MG and PMG in Figure 4.8b and 4.8c. MG shows higher electroactive loading and lower mass loading than PMG on functionalized carbon materials, suggesting that adsorption provides more efficient utilization of immobilized species than electropolymerization. Taking into account the finding that MG demonstrates higher electrocatalytic activity towards NADH oxidation, one could hypothesize that adsorption is a more effective deposition approach than electropolymerization for carbon material with functional groups.

4.4.5 Stability

The stability of the modified electrodes was measured by CV between -0.8 and 0.6 vs. Ag|AgCl at 900 rpm in pH 7.45 phosphate buffer. MG-Act-GC shows only 1% decrease in electroactive loading after 100 cycles, comparable with literature data on PMG-GC (data not shown).[71] Electroactive loadings for MG-*f*CNT and PMG-*f*CNT were obtained by integration of redox peaks in CV, assuming a two-electron redox reaction. As shown in Figure 4.9, the electroactive loading of MG-*f*CNT tends to decrease faster than PMG-*f*CNT under CV condition.

Nevertheless, MG-*f*CNT still shows higher loading than PMG-*f*CNT after 4000 continuous cycles, corresponding to its higher initial activity towards NADH oxidation, as shown in Table 4.3.

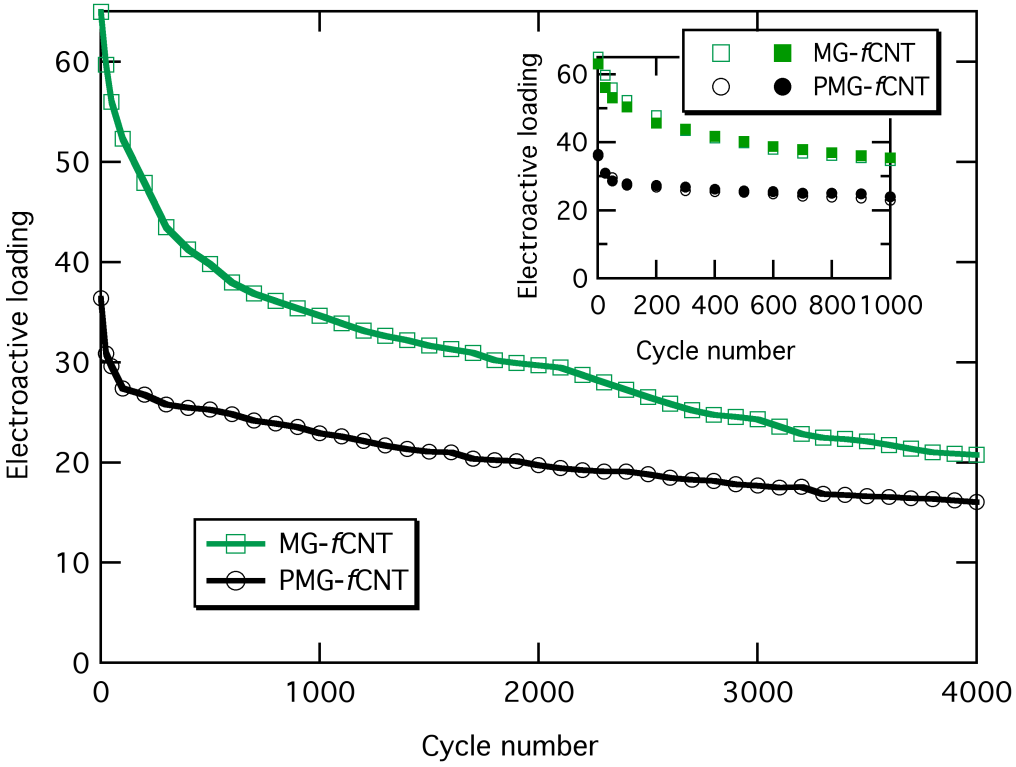

Figure 4.9 Stability of modified electrodes as measured by cyclic voltammetry, 0.1 M phosphate buffer pH 7.45, 30 ºC. Electroactive loading was obtained by integration of redox peak, assuming a two-electron redox reaction.

Table 4.3 Stability data

Electrodes	Initial activity (mA/cm^2)	After 4000 cycles (mA/cm^2)	Activity Reminds
MG-ACT-GC	0.70 ± 0.04	0.48	69%
MG-*f*CNT	7.0 ± 0.2	4.9	70%
PMG-*f*CNT	3.8 ± 0.2	3.1	81%

4.5 Conclusion

Electrochemical activation leads to oxidation of carbon, forming carbon-oxygen functionalities. Some of the functional groups are found to be traces of quinone due to their redox active property and electrocatalytic ability towards NADH oxidation. Other functional groups could lead to an increase of electrochemical capacitance. The electrochemically activated carbon electrode possesses good catalytic activity towards NADH oxidation. Adsorption of MG on activated carbon electrodes yields a highly active interface for electrooxidation of NADH, which in turn enables improved electrochemical regeneration of enzyme cofactors.

5 Modeling of bioelectrocatalysis for dihydroxyacetone (DHA) production involving enzyme cofactor electrochemical regeneration

5.1 Abstract

Quantitative models were developed for dihydroxyacetone (DHA) production from glycerol oxidation coupled with electrocatalysis. A two-step kinetic model was developed to describe the reactions in bioelectrocatalysis involving electrochemical NADH regeneration. Planar and porous bioelectronic interfaces are modeled to simulate, predict and evaluate kinetics and diffusion in the bioconversion. Key parameters involve diffusivity of cofactor/substrate, electrocatalytic activity and enzyme kinetics. Model-based analysis indicates that the bioreactor is controlled by glycerol dehydrogenase kinetics for enzyme loadings lower than 1 mM and shifts to mass transport and incipient NADH oxidation kinetic control at higher enzyme loadings.

5.2 Introduction

Utilization of glycerol as a source material has attracted attention due to the increasing amount of glycerol produced from biodiesel industry (>22 million lbs per year) and its decreasing price (<$1/lb).[193] The most important oxidation product from glycerol is dihydroxyacetone (DHA). DHA is a high-value chemical (~$240/lb) that is the active ingredient in sunless tanning agent in cosmetics industry and also widely used as a chemical intermediate in the pharmaceuticals and food industries.[12,193,194] The current commercial approach for DHA production from glycerol is fermentation using *Gluconobacter oxidans,* with yields of 87-94% after ~32 h.[194,195] A chemical approach based on precious metal (Au or Pt) catalysts have been studied, where a shorter reaction time is needed (<~10 hr) and the selectivity is relatively low.[194] To achieve effective conversion from glycerol to DHA, glycerol dehydrogenase (GlyDH)-based bioelectrocatalysis is a promising approach. As shown in Figure 5.1, the kinetics of the system can be simplified into two steps: the electrocatalytic regeneration of cofactor $NADH/NAD^+$ and the enzymatic conversion of substrate using glycerol dehydrogenase. As shown in Figure 5.1, for dihydroxyacetone production, a glycerol substrate is oxidized to DHA in the presence of GlyDH and cofactor NAD^+, whereas NAD^+ is regenerated by NADH electrocatalytic oxidation, forming a cofactor regeneration cycle:

$$\text{Glycerol} + NAD^+ \xleftarrow{\text{Glycerol}} \text{DHA} + NADH + H^+ \qquad [5.1]$$

$$\mathrm{NADH} \xrightarrow{Electrocatalyst} \mathrm{NAD^+ + H^+ + 2}e^- \qquad [5.2]$$

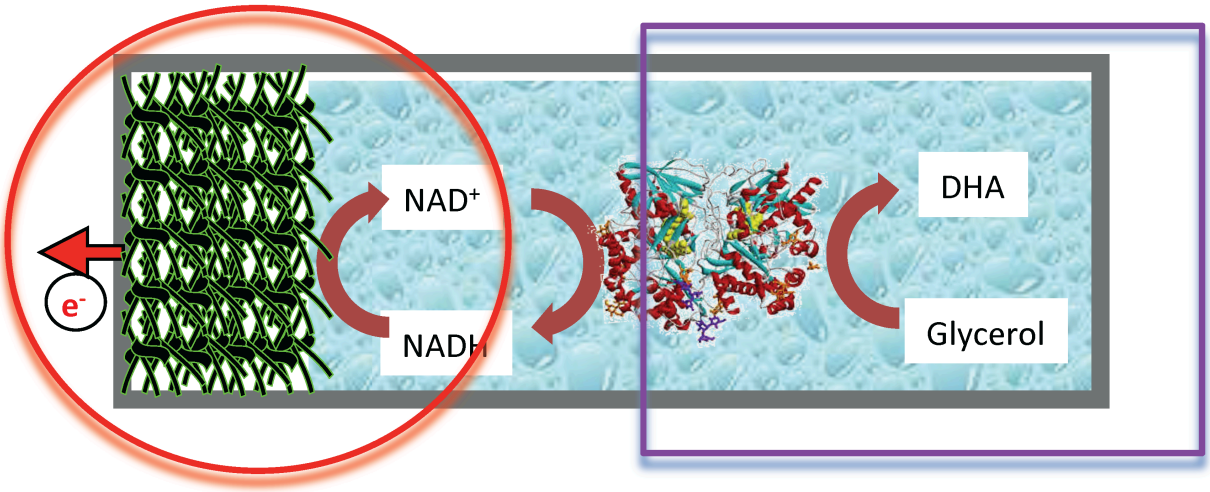

Figure 5.1 Scheme of bioelectrocatalysis showing two-step kinetics

Because of high cost, it is undesirable to feed enzymes or cofactors into a conversion process.[54] Instead, it is preferable to immobilize these active species on the electrode surface.[61] Typical approaches to molecular immobilization include intermolecular linking by means of bifunctional or multifunction reagents, and entrapment into a polymer matrix or a semi-permeable membrane, such as Nafion.[31,32,54,61,62] The Worden Lab has developed intermolecular linking techniques that use bifunctional or multifunction reagents. They have reported cysteine as a heterotrifunctional linking molecule which is attached to the electrode by sulfhydryl groups, to the electrode mediator by carboxyl group and to the cofactor by amino group.[32]

Mass transport introduces additional complexity, especially for enzyme/cofactor immobilized system. Bartlett *et al* built a model involving diffusion and kinetics in an immobilized mediated enzyme electrode.[140] Analytical solutions are generally based on the determination of suitable limiting cases where the diffusion and kinetics can be linearized and solved.[138,139,196,197] Based on Bartlett *et al*'s model, Manimozhi *et al* reported the analytical solutions for non-Michaelis-Menten kinetics of the enzymatic reaction.[141] Based on these models, we developed a mathematical model for our bioelectrocatalysis system on planar interface. Barton developed a model of a porous carbon electrode based on redox hydrogels, where the morphological properties of the carbon support such as porosity, fiber diameter, and surface area were studied.[143] Meena *et al* studied the non-linear reaction diffusion equations for direct reaction of substrate at microdisc electrode surface.[142] Kar *et al* described a modeling study of bioanode in methanol/air fuel cell where enzymes and electrocatalyst are entrapped in a porous film whereas cofactor NAD^+ is present in the bulk solution.[137] Built upon this model, models accounting for porous structure of high-rate electrodes are considered for systems where the electrocatalyst, cofactor and enzyme are immobilized within the void volume of the porous electrode.

In this chapter, we present a bioelectronic interface model that includes the reversible kinetics exhibited by dehydrogenases, as well as quantitative electrocatalyst kinetics. Nondimensional Damkohler numbers provide a useful approach to simulate, predict and evaluate

the kinetics and diffusion in the bioelectrocatalytic system. The resulting model, if validated, can be used to design and optimize electrochemical bioreactors and biofuel cells.

5.3 Model development

One kinetic model and three kinetic-mass transport models were developed to describe the fundamental processes in the bioreactor.

5.3.1 Kinetic model

As described in Eq 5.1 and Eq 5.2, the kinetics of bioelectrocatalysis can be simplified into two steps: enzymatic reaction and electrocatalysis. Degradation of NADH is not considered in this chapter, because the decay rate is only 0.2% of the initial reaction rate. Our collaborators in the Vieille lab have determined that GlyDH reversibly oxidizes glycerol to DHA in the presence of NAD^+. However, the exact kinetics are still under study. It is not yet clear whether the enzymatic reaction follows ordered bi bi or random bi bi kinetics,[198] but preliminary data indicate a good fit to ordered bi bi kinetics. In the present work, ordered bi bi kinetics are applied, but could be replaced by random bi bi after the kinetics are fully studied.[198] According to reversible ordered bi bi kinetics, rate of the enzyme reaction can be expressed as:[199]

$$R_{enzyme} = \frac{k_f k_r [E]([A][B] - \frac{[P][Q]}{K_{eq}})}{k_r K_{ia} K_{mB} + k_r K_{mB}[A] + k_r K_{mA}[B] + \frac{k_f K_{mQ}[P]}{K_{eq}} + \frac{k_f K_{mP}[Q]}{K_{eq}} + k_r[A][B] + \ldots} \\ + \frac{k_f K_{mQ}[A][P]}{K_{eq} K_{ia}} + \frac{k_f [P][Q]}{K_{eq}} + \frac{k_r K_{mA}[B][Q]}{K_{iq}} + \frac{k_r [A][B][P]}{K_{ip}} + \frac{k_f [B][P][Q]}{K_{ib} K_{eq}} \quad [5.3]$$

where E denotes enzyme, A is NAD^+, B is glycerol, P is DHA, Q is NADH. K_{mA}, K_{mB}, K_{mP} and K_{mQ} are Michaelis-Menten constants, and K_{ia}, K_{ib}, K_{ip} and K_{iq} are enzyme dissociation constants. k_f and k_r are the turnover numbers for forward reaction and backward reaction, respectively. K_{eq} is the equilibrium constant, defined as:

$$K_{eq} = \frac{[DHA][NADH]}{[Glycerol][NAD^+]} = \frac{k_f K_{iq} K_{mP}}{k_r K_{ia} K_{mB}} \quad [5.4]$$

In total, this kinetic model requires the experimental determination of 10 parameters for a complete description.

The electrode reaction rate is related to electrode current and depends on NADH concentration, applied potential and electrode surface-volume ratio:[103]

$$R_{electro} = i \times \frac{S}{nF} = \frac{j_{\max} S}{nFV_r} \left(\frac{[NADH]}{K_S + [NADH]} \right) \left\{ \frac{\exp[(U-V)/b]}{1 + \exp[(U-V)/b]} \right\} \quad [5.5]$$

where [NADH], *K*s, k_1, *V*, *U* and *b* have the same meanings as in Chapter 2. S/V_r is the surface/volume ratio of the conducting phase and *F* is the Faraday constant.

The overall rate of biochemical conversion can be expressed as function of the two reaction rates:

$$\frac{d[NAD^+]}{dt} = -\frac{d[NADH]}{dt} = R_{electro} - R_{enzyme} \quad [5.6]$$

$$\frac{d[Glycerol]}{dt} = -\frac{d[DHA]}{dt} = R_{enzyme} \quad [5.7]$$

5.3.2 Kinetics-mass transport model

To study the mass transport in the bioelectronic conversion, we developed three models to represent different immobilization and boundary conditions for the nanostructured bioelectronic interface, the schemes of which are shown in Figure 5.2.

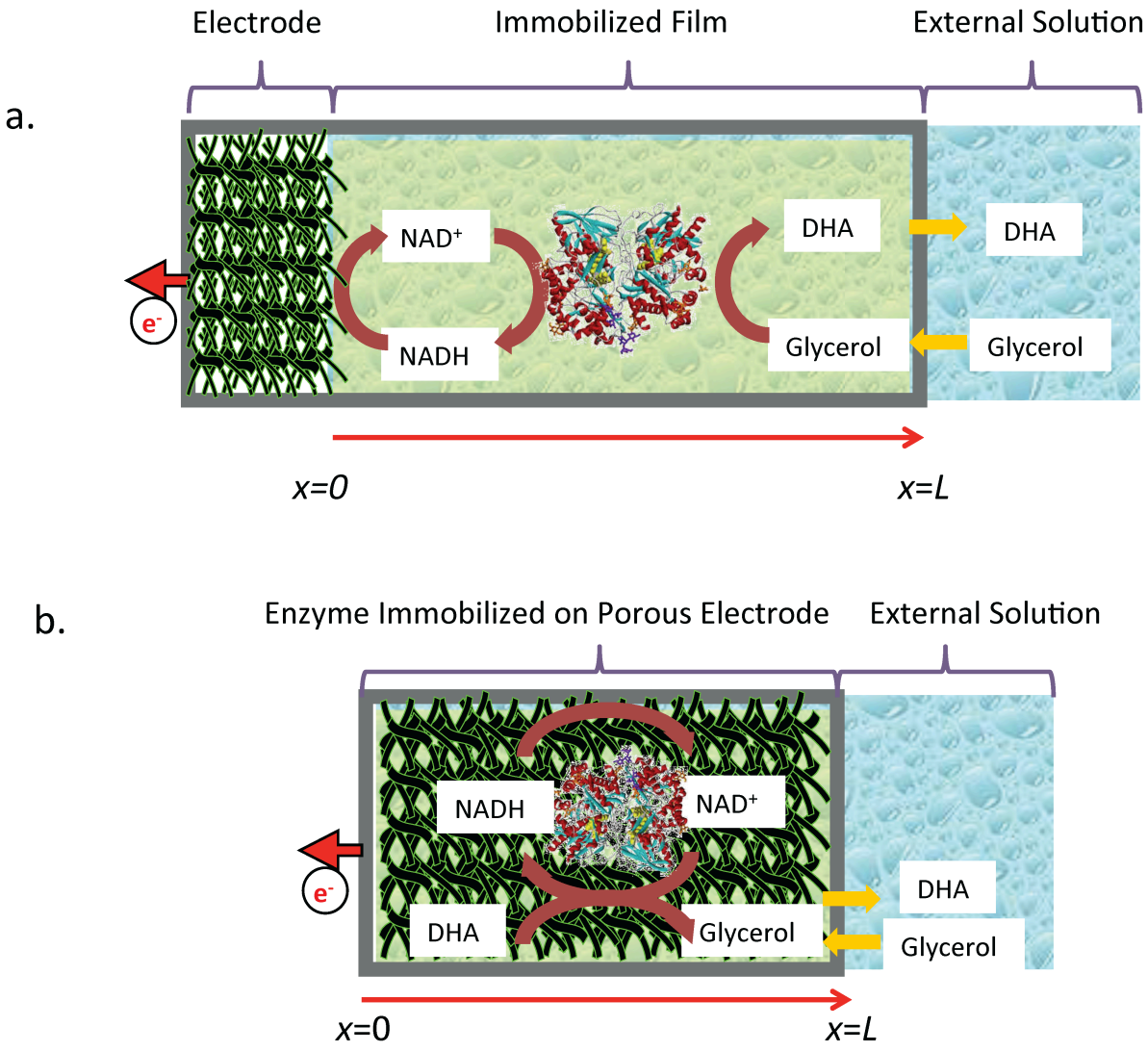

Figure 5.2 Scheme of kinetics-mass transport model. a): Planar interface; b): Porous interface

The comparison of the three models is listed in Table 5.1. The interface structure may be planar (Figure 5.2a), where both cofactor and enzyme are assumed to be entrapped on top of electrocatalyst and throughout the thickness *L* of the film (e.g. Nafion). Cofactor is assumed to be able to diffuse in the film, whereas enzyme has uniform concentration. Or the interface

structure may be porous (Figure 5.2b), where cofactor, immobilized electrocatalyst and enzyme exist in the porous electrode film. In the case of the porous structure (Figure 5.2b) the cofactor may be either free to diffuse into and within the porous layer (porous-mobile model) or may be entrapped within the porous layer (porous-entrapped model). In all three models, the external solution (electrolyte) is assumed to be well-mixed. The substrate glycerol partitions from the electrolyte into the film, whereas the product partitions from the film to the electrolyte. The substrate and product are free to diffuse through the film. At each location in the film, the total of NADH and NAD^+ concentration is assumed to equal to NAD^+ initial loading, whereas the total of glycerol and DHA concentration is assumed to equal to glycerol bulk concentration. In these models, again, we have neglected the decomposition reaction of NADH.

Table 5.1 Comparison of three kinetics-transport models for bioelectronic interface

Model		**Planar**	**Porous-Mobile**	**Porous-Entrapped**
Interface Structure		Planar	Porous	
Cofactor		Entrapped	Mobile	Entrapped
Boundary Conditions	***x*=0**	$\frac{d[Glycerol]}{dx}=0$		
		$\frac{d[DHA]}{dx}=0$		
		$\frac{d[NAD^+]}{dx}=\frac{i}{nFD_{Nh}}$	$\frac{d[NAD^+]}{dx}=0$	
		$\frac{d[NADH]}{dx}=\frac{i}{nFD_{Nh}}$	$\frac{d[NADH]}{dx}=0$	
	x*=*L	$[Glycerol]=[Glycerol]_\infty$		
		$[DHA]=0$		
		$\frac{d[NAD^+]}{dx}=0$	$[NAD^+]=[NAD^+]_\infty$	$\frac{d[NAD^+]}{dx}=0$
		$\frac{d[NADH]}{dx}=0$	$[NADH]=0$	$\frac{d[NADH]}{dx}=0$

5.3.2.1 Planar model description

The planar interface model is shown in Figure 5.2a, and based on Bartlett's paper.[139,140] In this model (planar model), the bioelectrocatalysis system is treated as one-dimensional, with enzyme and cofactors coated on electrocatalyst-modified electrodes, forming a uniform film of thickness *L*. The enzyme is considered to be immobilized with fixed concentration and not free to diffuse, whereas cofactor NADH/NAD^+ and substrate glycerol are free to diffuse in the film.

Applying a mass balance on NAD^+, NADH, glycerol and DHA in film at position *x*, we have the following differential equation to describe diffusion and reaction within the film:

$$\frac{\partial [m]}{\partial t} = D_m \frac{\partial^2 [m]}{\partial x^2} - R_{enzyme} \qquad [5.8]$$

where *m* denotes species and D_m the species' coefficients. R_{enzyme} is the enzyme reaction rate as expressed in Eq 5.3.

At $t = 0$, under steady-state condition, the above equation becomes:

$$D_m \frac{\partial^2 [m]}{\partial x^2} = R_{enzyme} \qquad [5.9]$$

At the electrode-film interface, the flux of substrate is assumed to be 0. NAD^+ is generated by electrocatalysis, at a rate, or current, that is the function of NADH concentration. Thus, at $x = 0$, we have the following boundary conditions:

$$\frac{d[Glycerol]}{dx} = -\frac{d[DHA]}{dx} = 0 \qquad [5.10]$$

$$\frac{d[NAD^+]}{dx} = -\frac{d[NADH]}{dx} = \frac{i}{nFD_{Nh}} = \frac{j_{\max}}{nFD_{Nh}}\left(\frac{[NADH]}{K_S + [NADH]}\right)\left\{\frac{\exp[(U-V)/b]}{1+\exp[(U-V)/b]}\right\} \qquad [5.11]$$

At the film-electrolyte interface, the substrate concentration is assumed to be equal to bulk concentration (partition coefficient of substrate is 1). The gradient of NAD^+ is assumed to be 0, because NAD^+ is entrapped in the film and cannot diffuse away. Thus, at $x = L$, we have the following boundary conditions:

$$[Glycerol] = [Glycerol]_\infty \qquad [5.12]$$

$$[DHA] = 0 \qquad [5.13]$$

$$\frac{d[NAD^+]}{dt} = \frac{d[NADH]}{dt} = 0 \qquad [5.14]$$

5.3.2.2 Porous model description

To obtain high current density, a porous electrode is more promising. For example, the PMG/PTBO-CNT-carbon electrode used in Chapters 2-4 has nanopores of 50 to 200 nm diameter (See Figure 2.1b of Chapter 2). In porous interfaces for bioelectrocatalysis, we assume that cofactor, immobilized electrocatalyst and enzyme exist in the porous electrode film *L*. The

porosity of the electrode allows the possibility of better interaction between electrocatalyst, cofactor and enzyme as shown in Figure 2.1b.

In this schematic, there could be two possible cases. One (Porous-Mobile model) is mobile cofactor NADH/NAD^+, where NAD^+ is fed from the electrolyte and partitions to the film. This design was based on multi-enzyme methanol/air biofuel cell by Addo *et al*[54] and Kar *et al.*[137] Another (Porous-Entrapped model) assumes that cofactor is entrapped in the film with constant diffusion coefficient.

In both cases (Porous-Mobile and Porous-Entrapped), we assume fast transport on the scale of electrode pores. Applying steady-state mass balance equations within the film, we can obtain:

$$D_N \frac{\partial^2 [NAD^+]}{\partial x^2} = -R_{enzyme} + R_{electrode} \quad [5.15]$$

$$D_{Nh} \frac{\partial^2 [NADH]}{\partial x^2} = R_{enzyme} - R_{electrode} \quad [5.16]$$

$$D_{Glycerol} \frac{\partial^2 [Glycerol]}{\partial x^2} = -R_{enzyme} \quad [5.17]$$

$$D_{DHA} \frac{\partial^2 [DHA]}{\partial x^2} = R_{enzyme} \quad [5.18]$$

In both cases (Porous-Mobile model and Porous-Entrapped model), at the electrode-film interface ($x = 0$), the fluxes of all species are assumed to be 0. Thus, at $x = 0$, the boundary condition is:

$$\frac{d[m]}{dx} = 0 \qquad [5.19]$$

In the Porous-Mobile model, at the film-electrolyte interface, the substrate/product and cofactor NADH/NAD^+ concentrations are assumed to be equal to bulk concentration (partition coefficients are assumed to be 1). Thus, at $x = L$, the boundary conditions are expressed as:

$$[Glycerol] = [Glycerol]_\infty;\ [DHA] = 0;\ [NAD^+] = [NAD^+]_0;\ [NADH] = 0; \qquad [5.20]$$

In the Porous-Entrapped model, cofactor is assumed to be entrapped in the film. Thus at $x = L$, instead of Eq 5.19 and Eq 5.20, the boundary conditions regarding cofactor are expressed as Eq 5.14.

5.3.2.3 Nondimensionalization

The following non-dimensional variables may be introduced:

$$a = [NAD^+]/[NAD^+]_0;\ b = [Glycerol]/[Glycerol]_\infty;$$

$$q = [NADH]/[NAD^+]_0;\ p = [DHA]/[Glycerol]_\infty; \qquad [5.21]$$

$$\sigma_a = K_{mA} / [NAD^+]_0;\ \sigma_b = K_{mB} / [Glycerol]_\infty;$$

$$\sigma_q = K_{mQ} / [NAD^+]_0;\ \sigma_p = K_{mP} / [Glycerol]_\infty; \quad [5.22]$$

$$\alpha_a = K_{ia} / [NAD^+]_0;\ \alpha_b = K_{ib} / [Glycerol]_\infty;$$

$$\alpha_q = K_{iq} / [NAD^+]_0;\ \alpha_p = K_{ip} / [Glycerol]_\infty; \quad [5.23]$$

$$f_r = k_f / k_r; \quad [5.24]$$

$$\sigma_{Nh} = K_S / [NAD^+]_0; \quad [5.25]$$

$$\chi = x / L \quad [5.26]$$

$$\varepsilon = \frac{D_{NADH}[NAD^+]_0}{D_{Glycerol}[Glycerol]_\infty} = \frac{D_{NAD^+}[NAD^+]_0}{D_{Glycerol}[Glycerol]_\infty} \quad [5.27]$$

where a, b, p and q are non-dimensional concentrations for NAD^+, glycerol, DHA and NADH, respectively. σ_a, σ_b, σ_p and σ_q are non-dimensional Michaelis-Menten constants, and α_a, α_b, α_p and α_q are non-dimensional enzyme dissociation constants. f_r is the ratio of turnover numbers for

forward reaction and backward reaction, σ_{Nh} is non-dimensional adsorption constant for electrochemical reaction. χ is non-dimensional film thickness. ε represents normalized diffusivity.

The non-dimensional enzyme reaction rate can then be expressed as:

$$r'_{Enz} = \frac{Da_{\text{Glycerol}}\left(ab - \frac{pq}{K_{eq}}\right)}{\alpha_a \sigma_b + \alpha_b \sigma_a + \sigma_a b + \frac{f_r \sigma_q p}{K_{eq}} + \frac{f_r \sigma_p q}{K_{eq}} + ab + \ldots + \frac{f_r pq}{K_{eq}} + \frac{\sigma_a bq}{\sigma_q} + \frac{abp}{\alpha_p} + \frac{f_r bpq}{\alpha_b K_{eq}}} \quad [5.28]$$

where Da_{Glycerol} is the Damkohler number, representing the ratio of reaction rate to diffusion rate, and is comparable to the Thiele Modulus.[2,121] Damkohler numbers for substrate glycerol and product DHA are defined as:

$$Da_{\text{Glycerol}} = \frac{k_f [E] L^2}{D_{Glycerol} [Glycerol]_\infty} \quad [5.29]$$

$$Da_{\text{DHA}} = \frac{k_f [E] L^2}{D_{DHA} [Glycerol]_\infty} \quad [5.30]$$

Similarly, the non-dimensional form of the electrode reaction rate is expressed as:

$$r'_{electrode} = \frac{Da_{\mathrm{NADH}} \times q}{\sigma_{Nh} + q} \qquad [5.31]$$

where Damkohler number for NADH and NAD^+, are defined as:

$$Da_{\mathrm{NADH}} = Da_{\mathrm{NAD^+}} = \frac{L^2}{D_{Glycerol}[Glycerol]_\infty} \frac{j_{\max} S}{nFV_r} \left\{ \frac{\exp[(U-V)/b]}{1+\exp[(U-V)/b]} \right\} \qquad [5.32]$$

In planar model, by substituting Eq 5.21-32 into Eq 5.9, the non-dimensional differential equations are obtained:

$$\frac{d^2a}{d\chi^2} = \frac{d^2q}{d\chi^2} = -\frac{r'_{enz}}{\varepsilon};\ \frac{d^2b}{d\chi^2} = \frac{d^2p}{d\chi^2} = -r'_{enz}; \qquad [5.33]$$

Similarly, the non-dimensional differential equations in porous models are given by:

$$\frac{d^2a}{d\chi^2} = \frac{d^2q}{d\chi^2} = -\frac{r'_{enz}}{\varepsilon} + \frac{r'_{electrode}}{\varepsilon};\ \frac{d^2b}{d\chi^2} = \frac{d^2p}{d\chi^2} = -r'_{enz}; \qquad [5.34]$$

5.3.2.4 Bioreactor performance calculation

Integration of reaction rate over the film thickness ($0 \le \chi \le 1$) gives flux per unit electrode surface area at the film-electrolyte boundary:

$$J = \left(\frac{D_{Glycerol}[Glycerol]_0}{L} \right) \int_0^1 r'_{enz}\, d\chi \qquad [5.35]$$

where J has units of mol s^{-1} cm^{-2}.

5.3.2.5 Parameter values

Relevant parameters, assumed nominal and calculated Damkohler number values are shown in Table 5.2. The parameter values of NADH electrochemical oxidation kinetics are from Chapter 2. The parameters for enzyme kinetics are based on experimental data from our lab and our collaborators. The diffusivity of NADH in aqueous electrolyte, D_{NADH}, was found to be 1.0×10^{-5} cm^2 s^{-1} by Levich analysis in Chapter 2, and is comparable to literature values.[136,160,161] D_{NADH} may be much lower when entrapped in a porous electrode or film. For example, Choi *et al* reported D_{NADH} to be ~10^{-9} cm^2 s^{-1} in Nafion.[200,201] Tetra butyl ammomium bromide modified Nafion (TBAB-Nafion) has enlarged micellar pores, allowing faster diffusion than unmodified Nafion.[202] In Kar *et al*'s model, $D_{NADH} = 3.3 \times 10^{-8}$ cm^2 s^{-1} was assumed.[137] This value is higher than that in unmodified Nafion and still much lower than in aqueous electrolyte, and is used in this work for both D_{NADH} and D_{NAD^+}. The diffusion coefficient for glycerol was reported to be 2.9×10^{-7} cm^2 s^{-1} for enzyme immobilized TBAB-Nafion,[203] and is used in this work for both $D_{Glycerol}$ and D_{DHA}. Wen *et al* measured nanotube layer thickness as a function of loading by microscopic measurements, and calculated a bulk density of hydrogel coated on nanotube layer.[157] Based on their data,[157] the thickness of carbon nanotube layer was obtained to be 10 μm for 0.85 mg cm^{-2} loading and this value is used for film thickness L in this work. The porosity of carbon nanotube is 20%,[157] which allows the loading of immobilized enzyme to be as high as 1 M. All the partition coefficients are assumed

to be 1. The material balance equations and accompanying boundary conditions for all the models were solved using MATLAB. The codes are available in the Appendix.

Table 5.2 Parameters and values involved[a]

Parameter	Value	Reference
Equilibrium constant for enzyme reaction, K_{eq}	0.02	Vieille lab
Turnover number of glycerol oxidation, k_f	3.3 s^{-1}	Our lab
Turnover number of DHA reduction, k_r	7.9 s^{-1}	Our lab
Michaelis-Menten constant for NAD^+, K_{mA}	8.2 μM	Our lab
Michaelis-Menten constant for glycerol, K_{mB}	140 mM	Our lab
Michaelis-Menten constant for NADH, K_{mQ}	14 μM	Vieille lab
Michaelis-Menten constant for DHA, K_{mP}	13 mM	Vieille lab
Dissociation constant of NAD^+, K_{ia}	23 μM	Our lab
Dissociation constant of glycerol, K_{ib}	1.5×10^4 mM	[205,206]
Dissociation constant for NADH, K_{iq}	12 μM	Our lab
Dissociation constant for DHA, K_{ip}	11 mM	[206]
Diffusion coefficient for NADH/NAD^+, D_{Nh}, D_N	3.3×10^{-8} cm^2 s^{-1}	[137]
Diffusion coefficient for glycerol/DHA, D_{Gly}, D_{DHA}	2.9×10^{-7} cm^2 s^{-1}	[203]
Reactor volume, V_r	10 cm^3	Set
Applied potential, V	0.4 V	Set
Electrode geometric surface area, S	1 cm^2	Set
Film thickness, L	10 μm	[157]
Enzyme loading, *[E]*	100 μM	Set
Cofactor loading, *[NAD^+]*	10 mM	Set
Substrate concentration, *[Glycerol]*	1 mM	Set
Damkohler number for glycerol/DHA, $Da_{Glycerol}$, Da_{DHA}	1.1	Use Eq 5.29-30
Damkohler number for NADH/NAD^+, Da_{NADH}, Da_{NAD^+}	455	Use Eq 5.32

a: parameter values regarding NADH electrocatalytic reaction using PMG-CNT have been shown in Chapter 2

5.4 Results and Discussion

Bioelectrocatalytic conversion and key parameters in kinetics were studied using the kinetic model. As will be discussed later, mass-transport analysis indicates that the enzyme kinetics are the rate-limiting under baseline conditions (Table 5.2). An optimal reactor design was obtained, which balances the rate of mass transfer with kinetics rates.

5.4.1 Conversion in bioelectrocatalysis

The kinetic model (Section 5.3.1) represents an initial value problem that can be solved numerically. The transient concentration profiles in the bioconversion process are shown in Figure 5.3. Using the baseline conditions shown in Table 5.1, while reaction starts, NADH is immediately generated from NAD^+ by the enzyme reaction. After 0.1 hr, due to glycerol depletion, the electrochemical reaction rate exceeds the enzyme reaction rate under the baseline condition, and NADH concentration begins to decrease. Thus a maximum in NADH concentration observed close to the initial point.

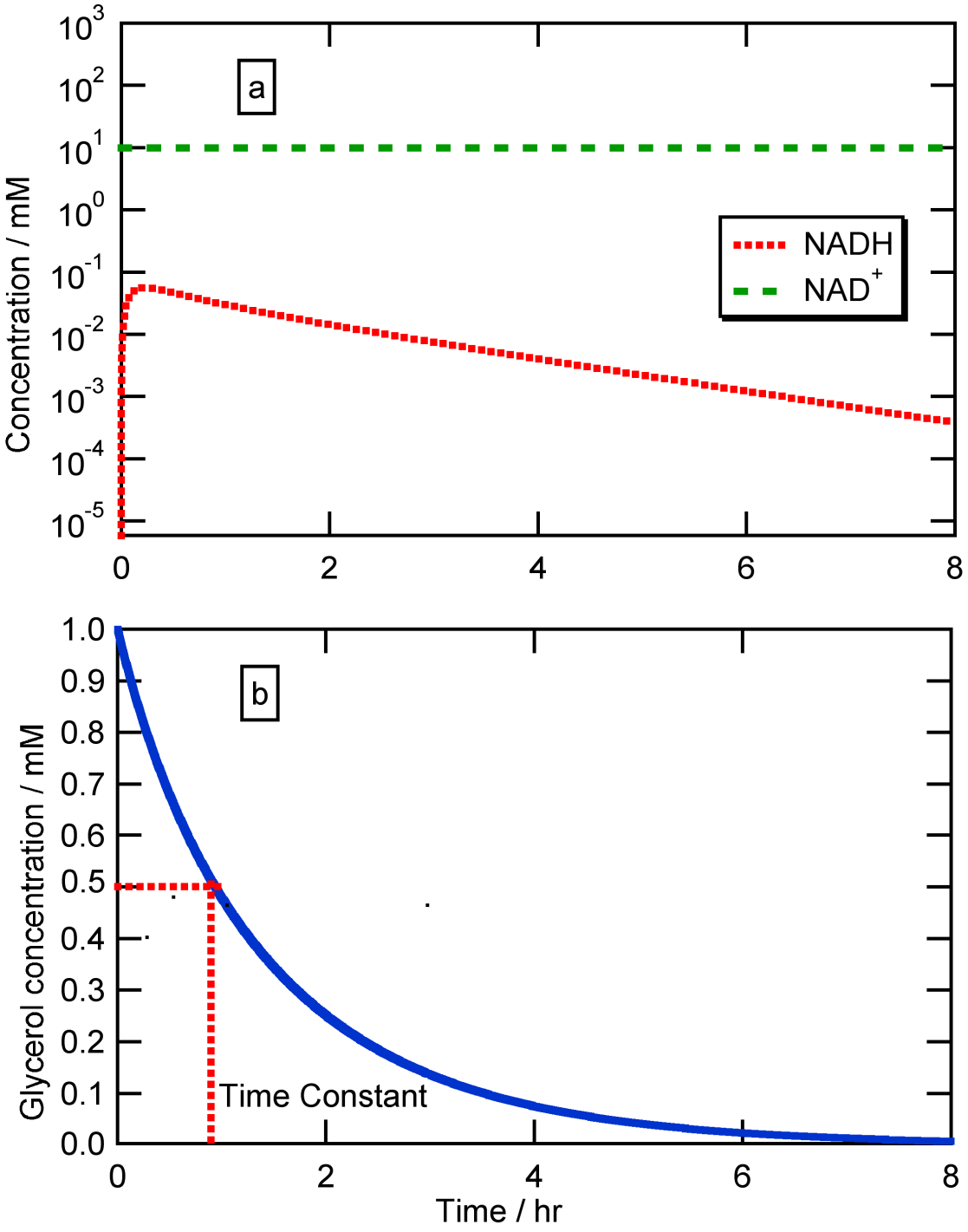

Figure 5.3 Conversions of redox cofactor (a) NADH/NAD^+ and (b) substrate glycerol in bioelectrocatalysis

To evaluate the efficiency of bioreactor, we define the time constant, τ as the time to achieve 50% substrate (glycerol) conversion. In commercial microbial processes for DHA production, τ is around 32 hrs.[194,195] A recently reported chemical process requires τ around 5 hrs.[2a] Using parameter values listed in Table 5.1, the time constant of the bioelectrocatalytic reactor for DHA production is 0.9 hr, as shown in Figure 5.3.

5.4.2 Key parameters in kinetics

Key parameters determining kinetics in bioreactor include surface area/volume ratio (*S/V*), electrocatalytic activity (j_{max}), cofactor loading ([NAD^+]) and enzyme concentration ([E]). The first two, *S/V* and j_{max} effect the electrochemical reaction rate, while [E] determines enzyme reaction rate and [NAD^+] impacts both reactions. As shown in Figure 5.4a, time constant is plotted as a function of surface area/volume ratio and cofactor loading ([NAD^+]). This plot suggests that, to achieve low time constant ($\tau \leq 3$ hr), the surface area/volume ratio should be higher than 0.075 cm^{-1} and the cofactor NAD^+ concentration should be higher than 0.5 mM, for the current enzyme conditions. In previous chapters, we described a high-rate NADH oxidizing electrode with a surface area/volume ratio of up 0.1 cm^{-1}, satisfying such requirements. The required cofactor concentration can also be achieved, since Addo *et al*[54] used larger NAD^+ (1.5 mM) concentration in their dehydrogenase-based fuel cell.

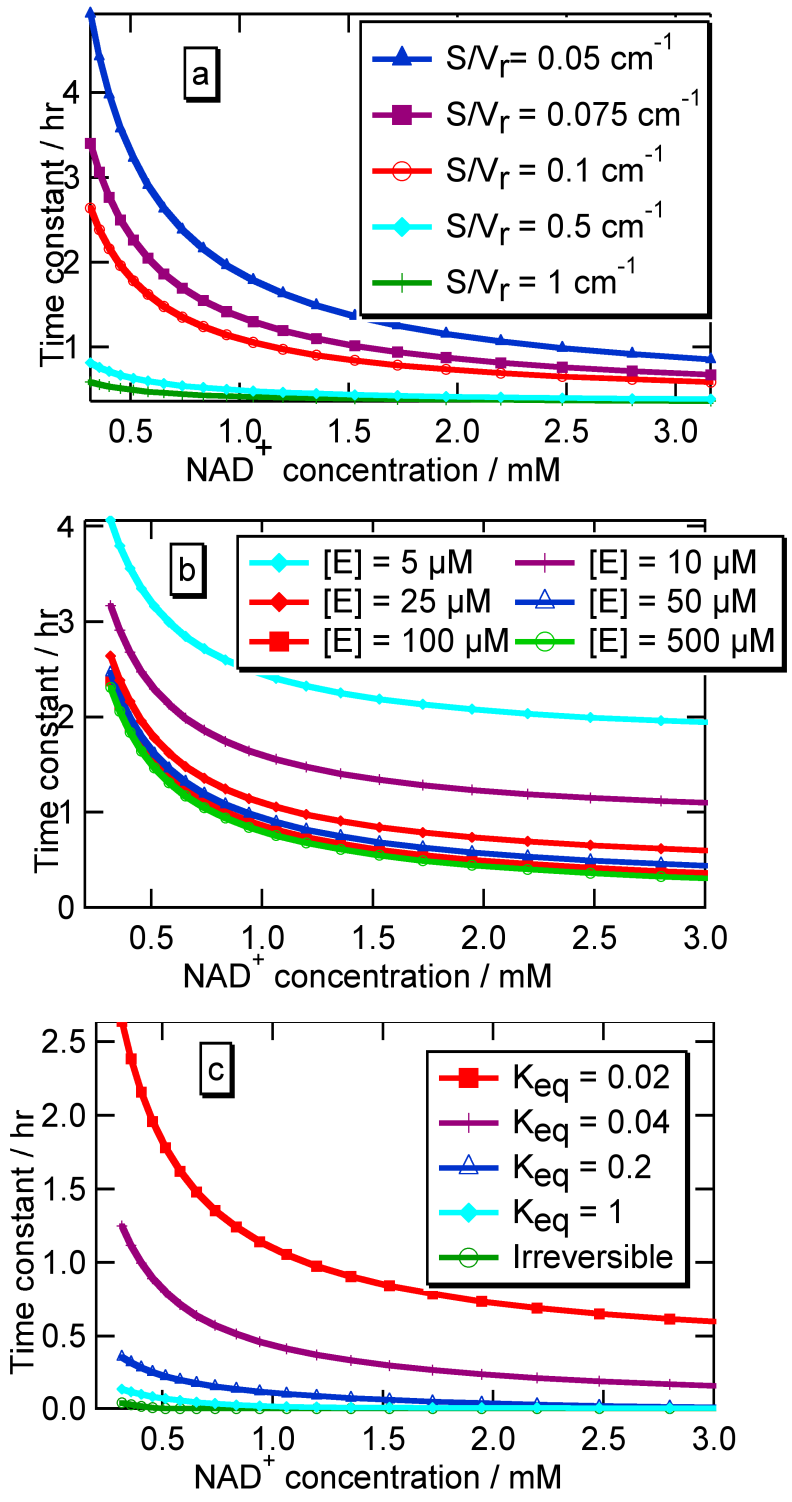

Figure 5.4 Time constant τ varying with a) Surface /volume ratio and NAD^+ loading; b) Enzyme concentration and NAD^+ loading; c) Enzyme equilibrium and NAD^+ loading.

The impact of enzyme concentration is shown in Figure 5.4b, which suggests that, to achieve effective bioelectronic conversion, the enzyme concentration should be higher than 25 μM. This value is realistic in aqueous solution, based on the experiments of enzyme kinetics in our lab. For immobilized enzymes, this concentration within the range of typical immobilized concentrations (~ 20 mM), based on the reported enzyme-immobilized systems.[204]

From Figure 5.4c, we could see that enzyme equilibrium also plays an important role in bioreactor performance. The parameter values in Table 5.2 are based on glycerol dehydrogenase whose forward reactivity is smaller than backward reactivity ($K_{eq} = 0.02$). Increasing equilibrium coefficient K_{eq} corresponds to increasing irreversibility, leading to dramatically decreased time constant. For other dehydrogenase-based reactions with increased K_{eq}, lower time constant may be obtained.

5.4.3 Kinetics-transport models under baseline conditions

The mathematical expressions of nondimensional Damkohler numbers for enzymatic reaction, $Da_{Glycerol}$, and NADH oxidation, Da_{NADH}, involve the key parameters in kinetics and mass transport that determine bioconversion performance. According to equations 5.29 and 5.32, $Da_{Glycerol}$ and Da_{NADH} depend on film thickness, species concentration and diffusivities. Moreover, $Da_{Glycerol}$ depends on enzymatic reaction rate and enzyme concentration. Da_{NADH}

depends on electrocatalysis rate, surface area, and applied potential. $Da_{Glycerol}$ and Da_{NADH} are the ratio of the reaction rate to diffusion rate, representing the degree of mass transport limitation.

Moreover, considering the kinetics of glycerol dehydrogenase (Eq 5.3 and 5.28), glycerol conversion rate reaches a maximum when glycerol and NAD^+ concentrations are equal to their bulk concentration, while DHA and NADH concentrations equal to zero. Using the parameter values in Table 5.2, the nondimensional glycerol conversion rate is calculated as:

$$(r'_{enz})_{\max} = \frac{Da_{Glycerol} \times ab}{\alpha_a \sigma_b + \alpha_b \sigma_a + \sigma_a b + ab} = \frac{Da_{Glycerol}}{13} \qquad [5.36]$$

This indicate that, when $Da_{Glycerol} < 13$, glycerol conversion rate is lower than its diffusion rate. Conversely, diffusion is the lower-rate step when $Da_{Glycerol} > 13$.

Additionally, the ratio $Da_{Glycerol}/Da_{NADH}$ is expressed as:

$$\frac{Da_{\text{Glycerol}}}{Da_{\text{NADH}}} = \frac{k_f[E]}{\frac{j_{\max} S}{nFV_r}\left\{\frac{\exp[(U-V)/b]}{1+\exp[(U-V)/b]}\right\}} \qquad [5.37]$$

This expression contains the parameters that determine kinetics as discussed in Section 5.4.2. The value of Eq 5.36 indicates the relative rate of the two reactions.

Under baseline conditions shown in Table 5.2, $Da_{Glycerol}$ = 1.1. Using our high-performance NADH oxidizing electrodes that were described in Chapter 2, Da_{NADH} = 455. $Da_{Glycerol}$ (= 1.1) is less than 13 and much smaller than Da_{NADH} (= 455), suggests that the enzymatic reaction is rate limiting.

Concentrations of NAD^+, glycerol, NADH and DHA govern bioconversion reaction rate. Under baseline conditions, because of low $Da_{Glycerol}$ (= 1.1), NAD^+ and glycerol are consumed at low rate. Because of high Da_{NADH} (= 455), NADH is oxidized at high rate, leading to close to complete regeneration of NAD^+. All concentration profiles were found to be more or less flat in the film (data not shown), indicating that the diffusion limitations are negligible. Thus, under the baseline condition, mass-transport in the film does not limit bioreactor performance, because the enzyme reaction is slow. To take advantage of this fact, under the baseline conditions, we can neglect transport and use kinetic model for bioreactor simulation.

5.4.4 Bioconversion performance

$Da_{Glycerol}$ may be increased by, for example, increasing enzyme loading. The predicted glycerol flux at the film-electrolyte boundary as a function of DaGlycerol and enzyme equilibrium constants were calculated for three electrode designs as shown in Figure 5.5. Figures 5.6-5.9 display the corresponding nondimensional concentration profiles, flux of glycerol, and local rate of consumption in the film.

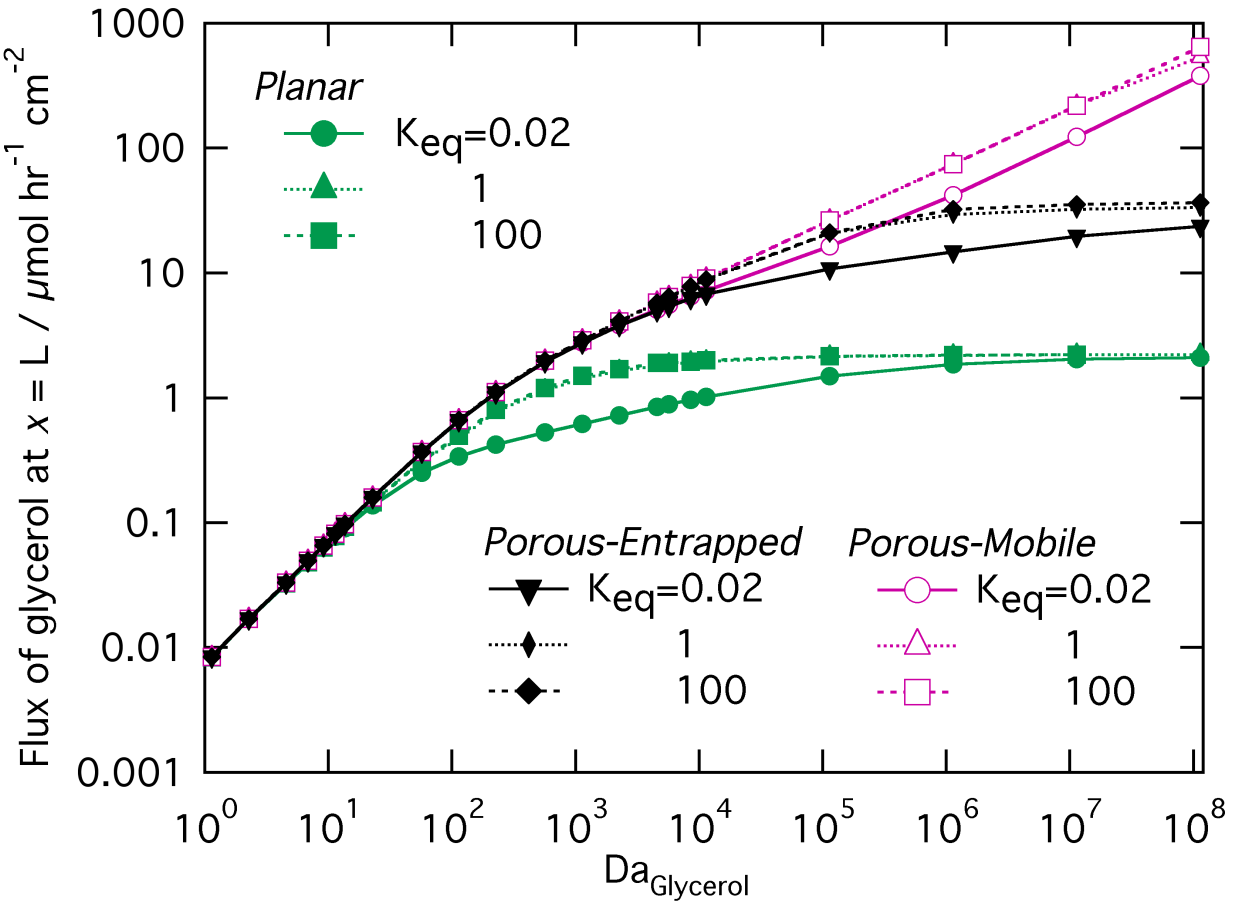

Figure 5.5 Effect of $Da_{Glycerol}$ on flux for kinetics-mass transport models under different enzyme equilibrium constants, with fixed Da_{NADH} = 455. Insert: plot for $Da_{Glycerol}$ = 0 - ~25

As shown in Figure 5.5, for all designs, glycerol flux at film-electrolyte boundary increases with $Da_{Glycerol}$ and enzyme equilibrium constants. When $Da_{Glycerol}$ is less than 13, concentration profiles are more or less flat (data not shown), indicating negligible mass-transport control, with the enzyme reaction as the rate-limiting step. In this region, all cases show very similar flux and increasing $Da_{Glycerol}$ leads to a linear increase of reaction rate, confirming control by enzyme reaction.

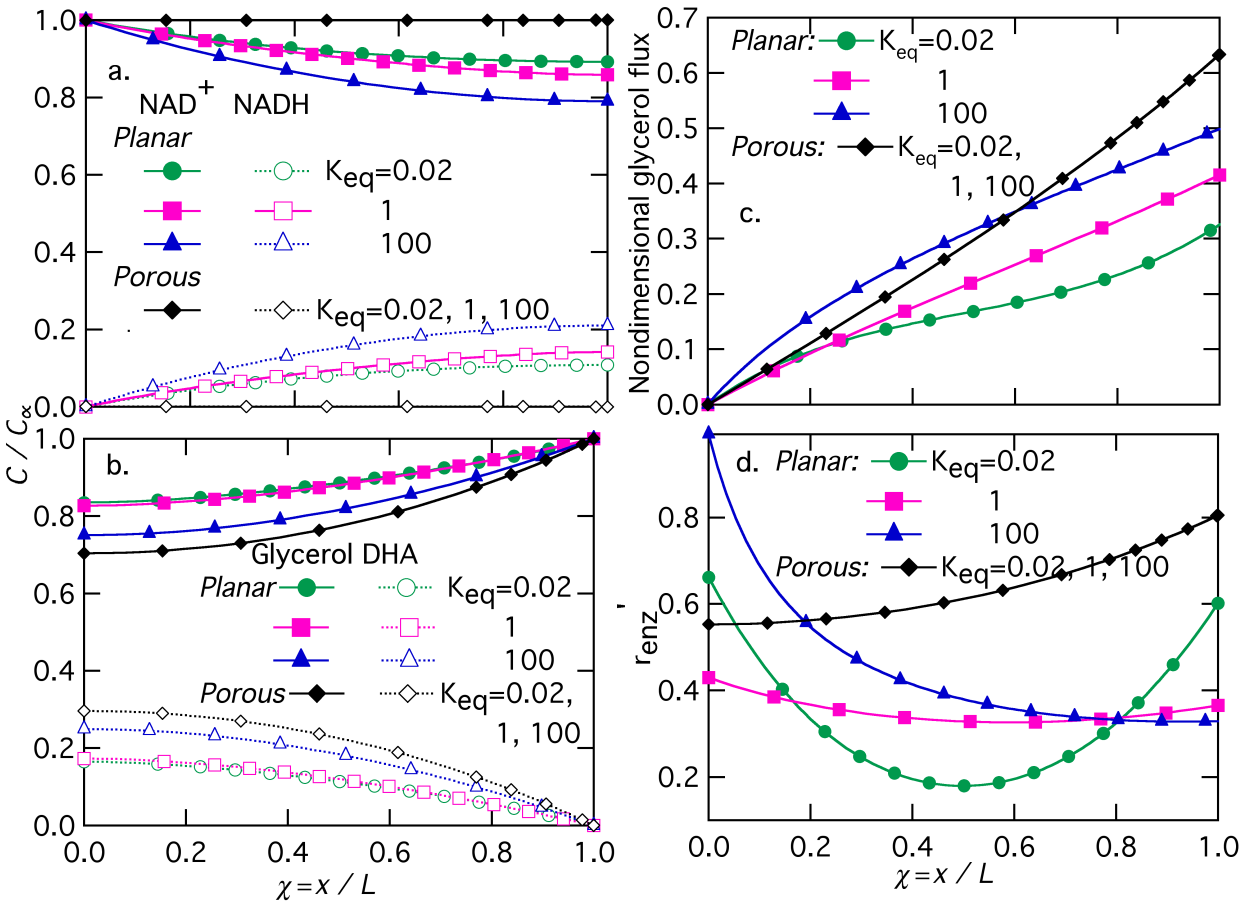

Figure 5.6 Simulation results of kinetics-mass transport models under different enzyme equilibrium constants at $Da_{Glycerol}$ = 100, Da_{NADH} = 455 a) Cofactor NAD^+/NADH concentration; b) Substrate glycerol and product DHA concentration; c) Flux of glycerol; d) Reaction rate of glycerol consumption.

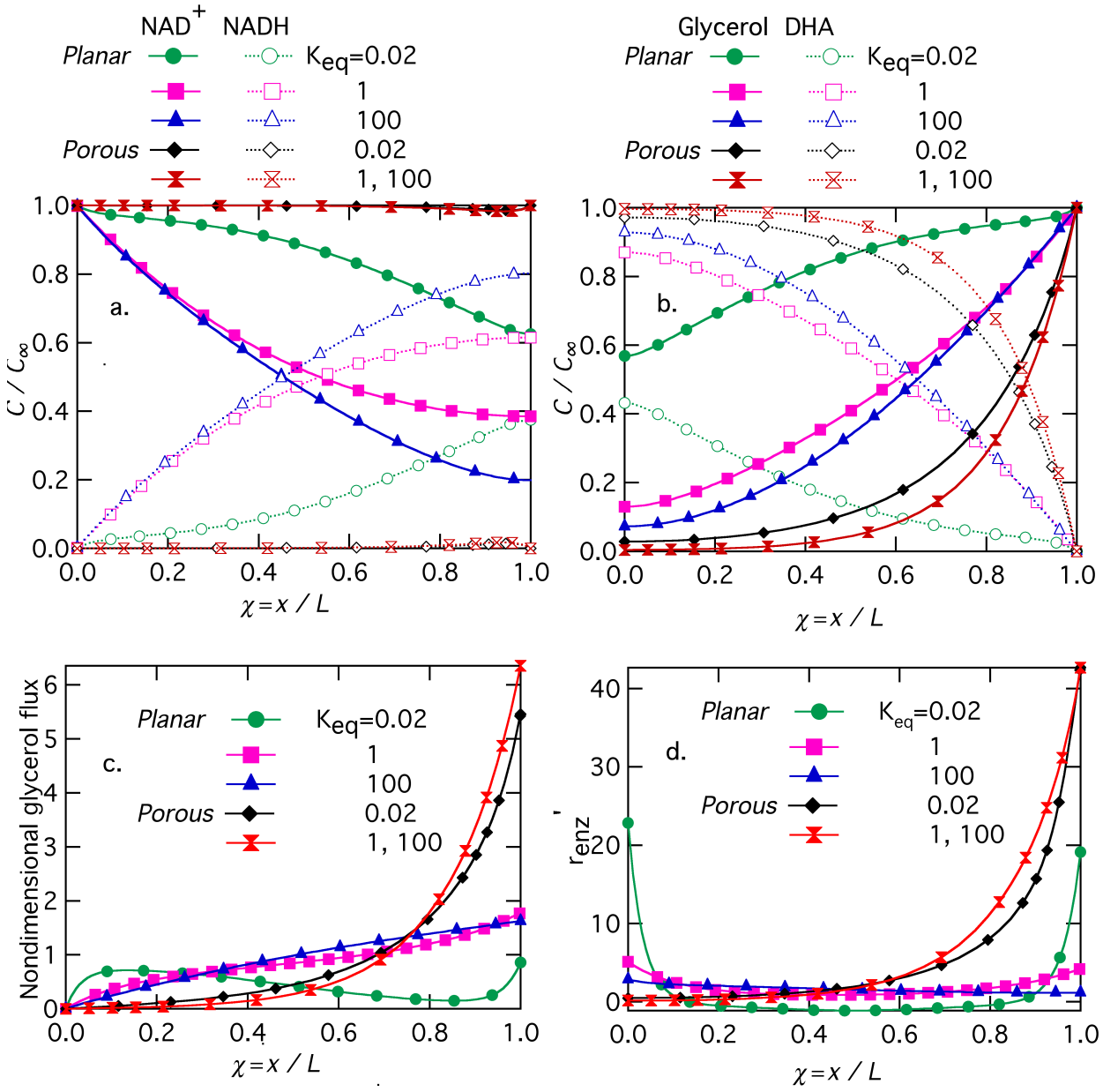

Figure 5.7 Simulation results of kinetics-mass transport models under different enzyme equilibrium constants at $Da_{Glycerol} = 6000$, $Da_{NADH} = 455$ a) Cofactor NAD^+/NADH concentration; b) Substrate glycerol and product DHA concentration; c) Flux of glycerol; d) Reaction rate of glycerol consumption

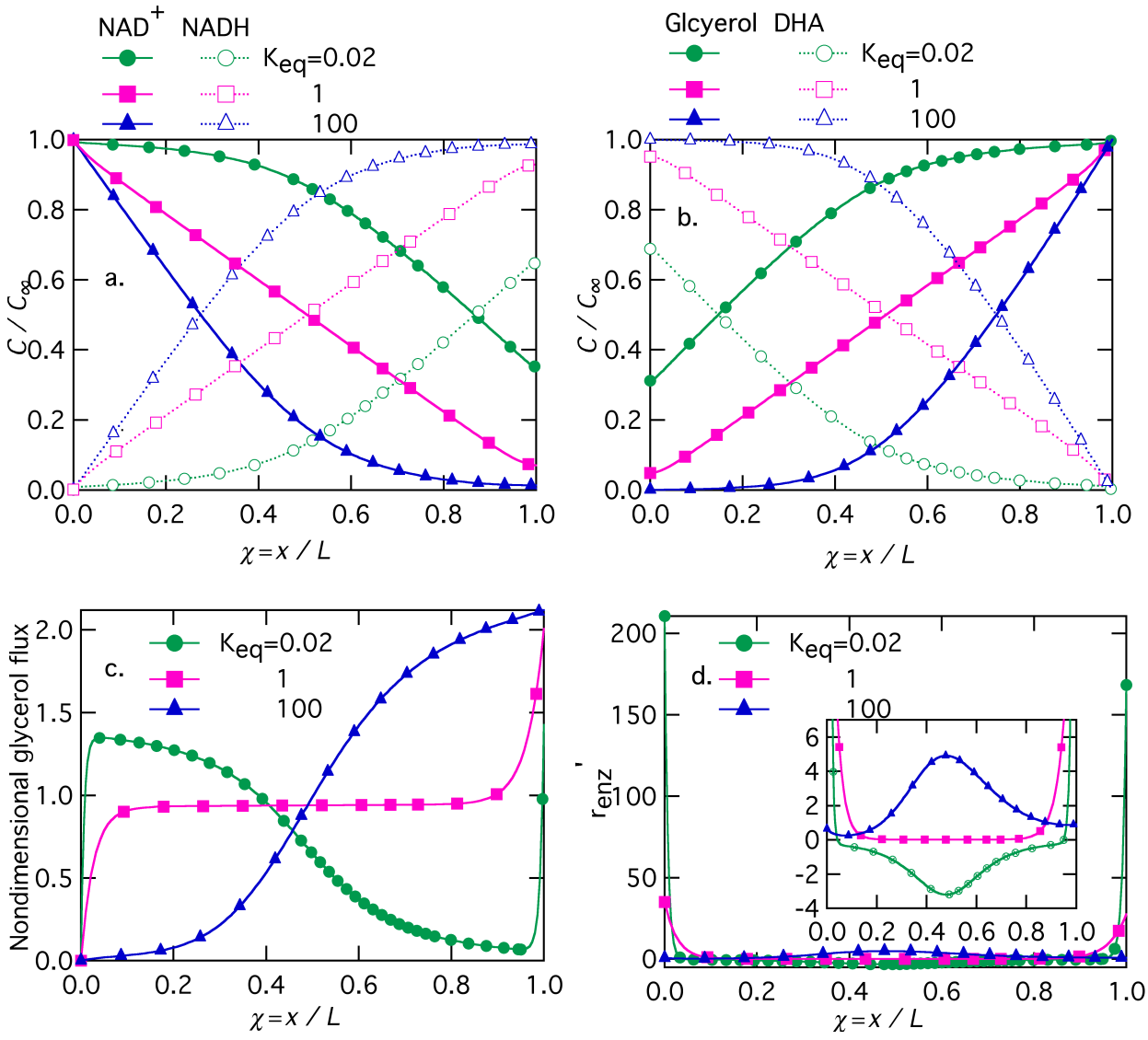

Figure 5.8 Simulation results of planar interface model under different enzyme equilibrium constants at $Da_{Glycerol} = 10^5$, $Da_{NADH} = 455$ a) Cofactor NAD^+/NADH concentration; b) Substrate glycerol and product DHA concentration; c) Flux of glycerol; d) Reaction rate of glycerol consumption

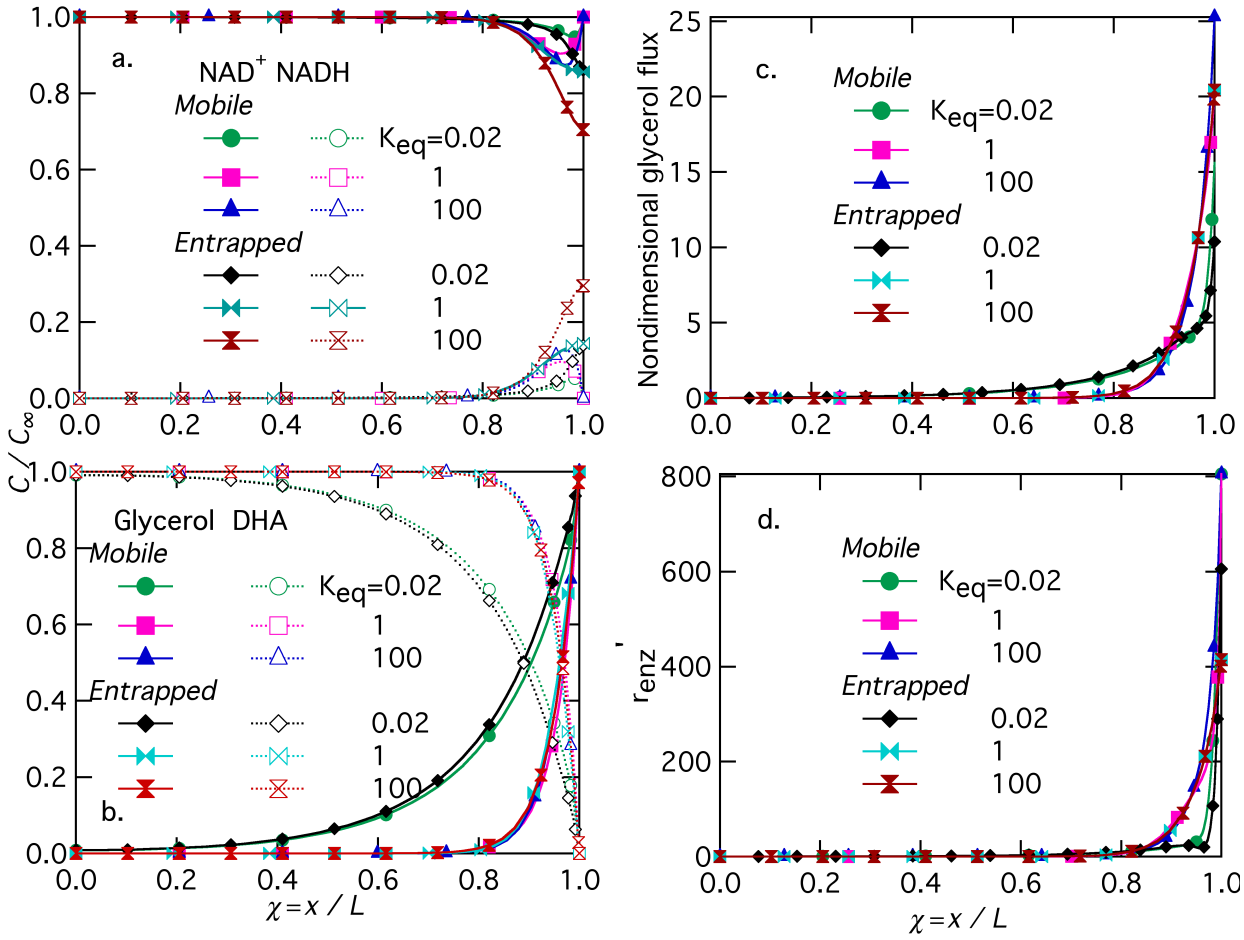

Figure 5.9 Simulation results of porous interface models under different enzyme equilibrium constants at $Da_{Glycerol} = 10^5$, $Da_{NADH} = 455$ a) Cofactor NAD^+/NADH concentration; b) Substrate glycerol and product DHA concentration; c) Flux of glycerol; d) Reaction rate of glycerol consumption

When $Da_{Glycerol}$ was further increased to be larger than 13, control is shared by the enzyme reaction and diffusion limitation. At $Da_{Glycerol} = 100$, in the planar design, gradients of NAD^+, glycerol, NADH and DHA concentrations were observed, indicating incipient mass transfer limitation, as shown in Figure 5.6a-b. NAD^+ is generated by the electrocatalyst at the film-electrode boundary and by the reversible enzyme reaction within the film. The NAD^+ concentration reaches its maximum at film-electrode interface and decreases towards film-electrolyte interface. Glycerol is fed from electrolyte, has maximum values at film-electrolyte interface and decreases towards film-electrode interface. As shown in Eq 5.27 and 5.33, under baseline conditions in Table 5.2, because $D_{Glycerol} \times [Glycerol]_\infty \approx D_{NAD^+} \times [NAD^+]_\infty$, these profiles have almost the same shape but different directions. Moreover, these gradients become steeper with increased K_{eq}, as a result of increased enzymatic reaction rate (Eq 5.28), corresponding to higher flux (Figure 5.5 and 5.6c) and higher net glycerol consumption rate (Figure 5.6d).

The porous interfaces permit electrocatalysts to be more or less collocated with the enzyme within the film instead of at the boundary. Because of high Da_{NADH} (= 455), the regeneration of NAD^+ by NADH electrocatalysis is close to complete in the film. Thus NAD^+ concentration is close to 1 and NADH concentration close to 0 throughout the film, which significantly eliminates the reverse enzymatic reaction and promotes glycerol consumption. Therefore, as shown in Figure 5.5-5.8, compared to the planar interface, the porous interface

show steeper glycerol concentration gradient, higher flux, net glycerol consumption rate and smaller impact by K_{eq}. At $Da_{Glycerol} = 100$, two porous models under three K_{eq} yield the same results.

At $Da_{Glycerol} = 6000$, as displayed in Figure 5.7, steeper concentration gradients and higher rate were obtained for all cases, as compared to $Da_{Glycerol} = 100$. Moreover, in the planar interface, concentration gradients at $K_{eq} = 0.02$ show different concave shape from these at other K_{eq} values. In this case, glycerol is consumed near two boundaries and generated slightly in the film. At $K_{eq} = 1$, glycerol is also mainly consumed near boundaries, and maintains enzyme reaction equilibrium throughout the film. Nevertheless, the net glycerol consumptions at both $K_{eq} = 0.02$ and 1 are still positive. In the porous interface, compared to the results at $K_{eq} = 0.02$, slightly steeper concentration gradients were observed at $K_{eq} = 1$ and 100, corresponding to slightly higher net glycerol consumption rate.

Simulation results for the planar interface at high Damkohler number ($Da_{Glycerol} = 1 \times 10^5$) are shown in Figure 5.8. Steep concentration gradients were observed as a result of high enzyme loading. Interface for $K_{eq} = 100$ demonstrates maximum glycerol consumption rate at $\chi = \sim 0.5$ due to symmetric diffusion. Near the film-electrode boundary (at $\chi < \sim 0.5$), glycerol conversion rate is limited by glycerol depletion. Near the film-electrolyte

boundary (at χ > ~0.5), it is limited by NAD^+ diffusion. Conversely, the interface for K_{eq} = 0.02 shows the minimum glycerol consumption rate at χ = ~0.5.

As shown in Figure 5.5, at high Damkohler number ($Da_{Glycerol} \geq 1 \times 10^5$), the glycerol flux at film-electrolyte boundary reaches a plateau value, which equals to:

$$J_{\text{planar-max}} = \frac{2 \times D_{Glycerol}[Glycerol]_0}{L} \qquad [5.36]$$

The flux obtained from the two porous models only varies when there is a variation in NADH/NAD^+ concentration profiles. As shown in Figure 5.9, the two porous models show different NAD^+ concentration profiles near the film-electrolyte boundary because of different boundary conditions at film-electrolyte boundary. At high Damkohler number ($Da_{Glycerol} \geq 1 \times 10^5$, as shown in Figure 5.5), the flux in porous-entrapped model tends to reach a plateau, suggesting a diffusion control, whereas the flux in porous-mobile model still increases, indicating a shared controlled by enzyme reaction and diffusion.

5.4.5 Model validation.

To validate model results, we applied the models to a glycerol biosensor involving NADH electrochemical regeneration reported by Zhao et al.[12,37] In their system, a single carbon fiber with branched nanotubes was use for NADH electrocatalysis. With the presence cofactor NAD^+ and glycerol dehydrogenase, both freely diffusing, NADH oxidation current was used to

indicate the concentration of glycerol, NAD^+, or glycerol dehydrogenase when the other two species were provided in excess.[37] The main difference between their system and ours is the electrode geometry and the source of glycerol dehydrogenase.

To validate the model, electrochemical kinetic parameters based on glassy carbon were used, except for the value of electrochemical reaction rate, j_{max}, which was decreased to 2 mA cm^{-2} in order to have better match with their reported fiber electrode activity.[178] Some parameters for glycerol dehydrogenase kinetics, including turnover number of glycerol oxidation, k_f, Michaelis-Menten constant for glycerol, K_{mB}, dissociation constant for NADH, K_{iq}, dissociation constant for DHA, K_{ip}, and equilibrium constant for enzyme reaction, K_{eq}, were changed to their reported values.[12] These parameter values and Damkohler number values are shown in Table 5.3. Since both enzyme and cofactor are freely diffusing in their report, and the Damkohler number of glycerol was estimated to be $Da_{Glycerol} < 15$ based on the above system parameters (shown in Table 5.3), mass transfer limitations can be neglected and a kinetic model was utilized for simulation.

Table 5.3 Parameters and values for model validation[b]

Parameter	Value	Reference
Equilibrium constant for enzyme reaction, K_{eq}	95	[12]
Turnover number of glycerol oxidation, k_f	121 s^{-1}	[12]
Turnover number of DHA reduction, k_r	7.9 s^{-1}	Our lab
Michaelis-Menten constant for NAD^+, K_{mA}	8.2 μM	Our lab
Michaelis-Menten constant for glycerol, K_{mB}	26 mM	[37]
Michaelis-Menten constant for NADH, K_{mQ}	14 μM	Vieille lab
Michaelis-Menten constant for DHA, K_{mP}	13 mM	Vieille lab
Dissociation constant of NAD^+, K_{ia}	23 μM	Our lab
Dissociation constant of glycerol, K_{ib}	1.5×10^{4} mM	[205,206]
Dissociation constant for NADH, K_{iq}	28 μM	Our lab
Dissociation constant for DHA, K_{ip}	0.064 mM	[12]
Diffusion coefficient for NADH/NAD^+, D_{Nh}, D_N	3.3×10^{-8} cm^2 s^{-1}	[137]
Diffusion coefficient for glycerol/DHA, D_{Gly}, D_{DHA}	2.9×10^{-7} cm^2 s^{-1}	[203]
Reactor volume, V_r	4 cm^3	[37]
Applied potential, V	0.515 V	[37]
Electrode geometric surface area, S	4.5×10^{-4} cm^2	[37]
Film thickness, L	10 μm	[157]
Enzyme loading, *[E]*	0-0.1 U mL^{-1}	[37]
Cofactor loading, *[NAD^+]*	2 mM	[37]
Substrate concentration, *[Glycerol]*	0-3 mM	[37]
Damkohler number for glycerol/DHA, $Da_{Glycerol}$, Da_{DHA}	0-15	Use Eq 5.29-30
Damkohler number for NADH/NAD^+, Da_{NADH}, Da_{NAD^+}	0.002	Use Eq 5.32
Electrochemical reaction rate, j_{max}	2 mA cm^{-2}	[37]

Simulation results for glycerol and enzyme concentration profiles show good fit with experimental data, as displayed in Figure 5.10. Current density increases while substrate glycerol

(Figure 5.10a) or enzyme (Figure 5.10b) concentration increases. Both curves show apparent Michaelis-Menten kinetics with electrochemical-reaction limiting plateau value $j_{\text{max\_apparent}}$ given by:

$$j_{\text{max\_apparent}} = j_{\text{max}} \times \frac{[NAD^+]_0}{K_S + [NAD^+]_0} \left\{ \frac{\exp[(U-V)/b]}{1+\exp[(U-V)/b]} \right\} \qquad [5.37]$$

where [NAD^+] is the concentration of freely diffusing cofactor in the biosensor set-up. *K*s, *V*, *U* and *b* have the same meanings as in Chapter 2.

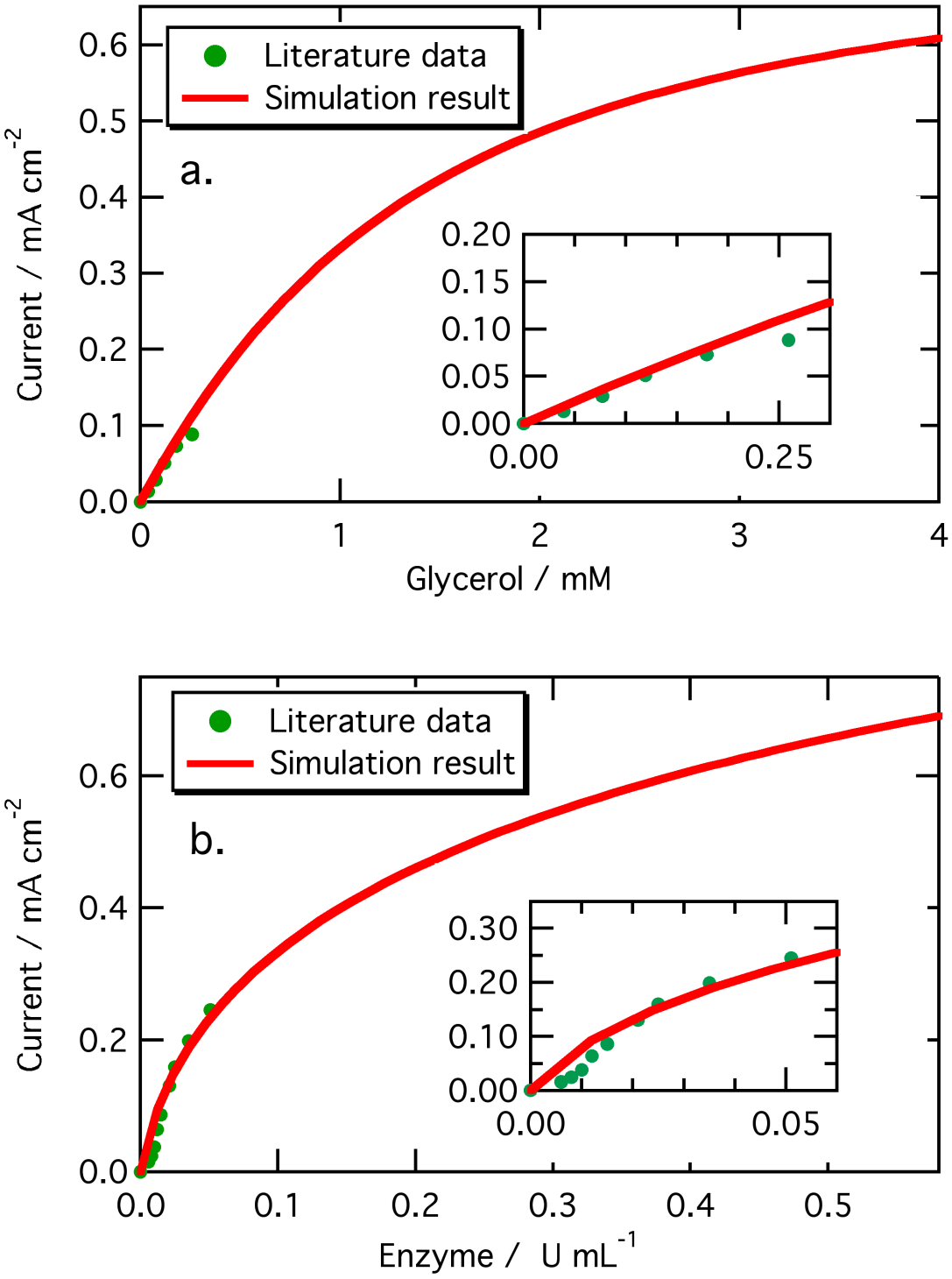

Figure 5.10 Simulation for biosensor performance a) glycerol concentration profiles; b) impact of enzyme concentration

In Figure 5.10a, the apparent Michaelis-Menten constant for glycerol concentration is 1.56 ± 0.02 mM. At low glycerol concentration region (<0.5 mM), a linear relationship exists, which can be used for glycerol detection. In Figure 5.11b, the apparent Michaelis-Menten constant for glycerol dehydrogenase concentration is 0.16 ± 0.01 U mL^{-1}. At very low enzyme concentration (<0.004 U mL^{-1}), it takes long time to achieve pseudo steady state (>1000 s). Thus, the detection limit 0.004 U mL^{-1} was reported.

5.5 Summary

A simplified two-step kinetic model was developed to describe the reactions in bioelectrocatalysis involving NADH electrochemical regeneration. Planar and porous structures are developed to describe and evaluate the correlations of kinetics and mass-transport in the bioreactor for glycerol oxidation. Key parameters involve diffusivity of cofactor/substrate, electrocatalytic activity and enzyme kinetics. This modeling work will help to identify the fundamental processes in bioelectrocatalysis, determine the rate-limiting steps and optimize performance.

6 Summary and future directions

Electrochemical interfaces for regeneration of enzyme cofactors were fabricated, characterized, and applied to a bioconversion system. Based on incorporation of azine electropolymers with commercially available carboxylated carbon nanotubes, these electrodes produce high reaction rate and high yield of bioactive cofactor. This research is part of a wider effort in bioelectronic conversion, using enzymes as catalysts instead of traditional metal-based-complexes.

In Chapter 2, high-rate NADH oxidizing interfaces were achieved by electrode modification. Two materials were used: carboxylated carbon nanotubes (CNT) that act as high surface-area material, and commercially available azine dyes that reduce the overpotential for NADH oxidation. The CNT layers demonstrate good nanoscale homogeneity via scanning electron microscopy (SEM) and have surface area that is proportional to CNT loading, as demonstrated by electrochemical capacitance measurements. At a loading of 0.85 mg cm^{-2} CNT, the active surface area was increased by more than 1000-fold compared to an unmodified electrode. Electrodeposition of poly(methylene green) (PMG) and poly(toluidine blue) (PTBO) on the carboxylated CNT-modified electrodes was achieved by cyclic voltammetry. PMG-CNT modified electrodes display higher activity than those modified by PTBO, especially at high NADH concentration and high overpotential. SEM imaging of PMG-CNT suggests conformal growth of PMG on CNT, which allows good interaction between the two materials. The PMG-CNT interface demonstrates 5.0 mA cm^{-2} current density for NADH oxidation at 50 mV vs. Ag|AgCl in 20 mM NADH solution. The kinetics of NADH electrocatalysis were analyzed using

a quantitative mass-transport-corrected model with NADH bulk concentration and applied potential as independent variables.

Following the successful incorporation of carboxylated carbon nanotubes and electropolymerized azines, in Chapter 3, this composite was applied to a carbon paper support in order to construct a high surface area electrode for bulk conversion of NADH to NAD^+. Electrochemical capacitance measurements on CNT-carbon paper indicate electrochemical properties similar to CNT-GC, including controllable high surface area and good reproducibility.

During NADH bulk oxidation, NADH is consumed in a batch reactor due to electrocatalysis as well as bulk decay. A mathematical model, calibrated by measurements of NADH oxidation at PMG-CNT-modified glassy carbon electrodes, was applied to describe the kinetics of NADH electrocatalysis. About 80% conversion of NADH was observed after 1 hour, suggesting a high conversion rate. Using this enzyme cycling assay, 93 ± 6 % and 87 ± 8 % yields were obtained for applied potential at 500 mV and 150 mV vs. Ag|AgCl respectively. This suggests that roughly 10% of oxidized NADH may be inactive due to dimerization or some other side byproduct, after accounting for self decay.

The high-rate property described in Chapter 2 and the confirmed bioactivity of generated product described in Chapter 3 demonstrates that PMG-CNT is a high-performance electrochemical oxidizing interface for cofactor regeneration. As engineers, we further explored two aspects: whether it is possible to further improve the performance, and application of this interface for bioelectronic conversion.

In Chapter 4, we present a novel approach to facilitate the above NADH electrocatalysis system. High-potential cyclic voltammetry was employed to electrochemically activate carbon material. Electroactivation yields carbon-oxygen functional groups, as suggested by literature and also confirmed by EDS analysis and capacitance measurements. The resulting electrodes not only demonstrate improved catalytic activity towards NADH oxidation via increased active sites and quinone/hydroquinine catalysis, but more importantly, allow direct electrostatic adsorption of azines. The electroactivated MG-*f*CNT electrode demonstrates 1.8-fold increase in NADH oxidation activity compared to electropolymerized-MG-*f*CNT, corresponding to increased electroactive species loading. Stability of these electrodes is good, with 65% activity retention after 4000 continuous cyclic voltammograms, comparable to PMG-*f*CNT. These findings demonstrate that adsorbing MG on carboxylated-CNT yields a significant improvement in NADH electrocatalysis.

Chapter 5 demonstrates applications of the cofactor regenerating electrode, using quantitative models for dihydroxyacetone (DHA) production from glycerol oxidation coupled with electrocatalysis. A two-step kinetic model was developed to describe the reactions in bioelectrocatalysis involving NADH electrochemical regeneration. The kinetics of the system can be simplified into two steps: the electrocatalytic regeneration of cofactor NADH/NAD^+ and the enzymatic reaction of substrate using dehydrogenase. Planar and porous interface structures are modeled to simulate, predict and evaluate the kinetics and diffusion for the bioelectronic interface. Nondimensional Damkohler numbers can provide useful approach to simulate, predict and evaluate the kinetics and diffusion in the bioelectrocatalytic system. Key parameters involve diffusivity of cofactor/substrate, electrocatalytic activity and enzyme kinetics. This modeling

work helps to identify the fundamental processes in bioelectrocatalysis, determine the rate-limiting steps and optimize performance.

The above work demonstrates the huge potential of NAD^+ regeneration for further application. Collaborative efforts between different areas of science and engineering are necessary to make dehydrogenase-based bioelectrocatalysis a viable route for advancement in chemical synthesis, energy generation and analyte detection. Recommendations for future directions mainly include further improvement of NAD(P)H electrocatalysis and the validation of bioelectrocatalysis for DHA and mannitol production

This work focuses on NADH electrooxidation, but the methodology described here can be applied to NAD^+ reduction. Further improvement of electrocatalysts could be achieved by optimizing the electropolymerization condition or electrochemical activation procedures. The experimental conditions in electropolymerization, such as supporting electrolyte, pH, the sweep rate and number of cycles, highly influence the properties of the formed polymer films. For example, the thickness of polymer films highly depends on the number of cycles in cyclic voltammetry. Thus, one can expect to control the properties of electrocatalysts by adjusting operation conditions in electropolymerization. The surface chemistry responsible for the enhancement of direct NADH oxidation without azine addition is facilitated by voltage cycling, and cyclic voltammetry-based activation could be optimized by a design of experiments approach to simultaneously optimize parameters such as the potential range, the sweep rate, and the number of cycles.

The approach described for glycerol oxidation simulation can be transferred to mannitol production from fructose using mannitol dehydrogenase. It would be very helpful to validate the model prediction by employing our high-performance cofactor-regenerating electrode, following the reactor design and conducting the bioelectrocatalysis for DHA production at anode and mannitol production at cathode.

Because of high cost, it is undesirable to feed enzymes or cofactors into a conversion process. Instead, it is preferable to immobilize these active species on the electrode surface. Surface immobilization can also help to maintain enzyme activity and improve stability. Cofactor immobilization allows easy access to the enzyme and avoids loss due to diffusion. Typical approaches to molecular immobilization include intermolecular linking by means of bifunctional or multifunction reagents, and entrapment into a polymer matrix or a semipermeable membrane. Novel synthetic cofactors synthesized by our collaborators offer a promising approach for cofactor immobilization.

In all, this dissertation describes fabrication and characterization methods for efficient cofactor generation intended for bioelectronic conversions. This interface is potentially applicable to high-performance bioconversion, bioenergy and biosensor systems involving NADH-dependent dehydrogenases.

APPENDIX

APPENDIX

A.1 Kinetic model

A.1.1 Reactor design for Glycerol oxidation based on NADH electrocatalysis

```
%% Section 1: Kinetics dimensional parameters

% constants

% NADH electrochemical oxidation

n = 2; % number of electrons
F = 96485; % faradic constant, C/mol
k1 = 26e-3; % rate constant in NADH oxidation study, A/cm2
Km1 = 3.3e-6; % adsorption coefficient in NADH electro-oxidation study,
mol/cm3
Ve = 0.5; % applied potential, V
U = 0.129; % half-wave potential, V
b = 0.070; % exponential coefficient, V
e = exp((Ve-U)/b)/(1+exp((Ve-U)/b)); % exponential factor, dimensionless

% Enzymatical reaction

% A: NAD; B: Glycerol; Q: NADH; P: DHA

KmA = 0.0082e-6; % Michaelis-Menten constant for NAD in glycerol oxidation,
mol/cm3
KmQ = 0.014e-6; % Michaelis-Menten constant for NADH in glycerol oxidation,
mol/cm3
KmB = 140e-6; % Michaelis-Menten constant for glycerol in glycerol oxidation,
mol/cm3
KmP = 13e-6; % Michaelis-Menten constant for DHA in glycerol oxidation,
mol/cm3
kcatf = 3.3; % forward reaction activity in glycerol oxidation, 1/s
kcatr = 7.85; % backward reaction activity in glycerol oxidation, 1/s
Kia = 0.023e-6; % enzyme affinity for NAD, mol/cm3
Kiq = 1.2e-8; % enzyme affinity for NADH, mol/cm3
Kib = 1.46e-2; % enzyme affinity for glycerol, mol/cm3
Kip = 11.1e-6; % enzyme affinity for DHA, mol/cm3

%% Section 2: Parameters for reactor design, which can be varied in
simulation.

% Baseline operating conditions

A0 = 1; % geometric electrode surface area; 0.0707 for glassy carbon, cm2
V = 10; % reactor volume, cm3
E0 = 1e-6; % enzyme concentration, mol/cm3
N0 = 10e-6; % cofactor loading, mol/cm3
G0 = 1e-6; % glycerol initial concentration, mol/cm3
```

```
DataN0 = logspace (-6.5, -5.5, 20); % cofactor loading, mol/cm3
time = zeros (size(DataN0)); % Time to consume 50% glycerol

for i=1:length(DataN0),
    N0 = DataN0(i);

%%  Section 3: Time constants

    tau1 = V*N0*n*F/A0/k1/e; % time constant for NADH electrocatalytic
oxidation, s
    tau2 = G0/kcatf/E0; % time constant for glycerol reduction, s

%% Section 3: Nondimensional parameters

    K = kcatf*E0*V*n*F/A0/k1/e; % one equilibrium constant for the two
reactions
    M = tau1/tau2; % the ratio of two time constant

%% Section 4: Time constant calculation

    [tau, out] = GlyReactormyd (A0, V, N0, E0, G0);
    time(i) = tau;

end

%% Section 5: Figures

DataN0= DataN0*1e6; % convert unit to mM

figure,plot(DataN0, time, '-o');
xlabel('NAD loading (mM)')
ylabel('Time constant (hr)')
```

A.1.2 Conversions in bioelectrocatalysis

```
function [tau, out] = GlyReactormyd (A0, V, N0, E0, G0)

%% Reactor design input
%A0; % electrode surface area, cm2;
%V; % volume of the reactor, cm3;
%N0; % cofactor loading, mol/cm3;
%E0;% enzyme concentration, mol/cm3;
%G0; % initial gly concentration, mol/cm3;

%% Parameters

% NADH Electrochemical reaction

n = 2; % number of electrons
F = 96485; % faradic constant, C/mol
k1 = 26e-3; % rate constant in NADH oxidation study, A/cm2
```

```
Km1 = 3.3e-6; % adsorption coefficient in NADH electro-oxidation study,
mol/cm3
Ve = 0.5; % applied potential, V
U = 0.129; % half-wave potential, V
b = 0.070; % exponential coefficient, V
e = exp((Ve-U)/b)/(1+exp((Ve-U)/b)); % exponential factor, dimensionless

% Enzymatical reaction

KmA = 0.0082e-6; % Michaelis-Menten constant for NAD in glycerol oxidation,
mol/cm3
KmQ = 0.014e-6; % Michaelis-Menten constant for NADH in glycerol oxidation,
mol/cm3
KmB = 140e-6; % Michaelis-Menten constant for glycerol in glycerol oxidation,
mol/cm3
KmP = 13e-6; % Michaelis-Menten constant for DHA in glycerol oxidation,
mol/cm3
kcatf = 3.3; % forward reaction activity in glycerol oxidation, 1/s
kcatr = 7.85; % backward reaction activity in glycerol oxidation, 1/s
Kia = 0.023e-6; % enzyme affinity for NAD, mol/cm3
Kiq = 1.2e-8; % enzyme affinity for NADH, mol/cm3
Kib = 1.46e-2; % enzyme affinity for glycerol, mol/cm3
Kip = 11.1e-6; % enzyme affinity for DHA, mol/cm3
Keq = kcatf*Kiq*KmP/kcatr/Kia/KmB; % equilibrium constant in enzymatical
reaction, dimensionless

%% Set Ode 45 calculation

% set calculation options

options = odeset('InitialStep',1,'MaxStep',1);

% ode 45

[t,y] = ode45(@deq,[0 36000],[0 N0 G0 0],options);

% y(:1): NADH concentration (Q)
% y(:2): NAD concentration (A)
% y(:3): Glycerol concentration (B)
% y(:4): DHA (P)

out.profileA = 1e6*y(:,1); % NADH concentration profile
out.profileB =1e6*y(:,2); % NAD concentration profile
out.glycerol = 1e6*y(:,3); % glycerol concentration profile
out.current = e*1e3*(k1*y(:,1))./(Km1+y(:,1)); % current density profile

%% Plots

% In the whole time range

out.time=t/3600; % convert time constant to unit hour

tau = out.time ( find( out.glycerol < 0.5, 1, 'first' )); % Time to consume
50% glycerol
```

```
figure,subplot(2,2,1);semilogy(out.time,out.profileA,t,out.profileB)
legend('NADH concentration profile','NAD concentration profile')
xlabel('time (hr)')
ylabel('Concentration (mM)')

subplot(2,2,2);plot(out.time, out.current);
legend('current density-time profile','Location','west');
xlabel('time (hr)')
ylabel('Current density (mA/cm2)')

subplot(2,2,4);plot(out.time, out.glycerol)
legend('Glycerol concentration profile')
xlabel('time (hr)')
ylabel('Concentration (mM)')

%% ODE 45 calculation

 function dydx=deq(t,y)

% y(:1): NADH concentration (Q)
% y(:2): NAD concentration (A)
% y(:3): Glycerol concentration (B)
% y(:4): DHA (P)

     Q = y(1);
     A = y(2);
     B = y(3);
     P = y(4);

     r1 = e*k1*A0*(Q/(Km1+Q))/n/F/V;% electrochemical reaction
     r2 = kcatf*kcatr*E0*(A*B - P*Q/Keq)/(kcatr*Kia*KmB + kcatr*KmB*A +
kcatr*KmA*B + kcatf*KmQ*P/Keq + kcatf*KmP*Q/Keq + kcatr*A*B +
kcatf*KmQ*A*P/Keq/Kia + kcatf*P*Q/Keq + kcatr*KmA*B*Q/Kiq + kcatr*A*B*P/Kip +
kcatf*B*P*Q/Kib/Keq);


    dydx = [-r1+r2;
            r1-r2;
            -r2;
            r2];

 end % deq

end
```

A.2 Kinetics-mass transport model

A.2.1 Planar model

```
function out=ndrGly1
%% Parameters

% Kinetics-transport model for planar interface

 %% Parameters

% Bioreactor set-up

L = 10e-4; % film thickness, cm
N0 = 10e-6; % initial NAD concentration, mol/cm3;
E = 100e-7;% enzyme concentration, mol/cm3;
G0 = 1e-6; % glycerol bulk concentration, mol/cm3;

% Parameters in NADH electrocatalysis

n = 2; % Number of electrons
F = 96485; % Faradic constant, C/mol
jmax = 26e-3; % rate constant in NADH oxidation study, A/cm2
S =1; % electrode geometric surface area, cm2
S2 = 1; % specific surface area ratio, under baseline conditions, S2=1
k1 = S*S2*jmax/n/F/S; % electrochemical reaction rate, mol/s
Km1 = 3.3e-6; % adsorption coefficient in NADH electro-oxidation study,
mol/cm3
Ve = 0.4; % applied potential, V
U = 0.129; % half-wave potential, V
b = 0.070; % exponential coefficient, V

% Parameters in enzyme reaction

% NADH concentration (Q)
% NAD concentration (A)
% Glycerol concentration (B)
% DHA concentration (P)

KmA = 0.0082e-6; % Michaelis-Menten constant for NAD in enzyme reaction,
mol/cm3
KmQ = 0.014e-6; % Michaelis-Menten constant for NADH in enzyme reaction,
mol/cm3
KmB = 140e-6; % Michaelis-Menten constant for glycerol in enzyme reaction,
mol/cm3
KmP = 13e-6; % Michaelis-Menten constant for DHA in enzyme reaction, mol/cm3
kcatf = 3.3; % forward enzyme reaction activity, 1/s
kcatr = 7.85; % backward enzyme reaction activity, 1/s
Kia = 0.023e-6; % enzyme affinity for NAD, mol/cm3
Kiq = 1.2e-8; % enzyme affinity for NADH, mol/cm3
Kib = 1.46e-2; % enzyme affinity for glycerol, mol/cm3
Kip = 11.1e-6; % enzyme affinity for DHA, mol/cm3
```

```
Keq = kcatf*Kiq*KmP/kcatr/Kia/KmB; % equilibrium constant in glycerol
reaction, dimensionless

% Diffusivities

Dnh = 3.3e-8; % diffusivity of NADH/NAD, cm2/s
Dg = 2.9e-7; %diffusivity of glycerol/DHA, cm2/s

%% Nondimensional parameters

% Normalize parameter in electrochemical reaction using cofactor loading

sigNh = Km1/N0;

% Normalize parameters in enzyme kinetics using cofactor loading and
substrate concentration

sigA = KmA/N0;
sigB = KmB/G0;
sigQ = KmQ/N0;
sigP = KmP/G0;
alfa = Kia/N0;
alfb = Kib/G0;
alfq = Kiq/N0;
alfp = Kip/G0;

fr = kcatf/kcatr;

eps = Dnh*N0/Dg/G0; % diffusivity ratio

% Damkohler numbers, reaction rate to diffusion rate

Da_nh = k1*L*exp((Ve-U)/b)/(1+exp((Ve-U)/b))/Dg/G0; % Damkohler number for
NADH, in electrochemical reaction
Da_gly = kcatf*E*L*L/Dg/G0;% Damkohler number for glycerol, in enzyme
reaction

%% output Damkohler numbers

out.Da_nh = Da_nh;
out.Da_gly = Da_gly;

%% BVP4c

% Generate an initial guess
x = linspace(0,1,1000);
solinit = bvpinit(x,[1 0 0.5 0]);

% x: film thickness
% y(1): NADH concentration
% y(2): NADH flux
% y(3): Glycerol concentration
% y(4): Glycerol flux
```

```
% call bvp4c

sol = bvp4c(@projectode,@projectbc,solinit);

% output concentration and reaction rate profiles from solution

out.x = (sol.x)'; % film thickness
out.a = (1-sol.y(1,:))'; % NAD concentration
out.s = sol.y(3,:)'; % glycerol concentration
out.q = 1-out.a; % NADH concentration
out.p = 1-out.s; % DHA concentration

r2 = sol.y(4,:);
rg = trapz(out.x, r2);
out.R = rg*Dg*G0/L/L; % dimensional enzyme reaction rate, mol/s/cm3

% Figures

figure, subplot(2,1,1);plot(out.x,[out.a, out.q])
xlabel('nondimensional thickness')
ylabel('nondimensional concentration')
legend('NAD','NADH','Location','Southeast')

subplot(2,1,2);plot(out.x,[out.s, out.p])
xlabel('nondimensional thickness')
legend('Glycerol','DHA','Location','Southeast')

    function dydx = projectode(x,y)

    Q = y(1);
    A = 1-y(1);
    B = y(3);
    P = 1-y(3);

    r2 = Da_gly * (A*B - P*Q/Keq)/(alfa*sigB + sigB*A + sigA*B +
fr*sigQ*P/Keq + fr*sigP*Q/Keq + A*B + fr*sigQ*A*P/Keq/alfa + fr*P*Q/Keq +
fr*sigA*B*Q/alfq + A*B*P/alfp +
fr*B*P*Q/alfb/Keq)*(A>0)*(y(3)>0)*(y(1)>0)*(A<1)*(B<1); % enzyme reaction


    dydx = [y(2)
            -r2/eps*(Q>0)*(B>0)*(A>0)*(A<1)*(B<1)
            y(4)
            r2*(Q>0)*(B>0)*(A>0)*(A<1)*(B<1)];

    end %dydx

        function res=projectbc(y0,y1)

        % Boundary conditions

        r1 = Da_nh/eps*(y0(1)/(sigNh+y0(1)));% electrochemical reaction
```

```
        res = [y0(2)-r1
               y0(4)
               y1(2)
               y1(3)-1];


        end % bc

end
```

A.2.2 Porous-Mobile model (porous electrode with cofactor fed into reactor)

```
function out=ndrGly2

% A Kinetics-transport model for porous electrode.
% In this model, enzyme is immobilized whereas cofactor is mobile.

 %% Parameters

% Bioreactor set-up

L = 10e-4; % film thickness, cm
N0 = 10e-6; % initial NAD concentration, mol/cm3;
E = 1e-7;% enzyme concentration, mol/cm3;
G0 = 1e-6; % glycerol bulk concentration, mol/cm3;

% Parameters in NADH electrocatalysis

n = 2; % Number of electrons
F = 96485; % Faradic constant, C/mol
jmax = 26e-3; % rate constant in NADH oxidation study, A/cm2
S =1; % electrode geometric surface area, cm2
S2 = 1; % specific surface area ratio, under baseline conditions, S2=1
k1 = S*S2*jmax/n/F/S; % electrochemical reaction rate, mol/s
Km1 = 3.3e-6; % adsorption coefficient in NADH electro-oxidation study,
mol/cm3
Ve = 0.4; % applied potential, V
U = 0.129; % half-wave potential, V
b = 0.070; % exponential coefficient, V

% Parameters in enzyme reaction

% NADH concentration (Q)
% NAD concentration (A)
% Glycerol concentration (B)
% DHA concentration (P)

KmA = 0.0082e-6; % Michaelis-Menten constant for NAD in enzyme reaction,
mol/cm3
```

```
KmQ = 0.014e-6; % Michaelis-Menten constant for NADH in enzyme reaction,
mol/cm3
KmB = 140e-6; % Michaelis-Menten constant for glycerol in enzyme reaction,
mol/cm3
KmP = 13e-6; % Michaelis-Menten constant for DHA in enzyme reaction, mol/cm3
kcatf = 3.3; % forward enzyme reaction activity, 1/s
kcatr = 7.85; % backward enzyme reaction activity, 1/s
Kia = 0.023e-6; % enzyme affinity for NAD, mol/cm3
Kiq = 1.2e-8; % enzyme affinity for NADH, mol/cm3
Kib = 1.46e-2; % enzyme affinity for glycerol, mol/cm3
Kip = 11.1e-6; % enzyme affinity for DHA, mol/cm3
Keq = kcatf*Kiq*KmP/kcatr/Kia/KmB; % equilibrium constant in glycerol
reaction, dimensionless

% Diffusivities

Dnh = 3.3e-8; % diffusivity of NADH/NAD, cm2/s
Dg = 2.9e-7; %diffusivity of glycerol, cm2/s

%% Nondimensional parameters

% Normalize parameter in electrochemical reaction using cofactor loading

sigNh = Km1/N0;

% Normalize parameters in enzyme kinetics using cofactor loading and
substrate concentration

sigA = KmA/N0;
sigB = KmB/G0;
sigQ = KmQ/N0;
sigP = KmP/G0;
alfa = Kia/N0;
alfb = Kib/G0;
alfq = Kiq/N0;
alfp = Kip/G0;

fr = kcatf/kcatr;

eps = Dnh*N0/Dg/G0; % diffusivity ratio

% Damkohler numbers, reaction rate to diffusion rate

Da_nh = k1*L*exp((Ve-U)/b)/(1+exp((Ve-U)/b))/Dg/G0; % Damkohler number for
NADH, in electrochemical reaction
Da_gly = kcatf*E*L*L/Dg/G0;% Damkohler number for glycerol, in enzyme
reaction

%% output Damkohler numbers

out.Da_nh = Da_nh;
out.Da_gly = Da_gly;

%% BVP4c
```

```
% Generate an intitial guess
x = linspace(0,1,1000);
solinit = bvpinit(x,[1 0 0.5 0]);

% x: film thickness
% y(1): NAD concentration
% y(2): NAD gradient rate
% y(3): Glycerol concentration
% y(4): Glycerol gradient rate

% call bvp4c

sol = bvp4c(@projectode,@projectbc,solinit);

% output concentration and reaction rate profiles from solution

out.x = (sol.x)'; % film thickness
out.a = sol.y(1,:)'; % NAD concentration
out.q = 1-out.a; % NADH concentration
out.b = sol.y(3,:)'; % Glycerol concentration
out.p = 1-out.b; % DHA concentration

r2 = sol.y(4,:);
rg = trapz(out.x, r2);
out.R = rg*Dg*G0/L/L; % dimensional enzyme reaction rate, mol/s/cm3

% Figures

figure, subplot(2,1,1);plot(out.x,[out.a, out.q])
xlabel('nondimensional thickness')
ylabel('nondimensional concentration')
legend('NAD','NADH','Location','Southeast')

subplot(2,1,2);plot(out.x,[out.b, out.p])
xlabel('nondimensional thickness')
legend('Glycerol','DHA','Location','Southeast')

    function dydx = projectode(x,y)

    A = y(1);
    B = y(3);
    Q = 1-y(1);
    P = 1-y(3);

    r1 = Da_nh/eps*(Q/(sigNh+Q));
    r2 = Da_gly*(A*B - P*Q/Keq)/(alfa*sigB + sigB*A + sigA*B + fr*sigQ*P/Keq
+ fr*sigP*Q/Keq + A*B + fr*sigQ*A*P/Keq/alfa + fr*P*Q/Keq + fr*sigA*B*Q/alfq
+ A*B*P/alfp + fr*B*P*Q/alfb/Keq)*(A>0)*(y(3)>0)*(y(1)>0);

    dydx = [y(2)*(A>0)*(B<1)
            (r2/eps-r1)*(A>0)*(B>0)*(B<1)
            y(4)*(A>0)*(B<1)
            r2*(A>0)*(B>0)*(B<1)];
```

```
    end %dydx


    function res=projectbc(y0,y1)

    res = [y0(2)
           y0(4)
           y1(1)-1
           y1(3)-1];


    end % bc

end
```

A.2.3 Porous-entrapped Model (Porous electrode with cofactor entrapped)

```
function out=ndrGly3

% A Kinetics-transport model for porous electrode.
%In this model, both enzyme and cofactor are entrapped in the film.


%% Parameters

% Bioreactor set-up
L = 10e-4; % film thickness, cm
N0 = 10e-6; % initial NAD concentration, mol/cm3;
E = 1e-7;% enzyme concentration, mol/cm3;
G0 = 1e-6; % glycerol bulk concentration, mol/cm3;

% Parameters in NADH electrocatalysis
n = 2; % Number of electrons
F = 96485; % Faradic constant, C/mol
jmax = 26e-3; % rate constant in NADH oxidation study, A/cm2
S =1; % electrode geometric surface area, cm2
S2 = 1; % specific surface area ratio, under baseline conditions, S2=1
k1 = S*S2*jmax/n/F; % electrochemical reaction rate, mol/s
Km1 = 3.3e-6; % adsorption coefficient in NADH electro-oxidation study,
mol/cm3
Ve = 0.4; % applied potential, V
U = 0.129; % half-wave potential, V
b = 0.070; % exponential coefficient, V

% Parameters in enzyme reaction

% NADH concentration (Q)
% NAD concentration (A)
% Glycerol concentration (B)
```

```
% DHA concentration (P)

KmA = 0.0082e-6; % Michaelis-Menten constant for NAD in enzyme reaction,
mol/cm3
KmQ = 0.014e-6; % Michaelis-Menten constant for NADH in enzyme reaction,
mol/cm3
KmB = 140e-6; % Michaelis-Menten constant for glycerol in enzyme reaction,
mol/cm3
KmP = 13e-6; % Michaelis-Menten constant for DHA in enzyme reaction, mol/cm3
kcatf = 3.3; % forward enzyme reaction activity, 1/s
kcatr = 7.85; % backward enzyme reaction activity, 1/s
Kia = 0.023e-6; % enzyme affinity for NAD, mol/cm3
Kiq = 1.2e-8; % enzyme affinity for NADH, mol/cm3
Kib = 1.46e-2; % enzyme affinity for glycerol, mol/cm3
Kip = 11.1e-6; % enzyme affinity for DHA, mol/cm3
Keq = kcatf*Kiq*KmP/kcatr/Kia/KmB; % equilibrium constant in malate reaction,
dimensionless

% Diffusivities

Dnh = 3.3e-8; % diffusivity of NADH/NAD, cm2/s
Dg = 2.9e-7; %diffusivity of glycerol, cm2/s

%% Nondimensional parameters

% Normalize parameter in electrochemical reaction using cofactor loading

sigNh = Km1/N0;

% Normalize parameters in enzyme kinetics using cofactor loading and
substrate concentration

sigA = KmA/N0;
sigB = KmB/G0;
sigQ = KmQ/N0;
sigP = KmP/G0;
alfa = Kia/N0;
alfb = Kib/G0;
alfq = Kiq/N0;
alfp = Kip/G0;

fr = kcatf/kcatr;

eps = Dnh*N0/Dg/G0; % diffusivity ratio

% Damkohler numbers, reaction rate to diffusion rate

Da_nh = k1/S*L*exp((Ve-U)/b)/(1+exp((Ve-U)/b))/Dg/G0; % Damkohler number for
NADH, in electrochemical reaction
Da_gly = kcatf*E*L*L/Dg/G0;% Damkohler number for glycerol, in enzyme
reaction

%% output Damkohler numbers
```

```
out.Da_nh = Da_nh;
out.Da_gly = Da_gly;

%% BVP4c

% Generate an intitial guess
x = linspace(0,1,1000);
solinit = bvpinit(x,[1 0 0.5 0]);

% x: film thickness
% y(1): NADH concentration
% y(2): NADH gradient rate
% y(3): Glycerol concentration
% y(4): Glycerol gradient rate

% call bvp4c

sol = bvp4c(@projectode,@projectbc,solinit);

% output concentration and reaction rate profiles from solution
out.x = (sol.x)'; % film thickness
out.a = sol.y(1,:)'; % NAD concentration
out.q = 1-out.a; % NADH concentration
out.b = sol.y(3,:)'; % Glycerol concentration
out.p = 1-out.b; % DHA concentration

r1 = out.q/(sigNh + out.q); % electrochemical reaction rate
r1m = max(r1);
r2 = sol.y(4,:)'; % enzymatic reaction rate
r2m = max(r2);

out.r1 = r1/r1m;
out.r2 = r2/r2m;

re = trapz(out.x, r1); % integration of electrochemical reaction rate along
the film thickness
rg = trapz(out.x, r2); % integration of enzyme reaction rate along the film
thickness

out.j = re*n*F*Dnh*N0/L; % dimensional electrochemical reaction rate, A/cm2
out.R = rg*Dg*G0/L/L; % dimensional enzyme reaction rate, mol/s/cm3

% Figures

figure, subplot(2,1,1);plot(out.x,[out.a, out.q])
xlabel('nondimensional thickness')
legend('NAD','NADH','Location','Southeast')

subplot(2,1,2);plot(out.x,[out.b, out.p])
xlabel('nondimensional thickness')
legend('Glycerol', 'DHA','Location','Southeast')

    function dydx = projectode(x,y)
```

```
    % y(1): NAD concentration
    % y(2): NAD gradient rate
    % y(3): Glycerol concentration
    % y(4): Glycerol gradient rate

    A = y(1);
    Q = 1-y(1);
    B = y(3);
    P = 1-y(3);

    r1 = Da_nh/eps*(Q/(sigNh+Q));
    r2 = Da_gly*(A*B - P*Q/Keq)/(alfa*sigB + sigB*A + sigA*B + fr*sigQ*P/Keq
+ fr*sigP*Q/Keq + A*B + fr*sigQ*A*P/Keq/alfa + fr*P*Q/Keq + fr*sigA*B*Q/alfq
+ A*B*P/alfp + fr*B*P*Q/alfb/Keq)*(A>0)*(y(3)>0)*(y(1)>0);

    dydx = [y(2)*(A>0)*(B<1)
            (r2/eps-r1)*(A>0)*(B>0)*(B<1)
            y(4)*(A>0)*(B<1)
            r2*(A>0)*(B>0)*(B<1)];

    end %dydx

    function res=projectbc(y0,y1)

        % BCs

        res = [y0(2)
               y0(4)
               y1(2)
               y1(3)-1];


    end % bc

end
```

A.3 Model validation

```
%% Simulation for Glycerol oxidation based on NADH electrocatalysis

% Kinetics model
% Hanzi Li and Scott Calabrese Barton, 2013

%% Section 1: Kinetics dimensional parameters

% constants

% NADH electrochemical oxidation

n = 2; % number of electrons
F = 96485; % faradic constant, C/mol
k1 = 2e-3; % rate constant in NADH oxidation study, A/cm2
Km1 = 2.6e-6; % adsorption coefficient in NADH electro-oxidation study,
```

```
mol/cm3
Ve = 0.55; % applied potential, V
U = 0.191; % half-wave potential, V
b = 0.101; % exponential coefficient, V
e = exp((Ve-U)/b)/(1+exp((Ve-U)/b)); % exponential factor, dimensionless

% Enzymatical reaction

% A: NAD; B: Glycerol; Q: NADH; P: DHA

KmA = 0.0082e-6; % Michaelis-Menten constant for NAD in glycerol oxidation,
mol/cm3
KmQ = 0.014e-6; % Michaelis-Menten constant for NADH in glycerol oxidation,
mol/cm3
KmB = 25.7e-6; % Michaelis-Menten constant for glycerol in glycerol oxidation,
mol/cm3
KmP = 13e-6; % Michaelis-Menten constant for DHA in glycerol oxidation,
mol/cm3
kcatf = 121; % forward reaction activity in glycerol oxidation, 1/s
kcatr = 7.85; % backward reaction activity in glycerol oxidation, 1/s
Kia = 0.023e-6; % enzyme affinity for NAD, mol/cm3
Kiq = 0.028e-6; % enzyme affinity for NADH, mol/cm3
Kib = 1.46e-2; % enzyme affinity for glycerol, mol/cm3
Kip = 0.064e-6; % enzyme affinity for DHA, mol/cm3
Keq = kcatf*Kiq*KmP/kcatr/Kia/KmB; % equilibrium constant in enzymatical
reaction, dimensionless

%% Section 2: Parameters for reactor design, which can be varied in
simulation.

% Baseline operating conditions

A0 = 4.53e-4; % geometric electrode surface area; 0.0707 for glassy carbon,
cm2
V = 4; % reactor volume, cm3
E0 = 3.67e-9; % enzyme concentration, mol/cm3
N0 = 2e-6; % cofactor loading, mol/cm3
G0 = 1e-6; % glycerol initial concentration, mol/cm3

DataG0 = linspace (0, 4e-6, 20); % cofactor loading, mol/cm3
Sensor = zeros (size(DataG0)); % Detected current

for i=1:length(DataG0),
    G0 = DataG0(i);

%%  Section 3: Time constants

    tau1 = V*N0*n*F/A0/k1/e; % time constant for NADH electrocatalytic
oxidation, s
    tau2 = G0/kcatf/E0; % time constant for glycerol reduction, s

%% Section 3: Nondimensional parameters

    K = kcatf*E0*V*n*F/A0/k1/e; % one equilibrium constant for the two
```

```
reactions
    M = tau1/tau2; % the ratio of two time constant

%% Section 4: Time constant calculation

    [current, out] = GlyReactorW (A0, V, N0, E0, G0);
    Sensor(i) = current;

end

%% Section 5: Figures

DataG0= DataG0'*1e6; % convert unit to mM
Sensor=Sensor';

figure,plot(DataG0, Sensor, '-o');
xlabel('Glycerol (mM)')
ylabel('Current (uA)')


function [current, out] = GlyReactorW (A0, V, N0, E0, G0)

%% Reactor design input
%A0; % electrode surface area, cm2;
%V; % volume of the reactor, cm3;
%N0; % cofactor loading, mol/cm3;
%E0;% enzyme concentration, mol/cm3;
%G0; % initial gly concentration, mol/cm3;

%% Parameters

% NADH Electrochemical reaction

n = 2; % number of electrons
F = 96485; % faradic constant, C/mol
k1 = 2e-3; % rate constant in NADH oxidation study, A/cm2
Km1 = 2.6e-6; % adsorption coefficient in NADH electro-oxidation study,
mol/cm3
Ve = 0.55; % applied potential, V
U = 0.191; % half-wave potential, V
b = 0.101; % exponential coefficient, V
e = exp((Ve-U)/b)/(1+exp((Ve-U)/b)); % exponential factor, dimensionless

% Enzymatical reaction

KmA = 0.0082e-6; % Michaelis-Menten constant for NAD in glycerol oxidation,
mol/cm3
KmQ = 0.014e-6; % Michaelis-Menten constant for NADH in glycerol oxidation,
mol/cm3
KmB = 25.7e-6; % Michaelis-Menten constant for glycerol in glycerol oxidation,
mol/cm3
KmP = 13e-6; % Michaelis-Menten constant for DHA in glycerol oxidation,
mol/cm3
kcatf = 121; % forward reaction activity in glycerol oxidation, 1/s
```

```
kcatr = 7.85; % backward reaction activity in glycerol oxidation, 1/s
Kia = 0.023e-6; % enzyme affinity for NAD, mol/cm3
Kiq = 0.028e-6; % enzyme affinity for NADH, mol/cm3
Kib = 1.46e-2; % enzyme affinity for glycerol, mol/cm3
Kip = 0.064e-6; % enzyme affinity for DHA, mol/cm3
Keq = kcatf*Kiq*KmP/kcatr/Kia/KmB; % equilibrium constant in enzymatical
reaction, dimensionless

%% Set Ode 45 calculation

% set calculation options

options = odeset('InitialStep',1,'MaxStep',1);

% ode 45

[t,y] = ode45(@deq,[0 3600],[0 N0 G0 0],options);

% y(:1): NADH concentration (Q)
% y(:2): NAD concentration (A)
% y(:3): Glycerol concentration (B)
% y(:4): DHA (P)

out.profileA = 1e6*y(:,1); % NADH concentration profile
out.profileB =1e6*y(:,2); % NAD concentration profile
out.glycerol = 1e6*y(:,3); % glycerol concentration profile
out.current = e*1e6*(k1*y(:,1))./(Km1+y(:,1))*A0; % current in uA

current = out.current (find (t > 60, 1, 'first'));

%% Plots

% In the whole time range

out.time=t; % convert time constant to unit hour

% figure,subplot(2,2,1);semilogy(out.time,out.profileA,t,out.profileB)
% legend('NADH concentration profile','NAD concentration profile')
% xlabel('time (s)')
% ylabel('Concentration (mM)')
%
% subplot(2,2,2);plot(out.time, out.current);
% legend('current -time profile','Location','west');
% xlabel('time (s)')
% ylabel('Current density (uA)')
%
% subplot(2,2,4);plot(out.time, out.glycerol)
% legend('Glycerol concentration profile')
% xlabel('time (s)')
% ylabel('Concentration (mM)')

%% ODE 45 calculation

 function dydx=deq(t,y)
```

```
% y(:1): NADH concentration (Q)
% y(:2): NAD concentration (A)
% y(:3): Glycerol concentration (B)
% y(:4): DHA (P)

     Q = y(1);
     A = y(2);
     B = y(3);
     P = y(4);

     r1 = e*k1*A0*(Q/(Km1+Q))/n/F/V;% electrochemical reaction
     r2 = kcatf*kcatr*E0*(A*B - P*Q/Keq)/(kcatr*Kia*KmB + kcatr*KmB*A +
kcatr*KmA*B + kcatf*KmQ*P/Keq + kcatf*KmP*Q/Keq + kcatr*A*B +
kcatf*KmQ*A*P/Keq/Kia + kcatf*P*Q/Keq + kcatr*KmA*B*Q/Kiq + kcatr*A*B*P/Kip +
kcatf*B*P*Q/Kib/Keq);


    dydx = [-r1+r2;
            r1-r2;
            -r2;
            r2];

 end % deq

end
```

REFERENCES

REFERENCES

1. G. A. Strohmeier, H. Pichler, O. May and M. Gruber-Khadjawi, "Application of designed enzymes in organic synthesis," *Chemical Reviews,* **111**(7), 4141-4164 (2011).

2. S. Fogler, *Elements of chemical reaction engineering (4th edition),* vol. (Prentice Hall, 2005).

3. U. T. Bornscheuer, G. W. Huisman, R. J. Kazlauskas, S. Lutz, J. C. Moore and K. Robins, "Engineering the third wave of biocatalysis," *Nature,* **485**(7397), 185-194 (2012).

4. F. H. Arnold, "Combinatorial and computational challenges for biocatalyst design," *Nature,* **409**(6817), 253-257 (2001).

5. A. Schmid, J. S. Dordick, B. Hauer, A. Kiener, M. Wubbolts and B. Witholt, "Industrial biocatalysis today and tomorrow," *Nature,* **409**(6817), 258-268 (2001).

6. J. D. Rozzell, "Commercial scale biocatalysis: Myths and realities," *Bioorganic & Medicinal Chemistry,* **7**(10), 2253-2261 (1999).

7. D. Voet, J. G. Voet and C. W. Pratt, *Fundamentals of biochemistry,* vol. (Wiley, New York, 2002).

8. S. C. Barton, J. Gallaway and P. Atanassov, "Enzymatic biofuel cells for implantable and microscale devices," *Chemical Reviews,* **104**(10), 4867-4886 (2004).

9. N. S. Hudak, *Mediated biocatalytic cathodes for fuel cells*, 3249093, Columbia University (2007).

10. S. Wenda, S. Illner, A. Mell and U. Kragl, "Industrial biotechnology-the future of green chemistry?," *Green Chemistry,* **13**(11), 3007-3047 (2011).

11. E. Simon and P. N. Bartlett, "Modified electrodes for the oxidation of nadh," *Surfactant Science Series,* **111**(Biomolecular Films), 499-544 (2003).

12. X. Zhao, *Intensified biocatalysis for production of fuel and chemicals from lipids*, Ph.D., University of Minnesota (2010).

13. S. A. Kumar and S. M. Chen, "Electroanalysis of nadh using conducting and redox active polymer/carbon nanotubes modified electrodes - a review," *Sensors,* **8**(2), 739-766 (2008).

14. A. A. Karyakin, E. E. Karyakina, W. Schuhmann and H. L. Schmidt, "Electropolymerized azines: Part ii. In a search of the best electrocatalyst of nadh oxidation," *Electroanalysis,* **11**(8), 553-557 (1999).

15. "Sigma-aldrich product catalog," http://www.sigmaaldrich.com/catalog/product/sial/n7004?lang=en&region=US, accessed January 16, 2013.

16. H. Chenault and G. Whitesides, "Regeneration of nicotinamide cofactors for use in organic synthesis," *Applied Biochemistry and Biotechnology,* **14**(2), 147-197 (1987).

17. W. F. Liu and P. Wang, "Cofactor regeneration for sustainable enzymatic biosynthesis," *Biotechnology Advances,* **25**(4), 369-384 (2007).

18. R. Wichmann and D. Vasic-Racki, "Cofactor regeneration at the lab scale," in *Technology transfer in biotechnology,* 225-260 (2005).

19. F. Hollmann, I. Arends and K. Buehler, "Biocatalytic redox reactions for organic synthesis: Nonconventional regeneration methods," *Chemcatchem,* **2**(7), 762-782 (2010).

20. Y. H. Kim and Y. J. Yoo, "Regeneration of the nicotinamide cofactor using a mediator-free electrochemical method with a tin oxide electrode," *Enzyme and Microbial Technology,* **44**(3), 129-134 (2009).

21. C. Kohlmann, W. Markle and S. Lutz, "Electroenzymatic synthesis," *Journal of Molecular Catalysis B-Enzymatic,* **51**(3-4), 57-72 (2008).

22. S. K. Yoon, E. R. Choban, C. Kane, T. Tzedakis and P. J. A. Kenis, "Laminar flow-based electrochemical microreactor for efficient regeneration of nicotinamide cofactors for biocatalysis," *Journal of the American Chemical Society,* **127**(30), 10466-10467 (2005).

23. K. Delecouls-Servat, A. Bergel and R. Basseguy, "Membrane electrochemical reactors (mer) for nadh regeneration in hladh-catalysed synthesis: Comparison of effectiveness," *Bioprocess and Biosystems Engineering,* **26**(4), 205-215 (2004).

24. L. Gorton and E. Dominguez, "Electrochemistry of nad(p)$^+$/nad(p)h," in *Encyclopedia of electrochemistry,* vol. 9 (eds. Bard, A. J., Stratmann, M. & Wilson, G. S.), 67-143 (Wiley, New York, 2002).

25. W. M. Haynes, "Crc handbook of chemistry and physics," (ed. Haynes, W. M.), (CRC Press, 2010).

26. I. Katakis and E. Dominguez, "Catalytic electrooxidation of nadh for dehydrogenase amperometric biosensors," *Mikrochimica Acta,* **126**(1-2), 11-32 (1997).

27. P. N. Bartlett, E. Simon and C. S. Toh, "Modified electrodes for nadh oxidation and dehydrogenase-based biosensors," in 117-122, (Elsevier Science Sa, 2002).

28. C. M. Halliwell, E. Simon, C. S. Toh, P. N. Bartlett and A. E. G. Cass, "Immobilisation of lactate dehydrogenase on poly(aniline)-poly(acrylate) and poly(aniline)-poly-(vinyl sulphonate) films for use in a lactate biosensor," *Analytica Chimica Acta,* **453**(2), 191-200 (2002).

29. G. T. R. Palmore, H. Bertschy, S. H. Bergens and G. M. Whitesides, "A methanol/dioxygen biofuel cell that uses nad$^+$-dependent dehydrogenases as catalysts: Application of an electro-enzymatic method to regenerate nicotinamide adenine dinucleotide at low overpotentials," *Journal of Electroanalytical Chemistry,* **443**(1), 155-161 (1998).

30. S. P. Kumar, R. Manjunatha, C. Nethravathi, G. S. Suresh, M. Rajamathi and T. V. Venkatesha, "Electrocatalytic oxidation of nadh on functionalized graphene modified graphite electrode," *Electroanalysis,* **23**(4), 842-849 (2011).

31. B. L. Hassler, N. Kohli, J. G. Zeikus, I. Lee and R. M. Worden, "Renewable dehydrogenase-based interfaces for bioelectronic applications," *Langmuir,* **23**(13), 7127-7133 (2007).

32. B. L. Hassler and R. M. Worden, "Versatile bioelectronic interfaces based on heterotrifunctional linking molecules," *Biosensors and Bioelectronics,* **21**(11), 2146-2154 (2006).

33. B. L. Hassler, T. J. Amundsen, J. G. Zeikus, I. Lee and R. M. Worden, "Versatile bioelectronic interfaces on flexible non-conductive substrates," *Biosensors and Bioelectronics,* **23**(10), 1481-1487 (2008).

34. M. Zhang, C. Mullens and W. Gorski, "Coimmobilization of dehydrogenases and their cofactors in electrochemical biosensors," *Analytical Chemistry,* **79**(6), 2446-2450 (2007).

35. T. Ikeda and K. Kano, "An electrochemical approach to the studies of biological redox reactions and their applications to biosensors, bioreactors, and biofuel cells," *Journal of Bioscience and Bioengineering,* **92**(1), 9-18 (2001).

36. N. L. Akers, C. M. Moore and S. D. Minteer, "Development of alcohol/o_2 biofuel cells using salt-extracted tetrabutylammonium bromide/nafion membranes to immobilize dehydrogenase enzymes," *Electrochimica Acta,* **50**(12), 2521-2525 (2005).

37. X. Zhao, X. Lu, W. T. Y. Tze and P. Wang, "A single carbon fiber microelectrode with branching carbon nanotubes for bioelectrochemical processes," *Biosensors & Bioelectronics,* **25**(10), 2343-2350 (2010).

38. Y. Tokita, T. Nakagawa, H. Sakai, T. Sugiyama, R. Matsumoto and T. Hatazawa, "Sony's biofuel cell," *ECS Transactions,* **13**(21), 89-97 (2008).

39. R. A. Rincon, *Biofuel cell anode for nad$^+$-dependent enzymes* The University of New Mexico (2010).

40. L. Stoica, N. Dimcheva, Y. Ackermann, K. Karnicka, D. A. Guschin, P. J. Kulesza, J. Rogalski, D. Haltrich, R. Ludwig, L. Gorton and W. Schuhmann, "Membrane-less biofuel cell based on cellobiose dehydrogenase (anode)/laccase (cathode) wired via specific os-redox polymers," *Fuel Cells,* **9**(1), 53-62 (2009).

41. A. Manjon, J. M. Obon, P. Casanova, V. M. Fernandez and J. L. Ilborra, "Increased activity of glucose dehydrogenase co-immobilized with a redox mediator in a bioreactor with electrochemical nad(+) regeneration," *Biotechnology Letters,* **24**(15), 1227-1232 (2002).

42. L. Gorton and P. N. Bartlett, "Nad(p)-based biosensors," in *Bioelectrochemistry,* 157-198 (John Wiley & Sons, Ltd, 2008).

43. H. Zhou, Z. Zhang, P. Yu, L. Su, T. Ohsaka and L. Mao, "Noncovalent attachment of nad$^+$ cofactor onto carbon nanotubes for preparation of integrated dehydrogenase-based electrochemical biosensors," *Langmuir,* **26**(8), 6028-6032 (2010).

44. M. J. Moehlenbrock, M. T. Meredith and S. D. Minteer, "Bioelectrocatalytic oxidation of glucose in cnt impregnated hydrogels: Advantages of synthetic enzymatic metabolon formation," *ACS Catalysis,* **2**(1), 17-25 (2011).

45. A. Eftekhari, "Glycerol biosensor based on glycerol dehydrogenase incorporated into polyaniline modified aluminum electrode using hexacyanoferrate as mediator," *Sensors and Actuators B: Chemical,* **80**(3), 283-289 (2001).

46. Y.-C. Tsai, S.-Y. Chen and H.-W. Liaw, "Immobilization of lactate dehydrogenase within multiwalled carbon nanotube-chitosan nanocomposite for application to lactate biosensors," *Sensors and Actuators B: Chemical,* **125**(2), 474-481 (2007).

47. H. Kinoshita, M. Torimura, K. Yamamoto, K. Kano and T. Ikeda, "Amperometric determination of nad(p)h with peroxidase-based h_2o_2-sensing electrodes and its application to isocitrate dehydrogenase activity assay in serum," *Journal of Electroanalytical Chemistry,* **478**(1–2), 33-39 (1999).

48. K. Guo, K. Qian, S. Zhang, J. L. Kong, C. Z. Yu and B. H. Liu, "Bio-electrocatalysis of nadh and ethanol based on graphene sheets modified electrodes," *Talanta,* **85**(2), 1174-1179 (2011).

49. J. Filip, J. Sefcovicová, P. Tomcík, P. Gemeiner and J. Tkac, "A hyaluronic acid dispersed carbon nanotube electrode used for a mediatorless nadh sensing and biosensing," *Talanta,* **84**(2), 355-361 (2011).

50. A. Salimi, S. Lasghari and A. Noorbakhash, "Carbon nanotubes-ionic liquid and chloropromazine modified electrode for determination of nadh and fabrication of ethanol biosensor," *Electroanalysis,* **22**(15), 1707-1716 (2010).

51. S. Alpat and A. Telefoncu, "Development of an alcohol dehydrogenase biosensor for ethanol determination with toluidine blue o covalently attached to a cellulose acetate modified electrode," *Sensors,* **10**(1), 748-764 (2010).

52. M. Zhou, Y. M. Zhai and S. J. Dong, "Electrochemical sensing and biosensing platform based on chemically reduced graphene oxide," *Analytical Chemistry,* **81**(14), 5603-5613 (2009).

53. D.-W. Yang and H.-H. Liu, "Poly(brilliant cresyl blue)-carbonnanotube modified electrodes for determination of nadh and fabrication of ethanol dehydrogenase-based biosensor," *Biosensors and Bioelectronics,* **25**(4), 733-738 (2009).

54. P. Addo, R. Arechederra and S. Minteer, "Evaluating enzyme cascades for methanol/air biofuel cells based on nad^+-dependent enzymes," *Electroanalysis,* **22**(7-8), 807-812 (2010).

55. D. Sokic-Lazic, R. L. Arechederra, B. L. Treu and S. D. Minteer, "Oxidation of biofuels: Fuel diversity and effectiveness of fuel oxidation through multiple enzyme cascades," *Electroanalysis,* **22**(7-8), 757-764 (2010).

56. S. Seung Hoon, N. Ahluwalia, Y. Leduc, L. T. J. Delbaere and C. Vieille, "Thermotoga maritima tm0298 is a highly thermostable mannitol dehydrogenase," *Applied Microbiology and Biotechnology: 81 (3) 485-495,* **81**(3), 485-495 (2008).

57. S. Song and C. Vieille, "Recent advances in the biological production of mannitol," *Applied Microbiology and Biotechnology,* **84**(1), 55-62 (2009).

58. Y. Zhang, F. Gao, S.-P. Zhang, Z.-G. Su, G.-H. Ma and P. Wang, "Simultaneous production of 1,3-dihydroxyacetone and xylitol from glycerol and xylose using a nanoparticle-supported multi-enzyme system with in situ cofactor regeneration," *Bioresource Technology,* **102**(2), 1837-1843 (2011).

59. P. Wang, "Chapter 12 - nonconventional biocatalysis for production of chemicals and polymers from biomass," in *Bioprocessing for value-added products from renewable resources,* (ed. Shang-Tian, Y.), 325-350 (Elsevier, Amsterdam, 2007).

60. B. El-Zahab, D. Donnelly and P. Wang, "Particle-tethered nadh for production of methanol from co_2 catalyzed by coimmobilized enzymes," *Biotechnology and Bioengineering,* **99**(3), 508-514 (2008).

61. A. A. Karyakin, O. A. Bobrova and E. E. Karyakina, "Electroreduction of nad^+ to enzymatically active nadh at poly(neutral red) modified electrodes," *Journal of Electroanalytical Chemistry,* **399**(1-2), 179-184 (1995).

62. Y. M. Yan, O. Yehezkeli and I. Willner, "Integrated, electrically contacted $nad(p)^+$-dependent enzyme - carbon nanotube electrodes for biosensors and biofuel cell applications," *Chemistry-a European Journal,* **13**(36), 10168-10175 (2007).

63. L. Gorton and E. Dominguez, "Electrocatalytic oxidation of nad(p)h at mediator-modified electrodes," *J Biotechnol,* **82**(4), 371-92 (2002).

64. L. T. F. Allen J. Bard (ed.) *Electrochemical methods: Foundamentals and applications* (2006).

65. Y. Dilgin, L. Gorton and G. Nisli, "Photoelectrocatalytic oxidation of nadh with electropolymerized toluidine blue o," *Electroanalysis,* **19**(2-3), 286-293 (2007).

66. R. Rincón, K. Artyushkova, M. Mojica, M. Germain, S. Minteer and P. Atanassov, "Structure and electrochemical properties of electrocatalysts for nadh oxidation," *Electroanalysis,* **22**(7-8), 799-806 (2010).

67. V. Svoboda, M. Cooney, B. Y. Liaw, S. Minteer, E. Piles, D. Lehnert, S. C. Barton, R. Rincon and P. Atanassov, "Standardized characterization of electrocatalytic electrodes," *Electroanalysis,* **20**(10), 1099-1109 (2008).

68. M. N. Arechederra, P. K. Addo and S. D. Minteer, "Poly(neutral red) as a nad^+ reduction catalyst and a nadh oxidation catalyst: Towards the development of a rechargeable biobattery," *Electrochimica Acta,* **56**(3), 1585-1590 (2011).

69. Y. H. Kim, T. Kim, J. H. Ryu and Y. J. Yoo, "Iron oxide/carbon black (fe_2o_3/cb) composite electrode for the detection of reduced nicotinamide cofactors using an amperometric method under a low overpotential," *Biosensors & Bioelectronics,* **25**(5), 1160-1165 (2010).

70. M. J. Cooney, V. Svoboda, C. Lau, G. Martin and S. D. Minteer, "Enzyme catalysed biofuel cells," *Energy & Environmental Science,* **1**(3), 320-337 (2008).

71. Z. Dong-mei, F. Hui-Qun, C. Hong-yuan, J. Huang-xian and W. Yun, "The electrochemical polymerization of methylene green and its electrocatalysis for the oxidation of nadh," *Analytica Chimica Acta,* **329**(1-2), 41-48 (1996).

72. Z. Wang, M. Etienne, S. Pöller, W. Schuhmann, G.-W. Kohring, V. Mamane and A. Walcarius, "Dehydrogenase-based reagentless biosensors: Electrochemically assisted deposition of sol-gel thin films on functionalized carbon nanotubes," *Electroanalysis,* **24**(2), 376-385 (2012).

73. J. Y. Wang, P. C. Nien, C. H. Chen, L. C. Chen and K. C. Ho, "A glucose bio-battery prototype based on a gdh/(polymethylene blue) bioanode and a graphite cathode with an iodide/tri-iodide redox couple," *Bioresource Technology,* **116**, 502-506 (2012).

74. L. N. Pelster, M. T. Meredith and S. D. Minteer, "Nicotinamide adenine dinucleotide oxidation studies at multiwalled carbon nanotube/polymer composite modified glassy carbon electrodes," *Electroanalysis,* **24**(5), 1011-1018 (2012).

75. M. Wooten and W. Gorski, "Facilitation of nadh electro-oxidation at treated carbon nanotubes," *Analytical Chemistry,* **82**(4), 1299-1304 (2010).

76. C. W. Narváez Villarrubia, R. A. Rincón, V. K. Radhakrishnan, V. Davis and P. Atanassov, "Methylene green electrodeposited on swnts-based “bucky” papers for nadh and l-malate oxidation," *ACS Applied Materials & Interfaces,* **3**(7), 2402-2409 (2011).

77. R. Doaga, T. McCormac and E. Dempsey, "Electrochemical sensing of nadh and glutamate based on meldola blue in 1,2-diaminobenzene and 3,4-ethylenedioxythiophene polymer films," *Electroanalysis,* **21**(19), 2099-2108 (2009).

78. A. E. Blackwell, M. J. Moehlenbrock, J. R. Worsham and S. D. Minteer, "Comparison of electropolymerized thiazine dyes as an electrocatalyst in enzymatic biofuel cells and self powered sensors," in 1714-1721, (Amer Scientific Publishers, 2009).

79. Z. H. Dai, F. X. Liu, G. F. Lu and J. C. Bao, "Electrocatalytic detection of nadh and ethanol at glassy carbon electrode modified with electropolymerized films from methylene green," *Journal of Solid State Electrochemistry,* **12**(2), 175-180 (2008).

80. L. Viry, A. Derre, P. Garrigue, N. Sojic, P. Poulin and A. Kuhn, "Optimized carbon nanotube fiber microelectrodes as potential analytical tools," *Analytical and Bioanalytical Chemistry,* **389**(2), 499-505 (2007).

81. C.-X. Cai and K.-H. Xue, "Electrochemical polymerization of toluidine blue o and its electrocatalytic activity toward nadh oxidation," *Talanta,* **47**(5), 1107-1119 (1998).

82. A. A. Karyakin, E. E. Karyakina and H. L. Schmidt, "Electropolymerized azines: A new group of electroactive polymers," *Electroanalysis,* **11**(3), 149-155 (1999).

83. C.-X. Cai and K.-H. Xue, "The effects of concentration and solution ph on the kinetic parameters for the electrocatalytic oxidation of dihydronicotiamide adenine dinucleotide (nadh) at glassy

carbon electrode modified with electropolymerized film of toluidine blue o," *Microchemical Journal,* **64**(2), 131-139 (2000).

84. K. Vilmos and J. V. B. Gary, "Electropolymerization of methylene blue investigated using on-line electrochemistry/electrospray mass spectrometry," *Electroanalysis,* **13**(17), 1425-1430 (2001).

85. V. Svoboda, M. J. Cooney, C. Rippolz and B. Y. Liaw, "In situ characterization of electrochemical polymerization of methylene green on platinum electrodes," *Journal of the Electrochemical Society,* **154**(3), D113-D116 (2007).

86. M. Musameh, J. Wang, A. Merkoci and Y. Lin, "Low-potential stable nadh detection at carbon-nanotube-modified glassy carbon electrodes," *Electrochemistry Communications,* **4**(10), 743-746 (2002).

87. J. Wang, "Carbon-nanotube based electrochemical biosensors: A review," *Electroanalysis,* **17**(1), 7-14 (2005).

88. G. G. Wildgoose, C. E. Banks, H. C. Leventis and R. G. Compton, "Chemically modified carbon nanotubes for use in electroanalysis," *Microchimica Acta,* **152**(3), 187-214 (2006).

89. Z. Xu, N. Gao and S. J. Dong, "Preparation and layer-by-layer self-assembly of positively charged multiwall carbon nanotubes," *Talanta,* **68**(3), 753-758 (2006).

90. H.-C. Chang, T. Matsue, I. Uchida and T. Osa, "Effect of viologen structure on electroreduction of nad+ catalyzed by diaphorase immobilized on electrodes," *Chemistry Letters,* **18**(7), 1119-1122 (1989).

91. K. Sohyoung, S.-E. Yun and K. Chan, "The formation of a diaphorase enzyme multilayer bound to a self-assembled monolayer for the mediated enzyme-catalyzed reduction of nad+," *Electrochemistry Communications,* **1**(3-4), 151-154 (1999).

92. S. Kim, S. E. Yun and C. Kang, "Electrochemical evaluation of the reaction rate between methyl viologen mediator and diaphorase enzyme for the electrocatalytic reduction of nad(+) and digital simulation for its voltammetric responses," *Journal of Electroanalytical Chemistry,* **465**(2), 153-159 (1999).

93. Y. Ogino, K. Takagi, K. Kano and T. Ikeda, "Reactions between diaphorase and quinone compounds in bioelectrocatalytic redox reactions of nadh and nad(+)," *Journal of Electroanalytical Chemistry,* **396**(1-2), 517-524 (1995).

94. Y.-W. Kang, C. Kang, J.-S. Hong and S.-E. Yun, "Optimization of the mediated electrocatalytic reduction of nad+ by cyclic voltammetry and construction of electrochemically driven enzyme bioreactor," *Biotechnology Letters,* **23**(8), 599-604 (2001).

95. H. Maeda and S. Kajiwara, "Malic acid production by an electrochemical reduction system combined with the use of diaphorase and methylviologen," *Biotechnology and Bioengineering,* **27**(5), 596-602 (1985).

96. A. Salimi, M. Izadi, R. Hallaj, S. Soltanian and H. Hadadzadeh, "Electrocatalytic reduction of nad(+) at glassy carbon electrode modified with single-walled carbon nanotubes and ru(iii) complexes," *Journal of Solid State Electrochemistry,* **13**(3), 485-496 (2009).

97. F. Man and S. Omanovic, "A kinetic study of nad+ reduction on a ruthenium modified glassy carbon electrode," *Journal of Electroanalytical Chemistry,* **568**, 301-313 (2004).

98. A. Azem, F. Man and S. Omanovic, "Direct regeneration of nadh on a ruthenium modified glassy carbon electrode," *Journal of Molecular Catalysis A: Chemical,* **219**(2), 283-299 (2004).

99. T. Tangkuaram, J. Wang, M. C. Rodriguez, R. Laocharoensuk and W. Veerasai, "Highly stable amplified low-potential electrocatalytic detection of nad+ at azure-chitosan modified carbon electrodes," *Sensors and Actuators B: Chemical,* **121**(1), 277-281 (2007).

100. A. A. Karyakin, Y. N. Ivanova and E. E. Karyakina, "Equilibrium (nad+/nadh) potential on poly(neutral red) modified electrode," *Electrochemistry Communications,* **5**(8), 677-680 (2003).

101. D. H. Park and J. G. Zeikus, "Utilization of electrically reduced neutral red by actinobacillus succinogenes: Physiological function of neutral red in membrane-driven fumarate reduction and energy conservation," *Journal of Bacteriology,* **181**(8), 2403-2410 (1999).

102. Damian, A, Maloo, Kh, Omanovic and S, *Direct electrochemical regeneration of nadh on au, cu and pt-au electrodes,* vol. 21 (Croatian Society of Chemical Engineers, Zagreb, CROATIE, 2007).

103. H. Li, H. Wen and S. Calabrese Barton, "Nadh oxidation catalyzed by electropolymerized azines on carbon nanotube modified electrodes," *Electroanalysis,* **24**(2), 398-406 (2012).

104. R. Antiochia and L. Gorton, "Development of a carbon nanotube paste electrode osmium polymer-mediated biosensor for determination of glucose in alcoholic beverages," *Biosensors and Bioelectronics,* **22**(11), 2611-2617 (2007).

105. D. C.-S. Tse and T. Kuwana, "Electrocatalysis of dihydronicotinamide adenosine diphosphate with quinones and modified quinone electrodes," *Analytical Chemistry,* **50**(9), 1315-1318 (1978).

106. J. M. Laval, C. Bourdillon and J. Moiroux, "Enzymic electrocatalysis: Electrochemical regeneration of nad+ with immobilized lactate dehydrogenase modified electrodes," *Journal of the American Chemical Society,* **106**(17), 4701-4706 (1984).

107. J. M. Laval, C. Bourdillon and J. Moiroux, "The electrochemical regeneration of nad+ revisited," *Biotechnology and Bioengineering,* **30**(2), 157-159 (1987).

108. J. Bonnefoy, J. Moiroux, J.-M. Laval and C. Bourdillon, "Electrochemical regeneration of nad+. A new evaluation of its actual yield," *Journal of the Chemical Society, Faraday Transactions 1: Physical Chemistry in Condensed Phases,* **84**(4), 941-950 (1988).

109. A. Fassouane, J. M. Laval, J. Moiroux and C. Bourdillon, "Electrochemical regeneration of nad in a plug-flow reactor," *Biotechnology and Bioengineering,* **35**(9), 935-939 (1990).

110. A. A. Karyakin, "Electropolymerized azines: A new group of electroactive polymers," in *Electropolymerization,* 93-110 (Wiley-VCH Verlag GmbH & Co. KGaA, 2010).

111. R. M. Kelly and D. J. Kirwan, "Electrochemical regeneration of nad+on carbon electrodes," *Biotechnology and Bioengineering,* **19**(8), 1215-1218 (1977).

112. P. J. Elving, C. O. Schmakel, K. S. V. Santhanam and P. Zuman, "Nicotinamide-nad sequence: Redox processes and related behavior: Behavior and properties of intermediate and final products," *C R C Critical Reviews in Analytical Chemistry,* **6**(1), 1-67 (1976).

113. M. A. Jensen and P. J. Elving, "Nicotinamide adenine-dinucleotide (nad+) - formal potential of the nad+ nad. Couple and nad. Dimerization rate," *Biochimica et Biophysica Acta,* **764**(3), 310-315 (1984).

114. D. Gligor, Y. Dilgin, I. C. Popescu and L. Gorton, "Photoelectrocatalytic oxidation of nadh at a graphite electrode modified with a new polymeric phenothiazine," *Electroanalysis,* **21**(3-5), 360-367 (2009).

115. E. J. Eisenberg and K. C. Cundy, "Amperometric high-performance liquid-chromatographic detection of nadh at a base-activated glassy-carbon electrode," *Analytical Chemistry,* **63**(8), 845-847 (1991).

116. X. Q. Liu, B. H. Li and C. Y. Li, "Sensitive determination of dihydronicotinamide adenine dinucleotide and ethanol with a nano-porous carbon electrode," *Journal of the Serbian Chemical Society,* **76**(1), 113-123 (2011).

117. C. Hung Tzang, R. Yuan and M. Yang, "Voltammetric biosensors for the determination of formate and glucose-6-phosphate based on the measurement of dehydrogenase-generated nadh and nadph," *Biosensors and Bioelectronics,* **16**(3), 211-219 (2001).

118. H. R. Zare, R. Samimi and M. Mazloum-Ardakani, "A comparison of the electrochemical behavior of rutin at an inactivated, activated, and multi wall carbon nanotubes modified glassy carbon electrode," *International Journal of Electrochemical Science,* **4**(5), 730-739 (2009).

119. S. M. Golabi and L. Irannejad, "Preparation and electrochemical study of fisetin modified glassy carbon electrode. Application to the determination of nadh and ascorbic acid," *Electroanalysis,* **17**(11), 985-996 (2005).

120. H. R. Zare, M. Eslami and M. Namazian, "Electrochemical behavior of o-chloranil in aqueous solution at an activated glassy carbon electrode," *Electrochimica Acta,* **56**(5), 2160-2164 (2011).

121. A. J. S. Ahammad, S. Sarker, M. A. Rahman and J. J. Lee, "Simultaneous determination of hydroquinone and catechol at an activated glassy carbon electrode," *Electroanalysis,* **22**(6), 694-700 (2010).

122. G. W. Hance and T. Kuwana, "Effect of glassy carbon pretreatment on background double-layer capacitance and adsorption of neutral organic molecules," *Analytical Chemistry,* **59**(1), 131-134 (1987).

123. C. D. Allred and R. L. McCreery, "Adsorption of catechols on fractured glassy carbon electrode surfaces," *Analytical Chemistry,* **64**(4), 444-448 (1992).

124. H. Zhang and L. A. Coury, "Effects of high-intensity ultrasound on glassy carbon electrodes," *Analytical Chemistry,* **65**(11), 1552-1558 (1993).

125. R. J. Rice, N. M. Pontikos and R. L. McCreery, "Quantitative correlations of heterogeneous electron-transfer kinetics with surface properties of glassy carbon electrodes," *Journal of the American Chemical Society,* **112**(12), 4617-4622 (1990).

126. N. Čėnas, J. Rozgaitė, A. Pocius and J. Kulys, "Electrocatalytic oxidation of nadh and ascorbic acid on electrochemically pretreated glassy carbon electrodes," *Journal of Electroanalytical Chemistry and Interfacial Electrochemistry,* **154**(1–2), 121-128 (1983).

127. R. L. McCreery, "Advanced carbon electrode materials for molecular electrochemistry," *Chemical Reviews,* **108**(7), 2646-2687 (2008).

128. N. M. Pontikos and R. L. McCreery, "Microstructural and morphological changes induced in glassy carbon electrodes by laser irradiation," *Journal of Electroanalytical Chemistry,* **324**(1–2), 229-242 (1992).

129. W. E. Van der Linden and J. W. Dieker, "Glassy carbon as electrode material in electroanalytical chemistry," *Analytica Chimica Acta,* **119**(1), 1-24 (1980).

130. S. C. Barton, Y. Sun, B. Chandra, S. White and J. Hone, "Mediated enzyme electrodes with combined micro- and nanoscale supports," *Electrochemical and Solid-State Letters,* **10**(5), B96-B100 (2007).

131. S. Chakraborty and C. R. Raj, "Mediated electrocatalytic oxidation of bioanalytes and biosensing of glutamate using functionalized multiwall carbon nanotubes-biopolymer nanocomposite," *Journal of Electroanalytical Chemistry,* **609**(2), 155-162 (2007).

132. J. Chen, J. Bao, C. Cai and T. Lu, "Electrocatalytic oxidation of nadh at an ordered carbon nanotubes modified glassy carbon electrode," *Analytica Chimica Acta,* **516**(1–2), 29-34 (2004).

133. M. Tominaga, S. Sakamoto and H. Yamaguchi, "Jungle-gym structured films of single-walled carbon nanotubes on a gold surface: Oxidative treatment and electrochemical properties," *The Journal of Physical Chemistry C,* **116**(17), 9498-9506 (2012).

134. A. H. Carl H. Hamann, Wolf Vielstich (ed.) *Electrochemistry* (WILEY-VCH Verlag GmbH & Co. KGaA, Weinheim, 2007).

135. R. W. Murray, J. B. Goodenough and W. J. Albery, "Modified electrodes: Chemically modified electrodes for electrocatalysis [and discussion]," *Philosophical Transactions of the Royal Society of London. Series A, Mathematical and Physical Sciences,* **302**(1468), 253-265 (1981).

136. S. Treimer, A. Tang and D. C. Johnson, "A consideration of the application of koutecký-levich plots in the diagnoses of charge-transfer mechanisms at rotated disk electrodes," *Electroanalysis,* **14**(3), 165-171 (2002).

137. P. Kar, H. Wen, H. Li, S. D. Minteer and S. C. Barton, "Simulation of multistep enzyme-catalyzed methanol oxidation in biofuel cells," *Journal of the Electrochemical Society,* **158**(5), B580-B586 (2011).

138. G. Rahamathunissa and L. Rajendran, "Application of he's variational iteration method in nonlinear boundary value problems in enzyme– substrate reaction diffusion processes: Part 1. The steady-state amperometric response," *Journal of Mathematical Chemistry,* **44**(3), 849-861 (2008).

139. P. N. Bartlett, C. S. Toh, E. J. Calvo and V. Flexer, "Modelling biosensor responses," in *Bioelectrochemistry,* 267-325 (John Wiley & Sons, Ltd, 2008).

140. P. N. Bartlett and K. F. E. Pratt, "Theoretical treatment of diffusion and kinetics in amperometric immobilized enzyme electrodes .1. Redox mediator entrapped within the film," *Journal of Electroanalytical Chemistry,* **397**(1-2), 61-78 (1995).

141. P. Manimozhi, A. Subbiah and L. Rajendran, "Solution of steady-state substrate concentration in the action of biosensor response at mixed enzyme kinetics," *Sensors and Actuators B-Chemical,* **147**(1), 290-297 (2010).

142. A. Meena and L. Rajendran, "Analytical solution of system of coupled non-linear reaction diffusion equations part ii direct reaction of substrate at underlying microdisc surface," *Journal of Electroanalytical Chemistry,* **650**(1), 143-151 (2010).

143. S. Calabrese Barton, "Oxygen transport in composite mediated biocathodes," *Electrochimica Acta,* **50**(10), 2145-2153 (2005).

144. R. A. Holt and S. R. Rigby, "Process for microbial reduction producing 4(s)-hydroxy-6(s)methyl-thienopyran derivatives " U.S. Pat. Appl. No. 5580764, (1996).

145. J. C. Moore, D. J. Pollard, B. Kosjek and P. N. Devine, "Advances in the enzymatic reduction of ketones," *Accounts of Chemical Research,* **40**(12), 1412-1419 (2007).

146. K. Götz, L. Hilterhaus and A. Liese, "Industrial application of oxidoreductase catalyzed reduction of ketones and aldehydes," in *Enzyme catalysis in organic synthesis,* 1205-1223 (Wiley-VCH Verlag GmbH & Co. KGaA, 2012).

147. F. Tasca, L. Gorton, J. B. Wagner and G. Noll, "Increasing amperometric biosensor sensitivity by length fractionated single-walled carbon nanotubes," *Biosensors & Bioelectronics,* **24**(2), 272-278 (2008).

148. M. Sosna, A. Bonamore, L. Gorton, A. Boffi and E. E. Ferapontova, "Direct electrochemistry and os-polymer-mediated bioelectrocatalysis of nadh oxidation by escherichia coli flavohemoglobin at graphite electrodes," *Biosensors & bioelectronics,* **42** (2013).

149. L. Zhang, Y. Li, D. W. Li, D. Karpuzov and Y. T. Long, "Electrocatalytic oxidation of nadh on graphene oxide and reduced graphene oxide modified screen-printed electrode," *International Journal of Electrochemical Science,* **6**(3), 819-829 (2011).

150. M. Masuda, Y. Motoyama, K. Murata, N. Nakamura and H. Ohno, "Preparation of an electrode modified with an electropolymerized film as a mediator of nadh oxidation and its application in an ethanol/o-2 biofuel cell," *Electroanalysis,* **23**(10), 2297-2301 (2011).

151. Y. Dilgin, B. Ertek, B. Kizilkaya, D. G. Dilgin and H. I. Gokcel, "Electrocatalytic oxidation of nadh using a pencil graphite electrode modified with hematoxylin," *Science of Advanced Materials,* **4**(9), 920-927 (2012).

152. F. S. Saleh, M. R. Rahman, T. Okajima, L. Mao and T. Ohsaka, "Determination of formal potential of nadh/nad+ redox couple and catalytic oxidation of nadh using poly(phenosafranin)-modified carbon electrodes," *Bioelectrochemistry,* **80**(2), 121-127 (2011).

153. F. S. Saleh, T. Okajima, F. Kitamura, L. Q. Mao and T. Ohsaka, "Poly(phenosafranin)-functionalized single-walled carbon nanotube as nanocomposite electrocatalysts: Fabrication and electrocatalysis for nadh oxidation," *Electrochimica Acta,* **56**(13), 4916-4923 (2011).

154. L. Zhu, J. Zhai, R. Yang, C. Tian and L. Guo, "Electrocatalytic oxidation of nadh with meldola's blue functionalized carbon nanotubes electrodes," *Biosensors and Bioelectronics,* **22**(11), 2768-2773 (2007).

155. M. Huang, H. Jiang, J. Zhai, B. Liu and S. Dong, "A simple route to incorporate redox mediator into carbon nanotubes/nafion composite film and its application to determine nadh at low potential," *Talanta,* **74**(1), 132-139 (2007).

156. J. Zeng, W. Wei, L. Wu, X. Liu, K. Liu and Y. Li, "Fabrication of poly(toluidine blue o)/carbon nanotube composite nanowires and its stable low-potential detection of nadh," *Journal of Electroanalytical Chemistry,* **595**(2), 152-160 (2006).

157. H. Wen, V. Nallathambi, D. Chakraborty and S. C. Barton, "Carbon fiber microelectrodes modified with carbon nanotubes as a new support for immobilization of glucose oxidase," *Microchimica Acta,* **175**(3-4), 283-289 (2011).

158. S. L. Flegler, J. W. Heckman and K. L. Klomparens, *Scanning and transmission electron microscopy: An introduction,* vol. (Oxford University Press, 1993).

159. K. Kinoshita (ed.) *Carbon: Electrochemical and physicochemical properties* (Wiley-Interscience, 1988).

160. J. Moiroux and P. J. Elving, "Mechanistic aspects of the electrochemical oxidation of dihydronicotinamide adenine dinucleotide (nadh)," *Journal of the American Chemical Society,* **102**(21), 6533-6538 (1980).

161. A. A. Karyakin, Y. N. Ivanova, K. V. Revunova and E. E. Karyakina, "Electropolymerized flavin adenine dinucleotide as an advanced nadh transducer," *Analytical Chemistry,* **76**(7), 2004-2009 (2004).

162. V. Svoboda and B. Y. Liaw, "In situ transient study of polymer film growth via simultaneous correlation of charge, mass, and ellipsometric measurements," in 2439-2449, (Int Union Pure Applied Chemistry, 2008).

163. R. P. Akkermans, S. L. Roberts, F. Marken, B. A. Coles, S. J. Wilkins, J. A. Cooper, K. E. Woodhouse and R. G. Compton, "Methylene green voltammetry in aqueous solution: Studies using thermal, microwave, laser, or ultrasonic activation at platinum electrodes," *Journal of Physical Chemistry B,* **103**(45), 9987-9995 (1999).

164. M. Zhang, A. Smith and W. Gorski, "Carbon nanotube−chitosan system for electrochemical sensing based on dehydrogenase enzymes," *Analytical Chemistry,* **76**(17), 5045-5050 (2004).

165. Y. Gibon and F. Larher, "Cycling assay for nicotinamide adenine dinucleotides: Nacl precipitation and ethanol solubilization of the reduced tetrazolium," *Analytical Biochemistry,* **251**(2), 153-157 (1997).

166. H. Matsumura and S. Miyachi, "[43] cycling assay for nicotinamide adenine dinucleotides," in *Methods in enzymology,* vol. Volume 69 (ed. Anthony San, P.), 465-470 (Academic Press, 1980).

167. C. Vilcheze, T. R. Weisbrod, B. Chen, L. Kremer, M. H. Hazbon, F. Wang, D. Alland, J. C. Sacchettini and W. R. Jacobs, "Altered nadh/nad(+) ratio mediates coresistance to isoniazid and ethionamide in mycobacteria," *Antimicrobial Agents and Chemotherapy,* **49**(2), 708-720 (2005).

168. Greenbau.Al, J. B. Clark and P. Cmlean, "Estimation of oxidized and reduced forms of nicotinamide nucleotides," *Biochemical Journal,* **95**(1), 161-166 (1965).

169. O. H. Lowry, M. K. Rock, D. W. Schulz and J. V. Passonneau, "Measurement of pyridine nucleotides by enzymatic cycling," *Journal of Biological Chemistry,* **236**(10), 2746-& (1961).

170. J. F. Biellmann, C. Lapinte, E. Haid and G. Weimann, "Structure of lactate dehydrogenase inhibitor generated from coenzyme," *Biochemistry,* **18**(7), 1212-1217 (1979).

171. O. H. Lowry, M. K. Rock and J. V. Passonneau, "Stability of pyridine nucleotides," *Journal of Biological Chemistry,* **236**(10), 2756-& (1961).

172. D. Hofmann, A. Wirtz, B. Santiago-Schubel, U. Disko and M. Pohl, "Structure elucidation of the thermal degradation products of the nucleotide cofactors nadh and nadph by nano-esi-fticr-ms and hplc-ms," *Analytical and Bioanalytical Chemistry,* **398**(7-8), 2803-2811 (2010).

173. O. H. Lowry, J. V. Passonneau, D. W. Schulz and M. K. Rock, "The measurement of pyridine nucleotides by enzymatic cycling," *Journal of Biological Chemistry,* **236**(10), 2746-2755 (1961).

174. B. D. Epstein, Dallemol.E and J. S. Mattson, "Electrochemical investigations of surface functional groups on isotropic pyrolytic carbon," *Carbon,* **9**(5), 609-& (1971).

175. D. Laser and M. Ariel, "The anodic behavior of glassy carbon in acid solution: A spectroelectrochemical study," *Journal of Electroanalytical Chemistry and Interfacial Electrochemistry,* **52**(2), 291-303 (1974).

176. K. Gong, S. Chakrabarti and L. Dai, "Electrochemistry at carbon nanotube electrodes: Is the nanotube tip more active than the sidewall?," *Angewandte Chemie International Edition,* **47**(29), 5446-5450 (2008).

177. M. Musameh, N. S. Lawrence and J. Wang, "Electrochemical activation of carbon nanotubes," *Electrochemistry Communications,* **7**(1), 14-18 (2005).

178. H. Wen, V. Nallathambi, D. Chakraborty and S. Calabrese Barton, "Carbon fiber microelectrodes modified with carbon nanotubes as a new support for immobilization of glucose oxidase," *Microchimica Acta,* **175**(3-4), 283-289 (2012).

179. G. M. Jenkins and K. Kawamura, "Structure of glassy carbon," *Nature,* **231**(5299), 175-& (1971).

180. A. Dekanski, J. Stevanović, R. Stevanović, B. Ž. Nikolić and V. M. Jovanović, "Glassy carbon electrodes: I. Characterization and electrochemical activation," *Carbon,* **39**(8), 1195-1205 (2001).

181. J. L. Figueiredo, M. F. R. Pereira, M. M. A. Freitas and J. J. M. Órfão, "Modification of the surface chemistry of activated carbons," *Carbon,* **37**(9), 1379-1389 (1999).

182. L. J. Kepley and A. J. Bard, "Ellipsometric, electrochemical, and elemental characterization of the surface phase produced on glassy-carbon electrodes by electrochemical activation," *Analytical Chemistry,* **60**(14), 1459-1467 (1988).

183. M. J. S. Dewar and N. Trinajstic, "Ground states of conjugated molecules - xiv: Redox potentials of quinones," *Tetrahedron,* **25**(18), 4529-4534 (1969).

184. K. S. Prasad, J. C. Chen, C. Ay and J. M. Zen, "Mediatorless catalytic oxidation of nadh at a disposable electrochemical sensor," *Sensors and Actuators B: Chemical,* **123**(2), 715-719 (2007).

185. J. Wang and T. Peng, "Enhanced stability of glassy carbon detectors following a simple electrochemical pretreatment," *Analytical Chemistry,* **58**(8), 1787-1790 (1986).

186. D. Dicu, F. D. Munteanu, I. C. Popeseu and L. Gorton, "Indophenol and o-quinone derivatives immobilized on zirconium phosphate for nadh electro-oxidation," *Analytical Letters,* **36**(9), 1755-1779 (2003).

187. S. Woislawski, "The spectrophotometric determination of ionization constants of basic dyes1," *Journal of the American Chemical Society,* **75**(21), 5201-5203 (1953).

188. P. J. F. Harris, "Fullerene-related structure of commercial glassy carbons," *Philosophical Magazine,* **84**(29), 3159-3167 (2004).

189. M. F. R. Pereira, S. F. Soares, J. J. M. Órfão and J. L. Figueiredo, "Adsorption of dyes on activated carbons: Influence of surface chemical groups," *Carbon,* **41**(4), 811-821 (2003).

190. P. C. C. Faria, J. J. M. Órfão and M. F. R. Pereira, "Adsorption of anionic and cationic dyes on activated carbons with different surface chemistries," *Water Research,* **38**(8), 2043-2052 (2004).

191. M. Arechederra, C. Jenkins, R. A. Rincon, K. Artyushkova, P. Atanassov and S. Minteer, "Poly(methylene blue) and poly(methylene green): Comparison between the electrochemical and chemical syntheses, chemical properties and application as an nadh electrocatalyst," *ECS Meeting Abstracts,* **1001**(6), 446-446 (2010).

192. A. A. Karyakin, A. K. Strakhova, E. E. Karyakina, S. D. Varfolomeyev and A. K. Yatsimirsky, "The electrochemical polymerization of methylene blue and bioelectrochemical activity of the resulting film," *Bioelectrochemistry and Bioenergetics,* **32**(1), 35-43 (1993).

193. S. S. Yazdani and R. Gonzalez, "Anaerobic fermentation of glycerol: A path to economic viability for the biofuels industry," *Current Opinion in Biotechnology,* **18**(3), 213-219 (2007).

194. W. Hu, D. Knight, B. Lowry and A. Varma, "Selective oxidation of glycerol to dihydroxyacetone over pt−bi/c catalyst: Optimization of catalyst and reaction conditions," *Industrial & Engineering Chemistry Research,* **49**(21), 10876-10882 (2010).

195. Z.-C. Hu, Y.-G. Zheng and Y.-C. Shen, "Dissolved-oxygen-stat fed-batch fermentation of 1,3-dihydroxyacetone from glycerol by gluconobacter oxydans zjb09112," *Biotechnology and Bioprocess Engineering,* **15**(4), 651-656 (2010).

196. F.-G. Bănică, "Mathematical modeling of mediated amperometric enzyme sensors," in *Chemical sensors and biosensors,* 332-346 (John Wiley & Sons, Ltd, 2012).

197. S. Loghambal and L. Rajendran, "Mathematical modeling of diffusion and kinetics in amperometric immobilized enzyme electrodes," *Electrochimica Acta,* **55**(18), 5230-5238 (2010).

198. K. M. Ivanetich, R. D. Goold and C. N. T. Sikakana, "Explanation of the nonhyperbolic kinetics of the glutathione s-transferases by the simplest steady-state random sequential bi bi mechanism," *Biochemical Pharmacology,* **39**(12), 1999-2004 (1990).

199. I. H. Segel (ed.) *Enzyme kinetics: Behavior and analysis of rapid equilibrium and steady-state enzyme systems* (Wiley-Interscience, New York, 1993).

200. H. N. Choi, J. Y. Lee, Y. K. Lyu and W. Y. Lee, "Tris(2,2 '-bipyridyl)ruthenium(ii) electrogenerated chemiluminescence sensor based on carbon nantube dispersed in sol-gel-derived titania-nafion composite films," *Analytica Chimica Acta,* **565**(1), 48-55 (2006).

201. H. N. Choi, S. H. Yoon, Y. K. Lyu and W. Y. Lee, "Electrogenerated chemiluminese ethanol biosensor based on carbon nanotube-titania-nafion composite film," *Electroanalysis,* **19**(4), 459-465 (2007).

202. T. J. Thomas, K. E. Ponnusamy, N. M. Chang, K. Galmore and S. D. Minteer, "Effects of annealing on mixture-cast membranes of nafion® and quaternary ammonium bromide salts," *Journal of Membrane Science,* **213**(1–2), 55-66 (2003).

203. R. L. Arechederra and S. D. Minteer, "Kinetic and transport analysis of immobilized oxidoreductases that oxidize glycerol and its oxidation products," *Electrochimica Acta,* **55**(26), 7679-7682 (2010).

204. D. Chakraborty and S. C. Barton, "Influence of mediator redox potential on fuel sensitivity of mediated laccase oxygen reduction electrodes," *Journal of the Electrochemical Society,* **158**(4), B440-B447 (2011).

205. H. Nishise, A. Nagao, Y. Tani and H. Yamada, "Studies on microbial glycerol dehydrogenase. 3. Further characterization of glycerol dehydrogenase from cellulomonas sp nt3060," *Agricultural and Biological Chemistry,* **48**(6), 1603-1609 (1984).

206. G. Gartner and G. Kopperschlager, "Purification and properties of glycerol dehydrogenase from cadida-valida," *Journal of General Microbiology,* **130**(DEC), 3225-3233 (1984).